THE HONG KONG
POLYTECHNIC UNIVERSITY
香港理工大學
Pao Yue-kong Library
包玉剛圖書館

Copyright Undertaking

This thesis is protected by copyright, with all rights reserved.

By reading and using the thesis, the reader understands and agrees to the following terms:

1. The reader will abide by the rules and legal ordinances governing copyright regarding the use of the thesis.
2. The reader will use the thesis for the purpose of research or private study only and not for distribution or further reproduction or any other purpose.
3. The reader agrees to indemnify and hold the University harmless from and against any loss, damage, cost, liability or expenses arising from copyright infringement or unauthorized usage.

IMPORTANT

If you have reasons to believe that any materials in this thesis are deemed not suitable to be distributed in this form, or a copyright owner having difficulty with the material being included in our database, please contact lbsys@polyu.edu.hk providing details. The Library will look into your claim and consider taking remedial action upon receipt of the written requests.

Pao Yue-kong Library, The Hong Kong Polytechnic University, Hung Hom, Kowloon, Hong Kong

http://www.lib.polyu.edu.hk

APPLICATION OF NEURAL NETWORKS AND IMAGE PROCESSING TECHNIQUES IN DISTRIBUTED OPTICAL FIBER SENSOR SYSTEMS

WANG BIWEI

PhD

The Hong Kong Polytechnic University

2023

The Hong Kong Polytechnic University
Department of Electronic and Information Engineering

Application of Neural Networks and Image Processing Techniques in Distributed Optical Fiber Sensor Systems

Wang Biwei

A thesis submitted in partial fulfillment of the requirements for
the degree of Doctor of Philosophy
August 2022

CERTIFICATE OF ORIGINALITY

I hereby declare that this thesis is my own work and that, to the best of my knowledge and belief, it reproduces no material previously published or written, nor material that has been accepted for the award of any other degree or diploma, except where due acknowledgment has been made in the text.

Signature: ____________________

Name of Student: Wang Biwei

Abstract

Distributed optical fiber sensor (DOFS) techniques have attracted a lot of interest in both research and application areas due to their capabilities of measuring temperature, strain, and vibration at consecutive points over a very long distance. Among all DOFS techniques, Brillouin optical time domain analyzer (BOTDA) and phase-sensitive optical time-domain reflectometry (Φ-OTDR) are two of the most popular directions in recent years. Inspired by the successful application of advanced machine learning and image processing techniques in the field of optical fiber communication, while the DOFS systems are very similar to optical fiber communication systems in fact, this thesis focuses on the application of some neural network (NN) techniques, including artificial neural network (ANN), convolutional neural network (CNN), and deep neural networks (DNN), and also an image processing method, the video block-matching and 3D filtering (VBM3D) in BOTDA and Φ-OTDR to improve the system performance and solve existing problems.

First, the DNN-based temperature distribution extraction method for using the BOTDA system is demonstrated experimentally. After appropriate training of DNN model, temperature distribution information along the fiber under test (FUT) could be directly extracted from the experimentally obtained local Brillouin gain spectrums (BGS) using DNN without the need of calculating Brillouin frequency shift (BFS) and transforming it to temperature as the conventional Lorentz curve fitting (LCF) method

does. The results of temperature extraction using DNN show a comparable accuracy to that of using conventional LCF method, which proves that DNN can be used in BOTDA for temperature extraction.

Second, simultaneous temperature and strain measurement by using DNN for BOTDA has been demonstrated with enhanced accuracy. After trained by using combined ideal clean and noisy BGSs, the DNN is applied to extract both the temperature and strain directly from the measured double-peak BGS in large-effective-area fiber (LEAF). Both simulated and experimental data under different temperature and strain conditions have been used to verify the reliability of DNN based simultaneous temperature and strain measurement, and to demonstrate its advantages over BOTDA with the conventional equation-solving method. Avoiding the small matrix determinant induced large error, the DNN approach significantly improves the measurement accuracy. The enhanced accuracy and fast processing speed make the DNN approach a practical way of achieving simultaneous temperature and strain measurement by the conventional BOTDA system without adding extra system complexity.

In addition, a method of robust and fast temperature extraction for BOTDA using the denoising autoencoder (DAE) based DNN is demonstrated. After appropriate training, the DAE suppresses the noise on the measured BGS, and improves the signal-to-noise ratio (SNR) by 9.96dB in the experiment. To extract temperature, the DAE as a basic block is stacked to form the DNN model. Since the DNN model is based on DAE, both denoising and fast temperature extraction can be simultaneously finished using only one DNN model. Moreover, since the temperature information can be extracted directly from the experimental BGS data, the speed of temperature extraction using the DAE based DNN is faster by 500 times than that using LCF. Combining the advantages of both denoising and fast processing speed, the DAE based DNN would be a practical way of temperature extraction for the BOTDA systems.

Besides, the video-BM3D denoising method is proposed and experimentally demonstrated for the first time in a 100.8km long-distance BOTDA sensing system with 2m spatial resolution. Both experiments under static and slowly varying temperature environment are carried out. A temperature uncertainty of 0.43°C has been achieved with denoising by VBM3D in static temperature measurement. The slowly varying temperature at the end of 100.8km fiber has also been accurately measured. VBM3D exploits both the spatial and temporal correlations of the data for denoising, thus it can significantly reduce the temperature fluctuations and keep the measured values close to the real temperature even if the temperature is temporally changing. Thus, it would be useful for the long-distance sensing where the measurand may have temporal evolution in the slowly varying environment.

Finally, the ANN and CNN are applied in the Φ-OTDR, which is an optic fiber distributed acoustic sensing (DAS) system, to detect the sound and to predict the existence of red palm weevil (RPW). RPW is a detrimental pest, which has wiped out many palm tree farms worldwide. However, early detection of RPW is challenging, especially in large-scale farms. Here, machine learning techniques including the ANN and CNN are combined with the DAS as a solution for the early detection of RPW.

Within the laboratory environment, we reconstructed the conditions of a farm that includes an infested tree with ~12 day old weevil larvae and another healthy tree. Meanwhile, some noise sources are introduced, including wind and bird sounds around the trees. After training with the experimental time- and frequency-domain data provided by the DAS system, a fully-connected ANN and a CNN can efficiently recognize the healthy and infested trees with high classification accuracy values (99.9% by ANN with temporal data and 99.7% by CNN with spectral data, in reasonable noise conditions). This work paves the way for deploying the high efficiency and cost-effective fiber optic DAS to monitor RPW in open-air and large-scale farms containing thousands of trees.

Declaration

I hereby declare that this thesis is composed by myself and all the contents have not been submitted to any other universities for a degree. The materials of some chapters have been published in the following conferences or journals:

Chapter 3

- **B. Wang**, L. Wang, N. Guo, F. N. Khan, A. K. Azad, C. Yu, and C. Lu, “Extraction of temperature distribution using deep neural networks for BOTDA sensing system,” in Conference on Lasers and Electro-Optics/Pacific Rim 2017 (CLEO-PR), Paper s2027, pp. 1-4, Singapore, 31 July-4 August, 2017.

Chapter 4

- **B. Wang**, L. Wang, N. Guo, Z. Zhao, C. Yu, and C. Lu, "Deep neural networks assisted BOTDA for simultaneous temperature and strain measurement with enhanced accuracy," Optics Express, vol. 27, no. 3, pp. 2530-2543, 2019.

Chapter 5

- **B. Wang**, N. Guo, L. Wang, C. Yu, and C. Lu, "Robust and fast temperature extraction for Brillouin optical time-domain analyzer by using denoising autoencoder based deep neural networks," *IEEE Sensors Journal*, vol. 20, no. 7, pp. 3614-3620, 2020.

Chapter 6

- **B. Wang**, L. Wang, C. Yu, and C. Lu, "Long-distance BOTDA sensing systems using video-BM3D denoising for both static and slowly varying environment," *Optics Express*, vol. 27, no. 25, pp. 36100-36113, 2019.

Chapter 7

- **B. Wang**, Y. Mao*, I. Ashry*, Y. Al-Fehaid, A. Al-Shawaf, T. K. Ng, C. Yu, and B. S. Ooi, "Towards detecting red palm weevil using machine learning and fiber optic distributed acoustic sensing," *Sensors*, vol. 21, no. 5, 1592, 2021.

Publications

Journal paper:

1. **B. Wang**, L. Wang, N. Guo, Z. Zhao, C. Yu, and C. Lu, "Deep neural networks assisted BOTDA for simultaneous temperature and strain measurement with enhanced accuracy," *Optics Express*, vol. 27, no. 3, pp. 2530-2543, 2019.
2. **B. Wang**, L. Wang, C. Yu, and C. Lu, "Long-distance BOTDA sensing systems using video-BM3D denoising for both static and slowly varying environment," *Optics Express*, vol. 27, no. 25, pp. 36100-36113, 2019.
3. **B. Wang**, N. Guo, L. Wang, C. Yu, and C. Lu, "Robust and fast temperature extraction for Brillouin optical time-domain analyzer by using denoising autoencoder based deep neural networks," *IEEE Sensors Journal*, vol. 20, no. 7, pp. 3614-3620, 2020.
4. K. Luo, **B. Wang***, N. Guo, K. Yu, C. Yu, and C. Lu, "Enhancing SNR by anisotropic diffusion for Brillouin distributed optical fiber sensors," *Journal of Lightwave Technology*, vol. 38, no. 20, pp. 5844-5852, 2020.
5. Y. Mao, I. Ashry*, **B. Wang**, F. Hveding, A. Y. Bukhamseen, K. T. Ng, and B. S. Ooi, "Sensing within the OTDR dead-zone using a two-mode fiber," Optics. Letters, vol. 45, no. 11, pp. 2969-2972, 2020.
6. I. Ashry, Y. Mao*, A. Trichili*, **B. Wang***, T. K. Ng, M. Alouini, and B. S. Ooi, "A review of using few-mode fibers for optical sensing," in *IEEE Access*, vol. 8, pp. 179592-179605, 2020.

7. **B. Wang**, Y. Mao*, I. Ashry*, Y. Al-Fehaid, A. Al-Shawaf, T. K. Ng, C. Yu, and B. S. Ooi, "Towards detecting red palm weevil using machine learning and fiber optic distributed acoustic sensing," *Sensors*, vol. 21, no. 5, 1592, 2021.
8. I. Ashry*, Yuan Mao*, **B. Wang***, F. Hveding, A. Y. Bukhamsin, T. K. Ng, and B. S. Ooi, "A Review of Distributed Fiber--optic Sensing in the Oil and Gas Industry," *Journal of Lightwave Technology*, vol. 40, no. 5, pp. 1407-1431, 2022.

Conference paper:

1. **B. Wang**, L. Wang, N. Guo, F. N. Khan, A. K. Azad, C. Yu, and C. Lu, “Extraction of temperature distribution using deep neural networks for BOTDA sensing system,” in *Conference on Lasers and Electro-Optics/Pacific Rim 2017 (CLEO-PR)*, Paper s2027, pp. 1-4, Singapore, 31 July-4 August, 2017.
2. L. Wang, **B. Wang**, C. Jin, N. Guo, C. Yu, and C. Lu, "Brillouin optical time domain analyzer enhanced by artificial/deep neural networks," in *2017 16th International Conference on Optical Communications and Networks (ICOCN)*, pp. 1-3, Wuzhen, China, 7-10, August, 2017.
3. **B. Wang**, L. Wang, C. Yu, and C. Lu, "Simultaneous temperature and strain measurement using deep neural networks for BOTDA sensing system," in *Optical Fiber Communication Conference 2018 (OFC)*, Paper Th2A.66, pp. 1-3, San Diego, USA, 11-15 March, 2018.
4. **B. Wang**, N. Guo, L. Wang, C. Yu, and C. Lu, "Denoising and robust temperature extraction for BOTDA systems based on denoising autoencoder and DNN," in *26th*

International Conference on Optical Fiber Sensors (OFS), Paper WF29, pp. 1-4, Lausanne, Switzerland, 24-28 September, 2018.

5. **B. Wang**, L. Wang, C. Yu, and C. Lu, “Video-BM3D denoising for BOTDA sensing systems,” in *2019 Asia Communications and Photonics Conference (ACP)*, Paper M3A.2, pp. 1-3, Chengdu, China, 2-5 November, 2019.
6. L. Wang, **B. Wang**, and C. Yu, "Advanced image and video denoising techniques for BOTDA system under both static and slowly varying environment," in *Proc. SPIE, vol. 11547 Optoelectronic Devices and Integration IX*, 1154704, online, 11-16 October, 2020.
7. G. Yang, **B. Wang**, L. Wang, Z. Cheng, C. Yu, C. C. Chan, L. Li, M. Tang, and D. Liu, "Optimization of 2D-BM3D denoising for long-range Brillouin optical time domain analysis," in *Asia Communications and Photonics Conference 2020 (ACP)*, Paper M4A.125, pp. 1-3, Beijing, China, 24-27 October, 2020.

Acknowledgements

It is only at this point that I realize the long journey of my PhD study is coming to an end. I would like to thank many people for their help and support during my PhD study. First, I would like to express my deepest gratitude to my supervisor, Prof. YU Changyuan. He not only provided me with the valuable opportunity to start my PhD study at the Hong Kong Polytechnic University, but also gave me a lot of patience and support in my study and research work. Moreover, his superb academic level and noble personality profoundly influenced me. I am incredibly grateful to have spent this precious and unforgettable period of PhD study under his guidance.

I also need to thank Prof. LU Chao for offering me a position of research assistant before my PhD study, which helped me get started and get familiar with the research work and direction. And then, I want to thank Prof. WANG Liang for his specific guidance and lots of advice during my PhD study.

I have also received much guidance and support from Prof. Alex WAI, Prof. TAM Hwa-Yaw, and their research group members, including Dr. LI Feng, Dr. KANG Zhe, Dr. SHANG Chao, Dr. HUANG Dongmei, Dr. ZHANG Xianting, Dr. LIU Zhenyong, Dr. CHENG Xin, Dr. HE Jijun, Dr. Dinusha GUNAWARDENA, Dr. CUI Jingxian, Dr. MEI Chao, and Mr. CHENG Zihao.

Especially, I want to thank Dr. GUO Nan, Dr. MAO Yuan, Dr. YU Kuanglu, Dr. Faisal Nadeem KHAN, Dr. Abul Kalam AZAD, Dr. DONG Zhenhua, Dr. JIN Chao, Dr.

GUI Tao, Dr. WU Huan, Dr. ZHU Kun, Dr. ZHAO Zhiyong, Dr. ZHOU Hailong, Dr. ZHOU Xian, Dr. YUAN Jinhui, Dr. GUO Changjian, Dr. HUO Jiahao, Dr. LU Xingyu, Dr. LU Jianing, Dr. YAN Yaxi, Dr. DONG Zheng, Dr. ZHAO Yan, Mr. FAN Qirui, and Mr. WU Xiong for their help in daily life and study. And also, I would like to express my thanks to Dr. LIU Yi, Dr. TU Jiajing, Dr. YOU Xiaodi, Dr. XUE Min, Dr. DONG Bo, Dr. LI Yan, Dr. DU Xinwei, Dr. DONG Shandong, Dr. WANG Wenxuan, Dr. HUANG Zhuili, Dr. TAN Fengze, Dr. WANG Zhuo, Dr. YUAN Weihao, Dr. LUO Huaijian, Dr. CHEN Shuyang, Mr. YANG Zongru, and all other members of our research group. I have learned a lot from the work and discussion with them, which offered me plenty of constructive suggestions and ideas, and contributed much to my research work.

My thanks are also extended to other colleagues and staffs in our Photonics Research Institute (PRI), Department of Electronic and Information Engineering (EIE), and the Research Office I worked with during my PhD study. I am very grateful for their kind help, valuable advice, and patiently support, without which I could not complete the work in this thesis.

Finally, I would like to express my great gratitude to my family and my girlfriend for their unconditional love, best wishes, and unwavering support. Thanks for always being there for me, whenever and wherever.

August 2022

Contents

List of abbreviations

A

ADC	Analog-to-digital converter
AI	Artificial intelligence
ANN	Artificial neural network
AOM	Acousto-optic modulator
APD	Avalanche photodiodes
ASE	Amplified spontaneous emission

B

BFS	Brillouin frequency shift
BGS	Brillouin gain spectrum
BPF	Band pass filter
BPS	Brillouin phase-shift spectrum
BOCDA	Brillouin optical correlation domain analyzer
BOCDR	Brillouin optical correlation domain reflectometry
BOFDA	Brillouin optical frequency domain analyzer
BOFDR	Brillouin optical frequency domain reflectometry
BOTDA	Brillouin optical time domain analysis
BOTDR	Brillouin optical time domain reflectometry
BP	Back-propagation

C

CD	Chromatic dispersion
CNN	Convolutional neural network
CW	Continuous wave

D

DAE	Denoising autoencoder
DAQ	Data acquisition device
DAS	Distributed acoustic sensing
DC	Direct current
DCF	Dispersion compensating fiber
DEMUX	Demultiplexer
DnCNN	Denoising convolutional neural networks
DNN	Deep neural networks

DFB	Distributed feedback
DXS	Distributed multiplexed sensing
DOFS	Distributed optical fiber sensing
DPP	Differential pulse-pair
DRA	Distributed Raman amplification
DSB	Dual sideband
DSF	Dispersion shift fiber
DSP	Digital signal processing
DSS	Distributed strain sensing
DTS	Distributed temperature sensing
DTSS	Distributed temperature and strain sensing
DVS	Distributed vibration sensors
E	
EDFA	Erbium-doped fiber amplifier
EMI	Electromagnetic interference
EOM	Electro-optic modulator
F	
FBG	Fiber Bragg grating
FBS	Forward Brillouin scattering
FDM	Frequency-division multiplexing
FFT	Fast Fourier transform
FMF	Few-mode fiber
FUT	Fiber under test
FWM	Four-wave mixing
FWHM	Full-width at half-maximum
G	
GAWBS	Guided acoustic–wave Brillouin scattering
GL	Gauge length
H	
H-DRA	Hybrid distributed Raman amplification
I	
IF	Intermediate frequency
IFFT	Inverse fast Fourier transform
IOC	Integrated optical chip
ISO	Isolator
L	

LCF	Lorentz curve fitting
LEAF	Large effective area fiber
LMA	Levenberg-Marquardt algorithm
LO	Local oscillator
LPCM	Linear pulse-code modulation
LPG	Long–period grating
M	
MCF	Multi-core fiber
MI	Modulation instability
ML	Machine learning
MUX	Multiplexer
MZI	Mach–Zehnder interferometer
MZM	Mach–Zehnder modulator
N	
NLM	Non-local means
NRZ	Non-return-to-zero
O	
OCC	Optical chirp chain
OFDM	Orthogonal frequency division multiplexing
OFDR	Optical frequency domain reflectometry
OFS	Optical fiber sensor
OSC	Oscilloscope
OSNR	Optical signal-to-noise ratio
OTDR	Optical time domain reflectometry
P	
PC	Polarization controller
PCF	Photonic crystal fiber
PD	Photonic detector
PMF	Polarization-maintaining fiber
PPG	Pulse pattern generator
PPP	Pre-pump Pulse
PS	Polarization scrambler
PSW	Polarization switch
Φ-OTDR	Phase-sensitive optical time-domain reflectometry
R	
RF	Radio frequency
RFL	Random fiber laser

RFLA	High-order random fiber laser amplification
RMSE	Root-mean-square error
RPW	Red palm weevil
RZ	Return-to-zero

S

SBS	Stimulated Brillouin scattering
SD	standard deviation
SpBS	Spontaneous Brillouin scattering
SPM	Self-phase modulation
SpRS	Spontaneous Raman scattering
SHM	Structural health monitoring
SMF	Single-mode fiber
SNR	Signal-to-noise ratio
SOF	Specialty optical fiber
SOP	State of polarization
SRS	Stimulated Raman scattering
SSB	Single sideband
SVM	Support vector machine

T

TDM	Time-division multiplexing
TL	Tunable laser

V

VBM3D	Video block-matching and 3D filtering
VOA	Variable optical attenuator

W

WD	Wavelet denoising
WDM	Wavelength division multiplexing

1 Introduction

1.1 Overview of optical fiber sensing

Optical fiber sensors can be classified as single–point, quasi–distributed, and distributed sensors [1]. Initially, optic sensors were developed as pointwise sensors, which monitor environmental parameters at one location along the fiber. Various types of single–point fiber–optic sensors have been introduced, including grating–based sensors (fiber Bragg grating (FBG), long–period grating (LPG), etc.) and interferometric sensors (Fabry–Perot, Mach–Zehnder, etc.) [2]. Following the advancement of optical multiplexing, such as wavelength–, time–, and spatial–division multiplexing, arrays of discrete single–point sensors can be multiplexed along the fiber to form a quasi–distributed fiber–optic sensor [3]. In the oil and gas industry as an example, the single–point and quasi–distributed fiber–optic sensors have been deployed in many applications, primarily requiring discrete monitoring of acoustics, temperature, and/or pressure along pipelines or downhole, such as managing well drawdown, in–well pressure measurement to determine completion effectiveness, providing pressure build–up data, zonal production allocation, determination of productivity index, and monitoring during well ramp–up [4]–[6]. However, in terms of technology and cost, single–point and quasi–distributed fiber–optic sensors are not suitable for petroleum applications that require continuous spatial sensing, similar to downhole monitoring of hydrocarbon flow [7], fluid injection [8], wax buildup [7], and surveillance of leak detection along pipelines [9].

In contrast, distributed fiber–optic sensors can offer wealthy information by monitoring environmental parameters along the entire fiber length, i.e., the fiber itself is the sensor [1],[10]. Besides the aforementioned advantages of optical fibers, distributed fiber–optic sensors have another major benefit of reducing the overall sensing cost by measuring sensing parameters continuously and in real–time over tens of kilometers. In the upstream sector of oil and gas industry, distributed fiber–optic sensors are used for a wide range of applications such as seismic profiling [13], hydraulic fracture analysis [14], flow monitoring [9], casing leak detection [15], gas lift optimization [11], diagnosis [10], among others. This is achieved by installing optical fibers downhole to deliver data about the well and reservoir. On the other hand, distributed fiber–optic sensors can provide detection of intrusion [16], leak [17], and deformation [18] along a pipeline by attaching/placing the optical fiber to/near the pipeline’s surface.

The operation principles of distributed fiber–optic sensors, widely deployed in the oil and gas industry, are mainly based on optical scattering such as Rayleigh, Brillouin, or Raman scattering [19]. Generally, light scattering is a stochastic statistical process that occurs in all angular directions. A typical spectrum of spontaneous light scattering in a general medium is shown in Fig. 1.1, comprising Rayleigh, Brillouin and Raman scattering [1], [12]. It should be noted that, since silica is an isotropic medium, Rayleigh-wing scattering is not included in a typical spectrum of spontaneous light scattering in an optical fiber. During the fabrication process of optical fibers, silica molecules move in the molten state and then randomly freeze in place, which leads to fluctuations in density along the optical fiber. The density fluctuations cause random changes in the refractive index at a scale smaller than the optical wavelength, resulting in Rayleigh scattering. Rayleigh scattering is an elastic phenomenon, i.e., incident light does not transfer energy to the glass and there is no frequency shift between the incident and scattered light. In contrast, Brillouin and Raman scattering are produced by photon–phonon interaction, such that acoustic (optical) phonons are involved in Brillouin (Raman) scattering. Both Brillouin and Raman scattering are inelastic phenomena, in which the frequency of the scattered light is shifted from that of the incident light (Fig. 1.1). With respect to the central Rayleigh peak, the down– and up–shifted spectral components of Brillouin and Raman scattering are called Stokes and Anti–Stokes components, respectively. A last scattering phenomenon that can be observed in Fig.

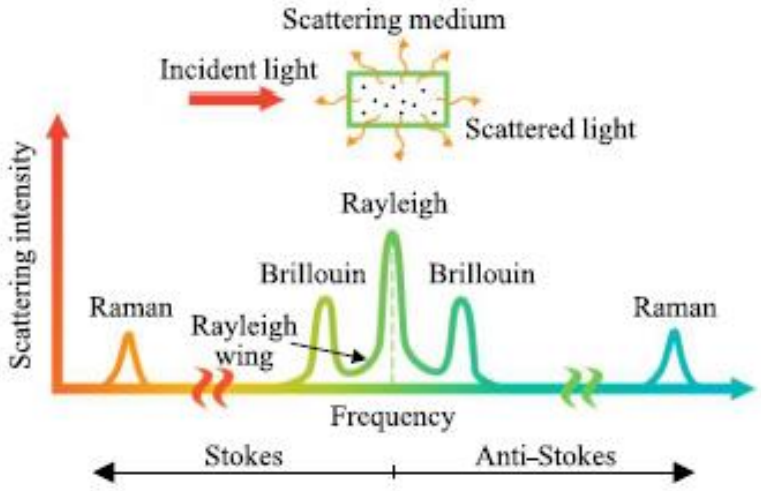

Fig. 1.1: A typical spectrum of spontaneous light scattering in a general medium.

1.1 is the Rayleigh–wing scattering, produced by fluctuations in the orientation of anisotropic molecules of the scattering medium [9].

Optical scattering can be classified as spontaneous or stimulated, based on the change in the optical properties of the medium during scattering. Spontaneous scattering typically occurs at low levels of incident light intensity, which do not alter the medium's optical properties. As the intensity of the incident light increases to a level at which the light changes the medium's optical properties, the scattering becomes stimulated. In other words, the transition from spontaneous to stimulated scattering corresponds to a change in the behavior of the medium from a linear to a nonlinear optical regime [17]. Both spontaneous and stimulated optical scattering offer various capabilities for distributed fiber–optic sensors used in the oil and gas industry and other applications.

1.2 Organization of the thesis

In this thesis, we focus on the application of some advanced signal processing techniques, including the neural networks and image processing methods in the distributed optical fiber sensing (DOFS). The aim is to promote the performance and make the DOFS more practical for the industry application, especially the oil and gas industry.

Chapter 1 gives an overview of optical fiber sensors (OFSs) and distributed optical fiber sensing (DOFSs). The classification of these optical fiber sensors is given, including some basic principles. Some application background in the industry, especially the oil and gas are mentioned to show the practical function of these sensing systems.

Chapter 2 gives the detailed introduction of the principles of three different types of scattering in the optical fiber. The DOFS based on these scattering (Rayleigh scattering, Brillouin scattering, and Raman scattering) are also introduced.

Chapter 3 introduces the first trial of using deep neural networks (DNN) for BOTDA to extract the temperature distribution. The simulation and experiment results prove the feasibility of this method.

Chapter 4 introduces the use of DNN for simultaneous temperature and strain measurement in BOTDA, which is very significant to make the BOTDA practical. The results show enhanced accuracy compared with conventional methods.

Chapter 5 introduces a new method to use the denoising autoencoder based DNN for fast and robust temperature distribution extraction in BOTDA. The key point is that the denoising autoencoder is adopted instead of normal autoencoder to construct the DNN model, which is inspired by the previous experiment process. The results show that the speed and robustness can be enhanced with this novel technique.

Chapter 6 introduces a very long-distance (about 100 km) BOTDA, achieved with the assistance of the Video-BM3D denoising method. During the previous research work, the denoising methods are expected to have good effects on the signals collected by the BOTDA system. Since the denoising effect of the DNN model has investigated previously, the more commonly used imaging denoising technique Video-BM3D is investigated here.

Both static and slowly varying environment has be taken into consideration and the results show excellent denoising effects of this technique.

Chapter 7 introduces the utilization of neural networks techniques including the artificial neural network (ANN) and convolutional neural networks (DNN) in the distributed acoustic sensing (DAS) system, or also known as phase-OTDR. DAS is a relatively new DOFS technique and has attracted a lot of research interest during recent several years. The reason why DAS is chosen to apply the neural network techniques is that it can generate a lot of data, which is very suitable to use the machine learning techniques as a pattern classification task. Very comprehensive comparative experiments have been conducted, which show the results with very high classification accuracy.

Chapter 8 gives the conclusion of this thesis. Besides, the challenges and future work direction of DOFS with novel advanced techniques are discussed for the practical use purpose.

References

[1] P. Lu, N. Lalam, M. Badar, B. Liu, B. T. Chorpening, M. P. Buric, and P. R. Ohodnicki, "Distributed optical fiber sensing: review and perspective." Applied Physics Reviews, vol. 6, no. 4, pp. 041302, 2019.

[2] M. Amanzadeh, S. M. Aminossadati, M. S. Kizil, and A. D. Rakic, “Recent developments in fibre optic shape sensing,” Measurement, vol. 128, pp. 119–137, 2018.

[3] D. A. Krohn, T. MacDougall, and A. Mendez, Fiber Optic Sensors: Fundamentals and Applications. Bellingham, WA, USA: SPIE Press, 2014.

[4] J. Dakin, "Multiplexed and distributed optical fibre sensor systems," J. Phys. E: Sci. Instrum., vol. 20, no. 8, 1987, Art. no. 954.

[5] M. R. Kabir, A. Ali, S. Pradhan, Q. Dashti, A. Al-Jasmi, and R. Abid, "Successful implementation of real time downhole pressure temperature monitoring using fiber optic technology in deep ht-hp well in north Kuwait," in Proc. Int. Petroleum Technol. Conf., 2014, pp. 1–11.

[6] Ö. H. Ünalmis and S. Trehan, "In-well, optical, strain-based flow mea- surement technology and its applications," in Proc. SPE Europec/EAGE Annu. Conf., 2012, pp. 1–18.

[7] C. S. Baldwin, "Applications for fiber optic sensing in the upstream oil and gas industry," in Proc. Fiber Opt. Sensors Appl. XII, vol. 9480. Bellingham, WA, USA, 2015, Art. no. 94800D.

[8] H. den Boer et al., "Flow monitoring and production profiling using das," in Proc. SPE Annu. Tech. Conf. Exhib., 2014.

[9] G. Naldrett, C. Cerrahoglu, and V. Mahue, "Production monitoring using next-generation distributed sensing systems," Petrophys. SPWLA.

[10] J. Formation Eval. Reservoir Description, vol. 59, no. 4, pp. 496–510, 2018.

[11] P. Stajanca, S. Chruscicki, T. Homann, S. Seifert, D. Schmidt, and A. Habib, "Detection of leak-induced pipeline vibrations using fiber-optic distributed acoustic sensing," Sensors, vol. 18, no. 9, 2018, Art. no. 2841.

[12] X. Bao and L. Chen, “Recent progress in distributed fiber optic sensors,” Sensors, vol. 12, no. 7, pp. 8601–8639, 2012.

[13] G. Naldrett, T. Parker, S. Shatalin, M. Mondanos, and M. Farhadiroushan, “High-resolution carina distributed acoustic fibreoptic sensor for perma- nent reservoir monitoring and extending the reach into subsea fields,” First Break, vol. 38, no. 2, pp. 71–76, 2020.

[14] M. Ichikawa et al., “Case study of hydraulic fracture monitoring using multiwell integrated analysis based on low-frequency das data,” Leading Edge, vol. 39, no. 11, pp. 794–800, 2020.

[15] K. Boone, A. Ridge, R. Crickmore, and D. Onen, “Detecting leaks in abandoned gas wells with fibre-optic distributed acoustic sensing,” in Proc. Int. Petroleum Technol. Conf., 2014, pp. 1–8.

[16] Z. Peng et al., “Distributed fiber sensor and machine learning data analytics for pipeline protection against extrinsic intrusions and in- trinsic corrosions,” Opt. Express, vol. 28, no. 19, pp. 27277–27292, 2020.

[17] D. Inaudi and B. Glisic, “Long-range pipeline monitoring by distributed fiber optic sensing,” J. Press. Vessel Technol., vol. 132, no. 1, 2010, Art. no. 011701.

[18] S. Zhang, B. Liu, and J. He, “Pipeline deformation monitoring using distributed fiber optical sensor,” Measurement, vol. 133, pp. 208–213, 2019.

[19] A. Rogers, “Distributed optical-fibre sensing,” Meas. Sci. Technol., vol. 10, no. 8, 1999, Art. no. R75.

[20] R. W. Boyd, “Nonlinear Optics,” Cambridge, MA, USA: Academic Press, 2020.

2 Distributed optical fiber sensing based on three scattering

In this chapter, the working principles are given in detail of DOFSs, which can be classified as three different types based on three kinds of optical scatterings in the fiber. These three scatterings have different physical principles, determining that they can be used for different measurements. Generally, the Rayleigh–based DOFS can be used for distributed acoustic sensing (DAS), Brillouin–based DOFS can be used for distributed temperature and strain sensing (DTSS), and Raman–based DOFS can be used for distributed temperature sensing (DTS).

2.1 Distributed optical fiber sensing based on Rayleigh scattering

The Rayleigh–based optical fiber DAS is achieved by the phase–sensitive optical time domain reflectometer (Φ–OTDR), which was described firstly in [1–4]. The working principle of this optical fiber DAS is very similar to the conventional OTDR [5]. Generally, the only key difference is adopting a laser source with a narrow linewidth and a stable frequency in Φ–OTDR. In other words, the successful operation of the DAS system depends on the use of a laser source with a much longer coherence length than the used fiber under test (FUT). Most commercial optical fiber DAS systems utilize the direct detection method (Fig. 2.1(a)), which makes the setups of sensing system relatively simple [5], [6]. In this setup, a narrow linewidth laser source generates a continuous wave (CW) light. The CW light is then converted into optical pulses using a modulator, such as electro-optic modulator (EOM) or acousto-optic modulator (AOM), driven by a function generator. Then, an erbium-doped fiber amplifier (EDFA) amplifies the power of the modulated optical pulses, which are injected into a single–mode fiber (SMF) via a circulator. As the optical pulses propagate along the SMF, Rayleigh signals are backscattered and directed through via a circulator into another EDFA. The EDFA's amplified spontaneous emission (ASE) noise is then removed using a filter, and finally the Rayleigh signals after filtering are detected by a photodetector (PD) and then collected by a data acquisition device (DAQ). Strictly speaking, this Φ-OTDR system setup can be called distributed vibration sensing (DVS), but not DAS, since it can not quantify the outside perturbation. However, the DAS has a wider understanding in the relevant application fields and are used to represent both DAS and DVS commonly. Thus, we will continue to use the name DAS in the following content while we are clear about its actual meaning.

The operation principle of DAS can be expressed by dividing the length (L) of the optical fiber into cascaded N small sections, such that each section length $\Delta L = L/N$ (Fig. 2.1(b)) [7], [8]. In this model, it is reasonable to set ΔL equals the width of the optical pulse. Due to the density fluctuations along the optical fiber, it is assumed that each section contains M independent Rayleigh scattering centers. At the PD position, the interference field E^i of the returned Rayleigh light generated from the i^{th} section can be expressed as:

$$E^{i} = E_{0} e^{-2\alpha L_{i}} \sum_{k=1}^{M} r_{k}^{i} e^{j\phi_{k}^{i}} \tag{2.1}$$

where E_0 is the electric field of the incident light, α is the attenuation coefficient of the fiber, L_i is the distance between the input port of the optical fiber to the location of the i^{th} section, i.e., $L_i = i\Delta L$, $i = 1, 2, \ldots, N$. The scattering coefficient and phase of the k^{th} scattering center in the i^{th} section are represented by r_k^i and φ_k^i, respectively. Eq. (2.1) can show that the i^{th} section's Rayleigh backscattered intensity $I^{i} \propto |E^{i}|^{2}$ is linked to the relative phases of light reflected from the individual scattering centers within the i^{th} section. Since the scattering centers are spatially randomly distributed within a section of the fiber, the fiber optic DAS has a Rayleigh speckle–like profile of random intensities along its length, as shown in the representative example of Fig. 2.1(c) for a 2–km–long standard SMF.

When there is no intrusion along the FUT, i.e., no refractive index perturbation along the fiber, the recorded Rayleigh traces remain ideally identical in the time–domain. In the case where an acoustic signal is applied at a position along the FUT, the relative phases of the backscattered light at that position change, resulting in temporal intensity fluctuations of the Rayleigh traces only at that perturbation position. The location of the acoustic event along the FUT can be identified by applying the differential method, in which consecutive temporal Rayleigh traces are subtracted from an initial reference one [9]. In addition, the frequency components of the acoustic event can be calculated by applying the fast Fourier transform to the resulting differential signal at the perturbation position.

Although the direct detection method is simple, as shown in Fig. 2.1(a), it has the drawback that the Rayleigh differential intensity varies nonlinearly with the strain induced by an acoustic event [8]. In other words, the strain along the FUT cannot be properly quantified. In case an application, such as wellbore seismic acquisition, strictly

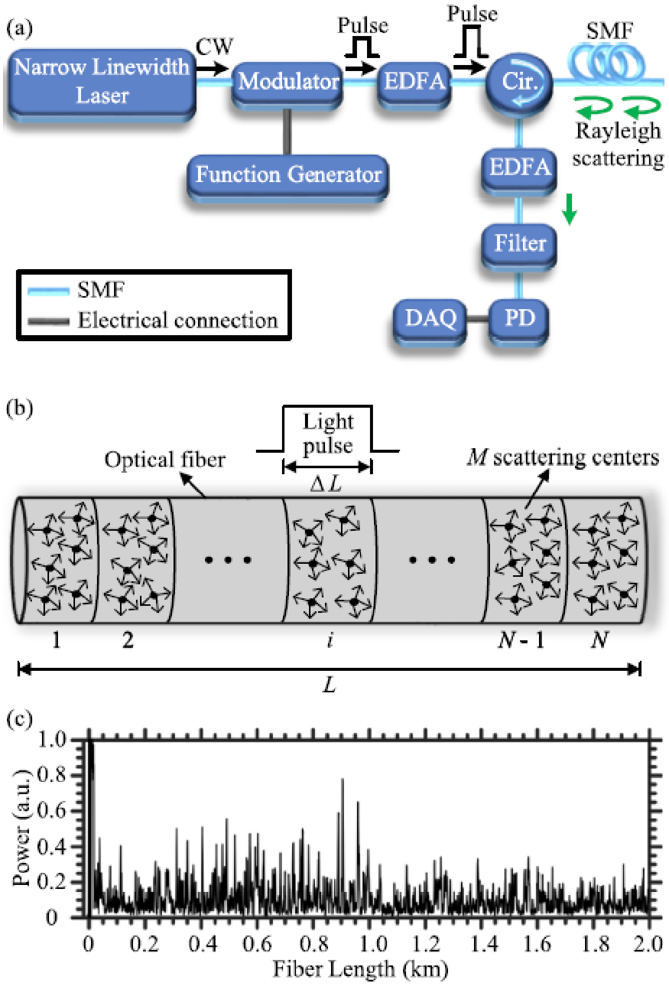

Fig. 2.1: (a) Experimental setup of the fiber–optic DAS with the direct detection method. (b) Schematic of modeling the operation of the fiber–optic DAS. (c) Representative example of a Rayleigh trace, recorded using a fiber–optic DAS. Cir., circulator.

requires quantifying the strain along the FUT, differential phase calculation should be adopted instead of the differential intensity measurement. The differential phase varies linearly with the strain; however, calculating the differential phase requires the use of more sophisticated optical systems and signal processing methods. For example, interferometric recovery [10], coherent detection [11], [12], dual–pulse [1], or chirped–pulse [13] scheme can be used for calculating the differential phase.

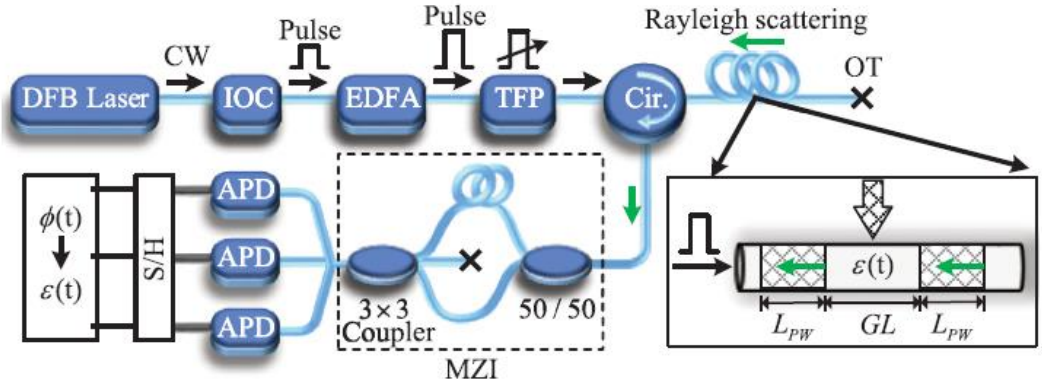

Fig. 2.2. Experimental setup of the fiber-optic DAS with the interferometric scheme for recovering the differential phase.

As a representative example, we describe the operation principle and experimental setup of the interferometric scheme for recovering the differential phase of a fiber–optic DAS (Fig. 2.2) [10]. As Fig. 2.2 shows, the system comprises a distributed feedback (DFB) laser that generates a CW light, which is modulated into optical pulses via an integrated optical chip (IOC). The optical pulses are then amplified with an EDFA, where its ASE noise is filtered out using a tunable Fabry–Perot filter (TFP). The amplified and filtered optical pulses are then launched throughout a circulator into a sensing fiber, whose end is optically terminated (OT) to prevent back reflections. The backscattered Rayleigh light is directed toward an unbalanced Mach–Zehnder interferometer (MZI), which mixes the backscattered light from two separate regions along the sensing fiber to extract the differential phase between them. The optical pulse–width determines the length of the scattering region (L_{PW}), while the gauge length (*GL*) is half the interferometer optical path imbalance. To avoid phase signal fading [14], a 3×3 output coupler is used for the MZI such that the interferometer has a 2π/3 relative phase difference between the output arms of the 3×3 coupler. The three output signals from the MZI are detected with avalanche photodiodes (APDs), sampled with a sample and hold amplifier (S/H), and processed for differential phase extraction along the fiber.

Demodulating the differential phase $\Delta\varphi(l)$ for any given fiber section of length l is well explained in [14], [15]. The light intensity at the three output arms of the MZI can be expressed as:

$$\begin{aligned} I_1 &= I_0\left[M + N\cos\left(\Delta\phi(l)\right)\right], \\ I_2 &= I_0\left[M + N\cos\left(\Delta\phi(l) + \frac{2\pi}{3}\right)\right], \\ I_3 &= I_0\left[M + N\cos\left(\Delta\phi(l) - \frac{2\pi}{3}\right)\right], \end{aligned} \tag{2.2}$$

where I_0 is the intensity of the input signal, and M and N are constants. Using trigonometric identities and some mathematical manipulation, $\Delta\varphi(l)$ can be extracted as:

$$\Delta\phi(l) = \arctan\left(\frac{\bar{I}_2 - \bar{I}_3}{\bar{I}_1}\right) \tag{2.3}$$

where $\bar{I}_i, i = 1, 2, or\ 3$, is the intensity of light at the detector less its DC component. Once *Δφ(l)* is demodulated, the strain (*ε*) applied on the fiber section can be estimated using the equation below:

$$\Delta\phi(l) = \epsilon l \beta \times 0.78 \tag{2.4}$$

where *β* is the propagation constant of light in the fiber.

It is important to highlight that the operation of DAS system that measures differential intensity/phase relies on spontaneous Rayleigh scattering. It is recommended to increase the peak power of the short optical pulses used in the DAS to extend the sensing range when maintaining a high spatial resolution. However, the peak power of the pulses should not exceed a threshold beyond which nonlinear phenomena occur within the fiber, such as self–phase modulation (SPM) and modulation instability (MI) which are generally the first nonlinear effects to degrade DAS measurements [16-18]. The threshold power of nonlinearity relies on the details of the optical pulses and fiber type.

2.2 Distributed optical fiber sensing based on Brillouin scattering

Brillouin–based DOFSs have been rapidly developed over the past 30 years [1], after their first proposal in 1989 [19-21]. The optical fiber DTSS can be achieved via one of two systems: Brillouin optical time–domain reflectometry (BOTDR) [22] and Brillouin optical time–domain analyzer (BOTDA) [23]. The operation principles of BOTDR and BOTDA are based on spontaneous Brillouin scattering (SpBS) and SBS, respectively. BOTDR has the advantage of having a simple experimental setup, with only one FUT pumping end, making it more convenient to deploy. In contrast, the BOTDA scheme is relatively complex and requires two FUT pumping ends. Nevertheless, BOTDA has a higher SNR than BOTDR, due to the essential principle of SBS with its higher power compared to SpBS [24].

A typical BOTDR experimental setup with heterodyne detection method is shown schematically in Fig. 2.3(a) [25]. A narrow linewidth laser generates a CW light that is divided by a coupler into two paths, a pump light and a local oscillator (LO) light. The pump light is modulated to optical pulses via an EOM driven by a function generator.

The optical pulses are then amplified with an EDFA and launched into a SMF through a circulator. As the pump pulses propagate along the SMF, SpBS signal is backscattered.

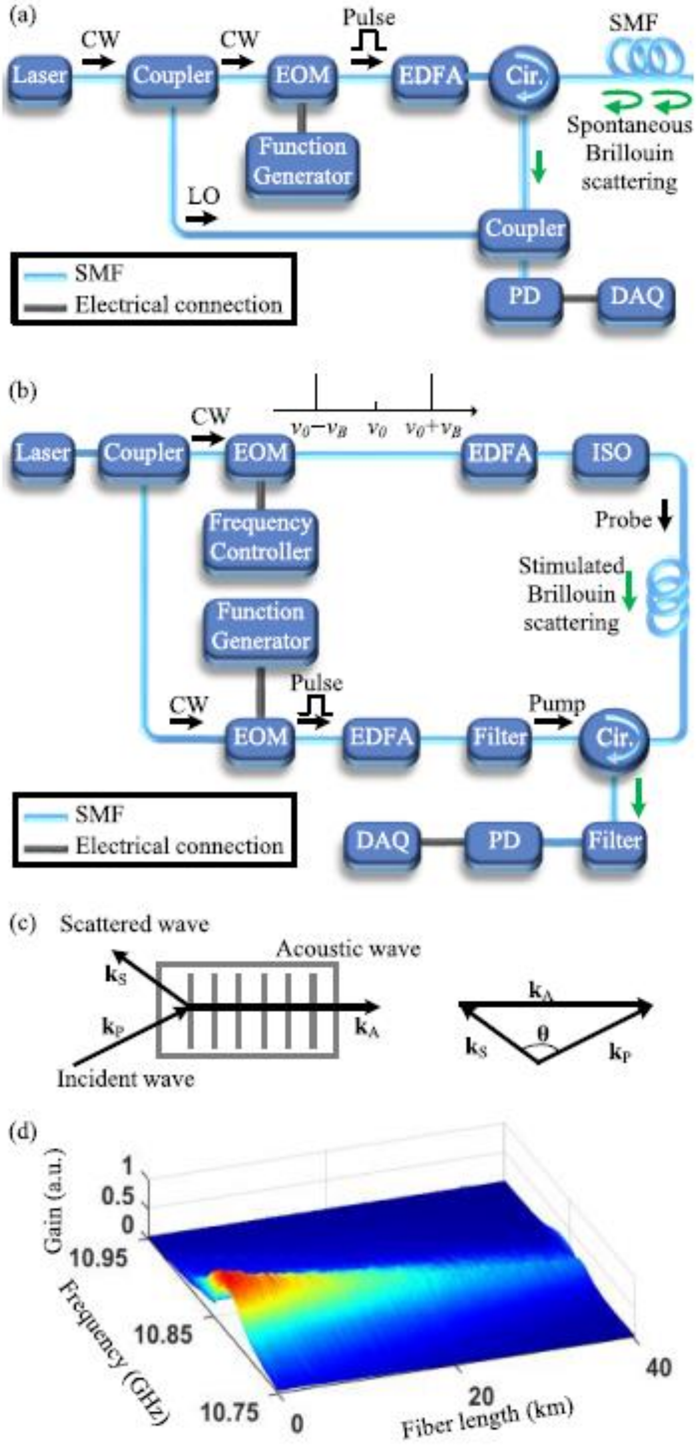

Fig. 2.3: Experimental setup of the BOTDR (a) and BOTDA (b). (c) Brillouin scattering in the Bragg diffraction regime. (d) Representative example of measured BGSs along a FUT.

The backscattered signal is directed via the circulator to be mixed with the LO light inside another coupler to generate a Brillouin beat–signal, which frequency is around 11 GHz with the commonly used 1550 nm light source and SMF. The Brillouin beat–signal is then detected and recorded by a PD and a DAQ, respectively.

In contrast, the typical BOTDA system is shown in Fig. 3.2(b) [26], where the CW light output from a narrow linewidth laser is split into two branches by a coupler. The light at the upper branch is modulated by an EOM biased at the null–point to suppress the optical carrier and driven by a frequency controller to provide the probe light. The probe light is amplified with an EDFA and then injected into a SMF after passing through an isolator (ISO), which blocks the light in the reverse direction. At the lower branch, the CW light is modulated by another EOM to generate pump pulses. The pump pulses are also amplified with another EDFA whose ASE noise is discarded by a filter. Then, the pump pulses are injected into the SMF in the reverse direction to amplify the probe light along the SMF via the SBS effect. The amplified probe signal is then spectrally filtered to remove its high-frequency sideband, detected by a PD, and recorded with a DAQ.

In the mechanism of SpBS, only one incident pump light enters the medium and a scattered Brillouin Stokes light of a lower frequency is generated. SpBS is caused mainly by thermally generated acoustic phonons, which has relatively weak intensity [24]. On the contrary, in the SBS mechanism, two lights of different frequencies enter the medium in the reverse direction. The energy is transferred from the pump light to the lower frequency Brillouin Stokes (probe) light. SBS is caused by the electrostriction from the interference of these two lights, which significantly enhances the thermally generated sound wave [24].

Generally in Brillouin scattering, the pump light of frequency ν_P (wave vector k_P), the scattered light of frequency ν_S (wave vector k_S), and the acoustic wave of frequency ν_A (wave vector k_A) satisfy the Bragg condition for energy and momentum fiber. As it can be derived from Equ. (2.4) and (2.5), the forward direction scattering vanishes while only the backscattered light "survives". The acoustic wave frequency ν_A represents the frequency difference between the pump light and the scattered light, also commonly called the Brillouin frequency shift (BFS) ν_B, which can be expresses as [27]:

$$\nu_P = \nu_S + \nu_A \tag{2.5}$$

$$k_P = k_S + k_A \tag{2.6}$$

As shown in Fig. 2.3(c), the Brillouin scattering process can be described as a scattering of light in a diffraction grating moving at the velocity of sound. Generally, the Brillouin scattering can occur in all angular directions. However, only the forward and backward directions are allowed for transmission in the optical fiber. As it can be derived from Eqs. (2.5) and (2.6), the forward direction scattering vanishes while only the backscattered light "survives". The acoustic wave frequency ν_A represents the frequency difference between the pump light and the scattered light, also commonly called the Brillouin frequency shift (BFS) ν_B, which can be expresses as [27]:

$$\nu_A = \nu_B = \frac{2n\nu_A}{\lambda_P}, \tag{2.7}$$

where n is the effective refractive index of fiber, V_A is the velocity of the acoustic wave, and λ_P is the pump light wavelength in vacuum. Thus, the BFS depends on the intrinsic properties of the optical fiber (n and V_A), which are functions of strain and temperature. It has been found that the BFS in optical fibers is linearly related to the strain (S) and temperature (T), i.e., [28]:

$$\nu_B(S,T) = C_S \cdot \Delta S + C_T \cdot \Delta T + \nu_B(S_0, T_0), \tag{2.8}$$

where $\Delta\nu_S$ and $\Delta\nu_T$ denote respectively the strain and temperature change, C_S (C_T) is the BFS strain (temperature) coefficient, and $\nu_B(S_0, T_0)$ is a reference BFS measured at predetermined strain S_0 and temperature T_0. When the acoustic wave decays exponentially, the Brillouin gain spectrum (BGS) has a Lorentzian lineshape [28]:

$$g(\nu) = \frac{g_B}{1 + [(\nu - \nu_B)/(\Delta\nu_B/2)]^2} \tag{2.9}$$

where $g(\nu)$ represents the Brillouin gain, ν is the frequency difference between the pump light and scattered light, g_B is the Brillouin peak gain, and $\Delta\nu_B$ is the Brillouin gain bandwidth.

The local BGSs along the whole FUT can be obtained using any of the BOTDR and BOTDA systems, as shown in the representative example of Fig. 3.2(d). Since the BFS is the central frequency of the BGS, Lorentzian curve fitting (LCF) can be used to estimate the BFS value [29]. Thus, using Eq. (2.8), the strain and temperature along the FUT can be measured.

In practical applications, to distinguish between temperature and strain, techniques based on Rayleigh or Raman scattering can be combined with Brillouin–based DTSS systems for tem- perature and strain separation [30], [31]. In addition, a sensing fiber can be used with a specially designed strain–isolating jacket to obtain the temperature profile separately. Then, the strain information can be collected using another typical sensing fiber with compensation using the separately measured temperature [31]. Furthermore, measuring BFS together with Brillouin intensity, bandwidth, or birefringence can provide temperature and strain information separately [32-34]. Besides, some specialty optical fibers (SOF) that provide several BFSs can be utilized for the temperature and strain discrimination, including multi–core fiber (MCF) [35], photonic crystal fiber (PCF) [36], large–effective–area fiber (LEAF) [37], dispersion compensating fiber (DCF) [38], and few–mode fiber (FMF) [39].

It is worth highlighting that the forward Brillouin scattering (FBS), also known as the guided acoustic–wave Brillouin scattering (GAWBS) has also been investigated for sensing purposes recently [40-46]. The typical Brillouin–based distributed fiber–optic sensors are based on backward spontaneous/stimulated Brillouin scattering, which involves the interaction of the injected light with the longitudinal acoustic waves in optical fibers. In contrast, the GAWBS relies on the acoustic waves of radial or torsional–radial modes, which propagate in the radial and circumferential directions instead of the longitudinal direction in fibers [45], [46]. The scattered spectrum of GAWBS contains dozens of peaks at frequencies below 1 GHz, which is also different from that of the backward Brillouin scattering. It is difficult for the sensors based on backward Brillouin scattering to detect ambient measurands that do not directly perturb the fiber core. For example, the BFS of the backward Brillouin scattering is not affected by ambient acoustic impedance. However, the surrounding medium affects the boundary conditions of the acoustic waves at the outer boundary of the fiber cladding, and thus affects the GAWBS. As a result, using a standard SMF, GAWBS can be used to measure the acoustic impedance of the ambient medium along with temperature and strain. Then the acoustic impedance can be used to analyze chemical species, e.g., the type and concentration of solutions [40], [41], which is a unique advantage of GAWBS. GAWBS–based sensors may be deployed for underground oil layer detection and other potential applications in the oil and gas industry in the future. However, it still needs some development to become reliable, due to the challenges of achieving long– distance distributed sensing and the requirement of having a bare fiber to provide direct contact with the surrounding medium.

2.3 Distributed optical fiber sensing based on Raman scattering

The concept of DTS using Raman scattering was first introduced in 1984 [47]. Commercially available Raman–based DTS systems typically use Raman intensity variations to determine the temperature profile along an optical fiber. The low power of the Stokes and Anti–Stokes Raman signals (60–70 dB weaker than the input pump power) is considered an early obstacle to the deployment of Raman–based DTS [48]. However, with the development of high–power lasers, EDFAs, high–sensitivity APD, and signal processing (e.g., averaging and wavelet denoising), the signal–to–noise ratio (SNR) of the Raman–based DTS has been significantly improved.

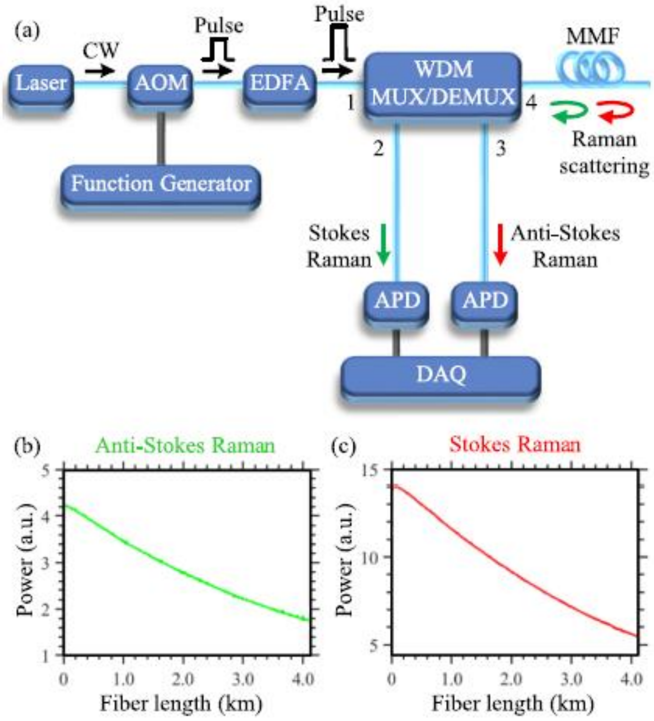

Fig. 2.4: (a) Experimental setup of a Raman–based fiber–optic DTS system. Representative examples of Anti–Stokes (b) and Stokes (c) Raman signal, recorded at room temperature.

A typical experimental setup of the Raman–based optical fiber DTS is schematically shown in Fig. 2.4(a) [49]. A high–power laser generates a CW light that is modulated into optical pulses using an AOM. The power of the optical pulses is then amplified with an EDFA, to improve the SNR of the DTS system. The EDFA is followed by a 3×1 wavelength division multiplexer/demultiplexer (MUX/DEMUX). One side of the wavelength division MUX/DEMUX includes three ports (Port 1–3) for adding/dropping signals of wavelengths matching the laser, Stokes Raman, and Anti–Stokes Raman signal, respectively. The other side of the wavelength division MUX/DEMUX includes a common port (Port 4) that simultaneously supports propagating the laser, Stokes Raman, and Anti-Stokes Raman signal. The amplified optical pulses are delivered to a MMF such that the pulses are directed from Port 1 to Port 4 of the wavelength division MUX/DEMUX. As the optical pulses propagate along the MMF, Stokes and Anti–Stokes Raman signals are backscattered, as shown in Fig. 3.3(a). In the backward direction, the two backscattered Raman signals can be well separated via the wavelength division MUX/DEMUX, detected using two separate APDs, and finally recorded with a DAQ. Fig. 2.4(b) and (c) show respectively representative examples of Anti–Stokes and Stokes Raman signal recorded using a standard 50/125 µm MMF, entirely placed at room temperature.

At the APDs, the received Raman Stokes power $P_S(z)$ and anti–Stokes power $P_{AS}(z)$ from a position z along the fiber can be expressed as [1]:

$$P_S(z) = R_S(z) e^{-(\alpha_p + \alpha_S)z} P_0 \tag{2.10}$$

$$P_{AS}(z) = R_{AS}(z) e^{-(\alpha_p + \alpha_{AS})z} P_0 \tag{2.11}$$

where $R_S(z)$ and $R_{AS}(z)$ are respectively the Stokes and anti–Stokes scattering coefficients at the position z, the attenuation coefficients of the pump, Stokes and Anti–Stokes light are denoted as α_p, α_S, and α_{AS}, respectively, and P_0 represents the laser power. As described by the Bose–Einstein statistics, $R_S(z)$ and $R_{AS}(z)$ are proportional to their differential cross sections as follows [50]:

$$R_S \propto \frac{d\sigma_S}{d\Omega} \cong \frac{1}{\lambda_S^4} \frac{1}{1-\exp\left[-\frac{hc\Delta\nu}{K_B T(z)}\right]} \tag{2.12}$$

$$R_{AS} \propto \frac{d\sigma_{AS}}{d\Omega} \cong \frac{1}{\lambda_{AS}^4} \frac{1}{\exp\left[\frac{hc\Delta\nu}{K_B T(z)}\right]-1} \tag{2.13}$$

where λ_S and λ_{AS} denote respectively the wavelengths of the Stokes and anti–Stokes light, h is the Planck's constant, c represents the speed of light in vacuum, K_B is the Boltzmann constant, $\Delta\nu$ is the Raman shift, and T is the temperature. The ratio $R(z)$ of the two backscattered Raman powers is independent of the laser power or the optical coupling efficiency:

$$\begin{aligned} R(z) &= \frac{P_{AS}(z)}{P_S(z)} \\ &= \left(\frac{\lambda_{AS}}{\lambda_S}\right)^4 \exp(-\alpha_{AS}z+\alpha_S z)\exp\left(-\frac{hc\Delta\nu}{K_B T(z)}\right) \end{aligned} \tag{2.14}$$

In practical applications, the stability of the DTS system's components may change with the environment. Hence, one usually does not use (2.14) directly to calculate the temperature, but instead a known reference temperature $T(z_0)$ at a position z_0 is introduced as follows:

$$\frac{1}{T(z)}-\frac{1}{T(z_0)}=\frac{-K_B}{hc\Delta\nu}\Big[\ln\frac{P_{AS}(z)}{P_S(z)}-\ln\frac{P_{AS}(z_0)}{P_S(z_0)} + (\alpha_{AS}-\alpha_S)(z-z_0)\Big] . \tag{2.15}$$

Eq. (2.15) can be used for determining the temperature $T(z)$ as long as the sensor operates in the spontaneous Raman scattering regime. Stimulated Raman scattering does not follow the Bose–Einstein statistics and cannot be used for distributed temperature sensing. Since the Raman scattering is weak and considering Eqs. (2.10) and (2.11), it is necessary to increase the power of the pump laser to collect a sufficient number of Raman photons for measurement. However, the laser power in DTS cannot exceed the Stimulated Raman scattering threshold, which is proportional to the effective core area of the fiber [51].

In the harsh environment such as the downhole environment of the oil and gas industry, the optical fiber cable may be pumped, exposed to hydrogen or water, etc. Thus, in Eq. (2.13), the wavelength–dependent differential attenuation coefficient, $\Delta\alpha = \alpha_{AS}-\alpha_S$, may change over time and/or along the optical fiber cable. Using a fixed pre–calibrated value of $\Delta\alpha$ cannot produce accurate temperatures over time. Consequently, for temperature measurement downhole, it is necessary to periodically calibrate $\Delta\alpha$ or even calculate it before each measurement. A single–ended fiber configuration with a reference temperature sensor at the fiber end or a partially returned fiber configuration can be used to calibrate $\Delta\alpha$, which varies over time but independent of z. Otherwise, a double–ended fiber configuration can calibrate $\Delta\alpha$, even if $\Delta\alpha$ changes along the fiber and over time. More details on calibrating the $\Delta\alpha$ of optical fiber DTS system can be found in [52], [53].

References

[1] J. Dakin and C. Lamb, “Distributed fibre optic sensor system gb2222247a,” 1990.

[2] H. F. Taylor and C. E. Lee, “Apparatus and method for fiber optic intrusion sensing,” U.S. Patent 5,194,847, Mar. 1993.

[3] R. Juškaitis, A. Mamedov, V. Potapov, and S. Shatalin, “Distributed inter- ferometric fiber sensor system,” Opt. Lett., vol. 17, no. 22, pp. 1623–1625, 1992.

[4] R. Juškaitis, A. Mamedov, V. Potapov, and S. Shatalin, “Interferometry with Rayleigh backscattering in a single-mode optical fiber,” Opt. Lett., vol. 19, no. 3, pp. 225–227, 1994

[5] P. Lu et al., “Distributed optical fiber sensing: Review and perspective,” Appl. Phys. Rev., vol. 6, no. 4, 2019, Art. no. 041302.

[6] I. Ashry et al., “Normalized differential method for improving the signal- to-noise ratio of a distributed acoustic sensor,” Appl. Opt., vol. 58, no. 18, pp. 4933–4938, 2019.

[7] W. Seo, “Fiber optic intrusion sensor investigation,” Ph.D. dissertation, Texas A&M Univ., College Station, TX, USA, 1994.

[8] M. Ren, “Distributed optical fiber vibration sensor based on phase- sensitive optical time domain reflectometry,” Ph.D. dissertation, Univ. Ottawa, Ottawa, ON, Canada, 2016.

[9] X. Bao, D.-P. Zhou, C. Baker, and L. Chen, “Recent development in the distributed fiber optic acoustic and ultrasonic detection,” J. Lightw. Technol., vol. 35, no. 16, pp. 3256–3267, 2016.

[10] R. Posey, G. Johnson, and S. Vohra, “Strain sensing based on coherent Rayleigh scattering in an optical fibre,” Electron. Lett., vol. 36, no. 20, pp. 1688–1689, 2000.

[11] Z. Pan, K. Liang, Q. Ye, H. Cai, R. Qu, and Z. Fang, “Phase-sensitive OTDR system based on digital coherent detection,” in Proc. Asia Com- mun. Photon. Conf. Exhib., 2011, Art. no. 83110S.

[12] A. Hartog and K. Kader, “Distributed fiber optic sensor system with improved linearity,” US Patent 9,170,149, Oct. 27 2015.

[13] J. Pastor-Graells, H. F. Martins, A. Garcia-Ruiz, S. Martin-Lopez, and M. Gonzalez-Herraez, “Single-shot distributed temperature and strain track- ing using direct detection phase-sensitive OTDR with chirped pulses,” Opt. Express, vol. 24, no. 12, pp. 13121–13133, 2016.

[14] A. Masoudi, M. Belal, and T. Newson, “A distributed optical fibre dy- namic strain sensor based on phase-OTDR,” Meas. Sci. Technol., vol. 24, no. 8, 2013, Art. no. 085204.

[15] A. Masoudi and T. P. Newson, "High spatial resolution distributed optical fiber dynamic strain sensor with enhanced frequency and strain resolu- tion," Opt. Lett., vol. 42, no. 2, pp. 290–293, 2017.

[16] J. Toulouse, "Optical nonlinearities in fibers: Review, recent examples, and systems applications," J. Lightw. Technol., vol. 23, no. 11, 2005, Art. no. 3625.

[17] X. Hu et al., "The modulation instability induced temporal fluctua- tion of the optical pulses in optical fiber sensing systems," in Opti- cal Fiber Sensors. Washington, DC, USA: Opt. Soc. America, 2018, Art. no. WF50.

[18] O. H. Waagaard et al., "Real-time low noise distributed acoustic sensing in 171 km low loss fiber," OSA Continuum, vol. 4, no. 2, pp. 688–701, 2021.

[19] T. Horiguchi and M. Tateda, "BOTDA-nondestructive measurement of single-mode optical fiber attenuation characteristics using Brillouin in- teraction: Theory," J. Lightw. Technol., vol. 7, no. 8, pp. 1170–1176, 1989.

[20] D. Culverhouse, F. Farahi, C. Pannell, and D. Jackson, "Potential of stimulated Brillouin scattering as sensing mechanism for distributed temperature sensors," Electron. Lett., vol. 25, no. 14, pp. 913–915, 1989.

[21] T. Horiguchi, T. Kurashima, and M. Tateda, "Tensile strain dependence of Brillouin frequency shift in silica optical fibers," IEEE Photon. Technol. Lett., vol. 1, no. 5, pp. 107–108, May 1989.

[22] T. Kurashima, T. Horiguchi, H. Izumita, S.-I. Furukawa, and Y. Koya- mada, "Brillouin optical-fiber time domain reflectometry," IEICE Trans. Commun., vol. 76, no. 4, pp. 382–390, 1993.

[23] X. Bao, D. J. Webb, and D. A. Jackson, “22-km distributed temperature sensor using Brillouin gain in an optical fiber,” Opt. Lett., vol. 18, no. 7, pp. 552–554, 1993.

[24] R. W. Boyd, Nonlinear Optics. Cambridge, MA, USA: Academic Press, 2020.

[25] H. H. Kee, G. P. Lees, and T. P. Newson, “All-fiber system for simul- taneous interrogation of distributed strain and temperature sensing by spontaneous Brillouin scattering,” Opt. Lett., vol. 25, no. 10, pp. 695–697, 2000.

[26] H. Liang, W. Li, N. Linze, L. Chen, and X. Bao, “High-resolution DPP-BOTDA over 50 km leaf using return-to-zero coded pulses,” Opt. Lett., vol. 35, no. 10, pp. 1503–1505, 2010.

[27] G. P. Agrawal, “Nonlinear fiber optics,” in Proc. Nonlinear Sci. Dawn 21st Century, 2000, pp. 195–211.

[28] C. A. Galindez-Jamioy and J. M. Lopez-Higuera, “Brillouin distributed fiber sensors: An overview and applications,” J. Sensors, vol. 2012, 2012, Art. no. 204121.

[29] C. N. Pannell, J. Dhliwayo, and D. J. Webb, “The accuracy of parameter estimation from noisy data, with application to resonance peak estimation in distributed Brillouin sensing,” Meas. Sci. Technol., vol. 9, no. 1, p. 50, 1998.

[30] K. Kishida, Y. Yamauchi, and A. Guzik, “Study of optical fibers strain-temperature sensitivities using hybrid Brillouin-Rayleigh system,” Pho- tonic Sensors, vol. 4, no. 1, pp. 1–11, 2014.

[31] M. Alahbabi, Y. Cho, and T. Newson, “Simultaneous temperature and strain measurement with combined spontaneous raman and Brillouin scattering,” Opt. Lett., vol. 30, no. 11, pp. 1276–1278, 2005.

[32] S. M. Maughan, H. H. Kee, and T. P. Newson, “Simultaneous distributed fibre temperature and strain sensor using microwave coherent detection of spontaneous Brillouin backscatter,” Meas. Sci. Technol., vol. 12, no. 7, 2001, Art. no. 834.

[33] X. Bao, Q. Yu, and L. Chen, “Simultaneous strain and temperature measurements with polarization-maintaining fibers and their error analysis by use of a distributed Brillouin loss system,” Opt. Lett., vol. 29, no. 12, pp. 1342–1344, 2004.

[34] W. Zou, Z. He, and K. Hotate, “Complete discrimination of strain and temperature using Brillouin frequency shift and birefringence in a polarization-maintaining fiber,” Opt. Express, vol. 17, no. 3, pp. 1248–1255, 2009.

[35] Z. Zhao et al., “Spatial-division multiplexed Brillouin distributed sensing based on a heterogeneous multicore fiber,” Opt. Lett., vol. 42, no. 1, pp. 171–174, 2017.

[36] L. Zou, X. Bao, S. Afshar, and L. Chen, “Dependence of the Brillouin frequency shift on strain and temperature in a photonic crystal fiber,” Opt. Lett., vol. 29, no. 13, pp. 1485–1487, 2004.

[37] X. Liu and X. Bao, “Brillouin spectrum in leaf and simultaneous tem- perature and strain measurement,” J. Lightw. Technol., vol. 30, no. 8, pp. 1053–1059, 2011.

[38] Z. Li, L. Yan, X. Zhang, and W. Pan, “Temperature and strain discrimina- tion in BOTDA fiber sensor by utilizing dispersion compensating fiber,” IEEE Sensors J., vol. 18, no. 17, pp. 7100–7105, Sep. 2018.

[39] A. Li, Y. Wang, J. Fang, M.-J. Li, B. Y. Kim, and W. Shieh, “Few- mode fiber multi-parameter sensor with distributed temperature and strain discrimination,” Opt. Lett., vol. 40, no. 7, pp. 1488–1491, 2015.

[40] Y. Antman, A. Clain, Y. London, and A. Zadok, “Optomechanical sensing of liquids outside standard fibers using forward stimulated Brillouin scattering,” Optica, vol. 3, no. 5, pp. 510–516, 2016.

[41] N. Hayashi, Y. Mizuno, K. Nakamura, S. Y. Set, and S. Yamashita, “Experimental study on depolarized GAWBS spectrum for optomechanical sensing of liquids outside standard fibers,” Opt. Express, vol. 25, no. 3, pp. 2239–2244, 2017.

[42] N. Hayashi, Y. Mizuno, H. Lee, K. Nakamura, S. Y. Set, and S. Yamashita, “Characterization of cascaded forward Brillouin scattering seeded by backward stimulated Brillouin scattering in optical fibers,” IEICE Elec- tron. Express, 17, 2020, Art. no. 20200139.

[43] C. Pang et al., “Opto-mechanical time-domain analysis based on coherent forward stimulated Brillouin scattering probing,” Optica, vol. 7, no. 2, pp. 176–184, 2020.

[44] N. Hayashi et al., “Pilot demonstration of correlation-domain distributed temperature sensing using forward Brillouin scattering,” Japanese J. Appl. Phys., vol. 59, no. 8, 2020, Art. no. 088002.

[45] R. Shelby, M. Levenson, and P. Bayer, “Guided acoustic-wave Brillouin scattering,” Phys. Rev. B, vol. 31, no. 8, 1985, Art. no. 5244.

[46] A. J. Poustie, “Bandwidth and mode intensities of guided acoustic-wave Brillouin scattering in optical fibers,” J. Opt. Soc. Amer. B, vol. 10, no. 4, pp. 691–696, 1993.

[47] J. Dakin, “Temperature measuring arrangement,” U.K. Patent, GB2140554, 1984.

[48] M. A. Soto et al., “Raman-based distributed temperature sensor with 1 m spatial resolution over 26 km SMF using low-repetition-rate cyclic pulse coding,” Opt. Lett., vol. 36, no. 13, pp. 2557–2559, 2011.

[49] Y. Liu, L. Ma, C. Yang, W. Tong, and Z. He, “Long-range raman distributed temperature sensor with high spatial and temperature reso- lution using graded-index few-mode fiber,” Opt. Express, vol. 26, no. 16, pp. 20562–20571, 2018.

[50] M. Höbel, J. Ricka, M. Wüthrich, and T. Binkert, “High-resolution distributed temperature sensing with the multiphoton-timing technique,” Appl. Opt., vol. 34, no. 16, pp. 2955–2967, 1995.

[51] G. P. Agrawal, “Nonlinear fiber optics,” in Proc. Nonlinear Sci. Dawn 21st Century, 2000, pp. 195–211.

[52] G. A. Brown, The Essentials of Fiber-Optic Distributed Temperature Analysis. Houston, TX, USA: Schlumberger Educational Services, 2005.

[53] J. J. Smolen, “Distributed temperature sensing, a DTS primer for oil & gas production,” EP2003, 2003.

3 Temperature Extraction Using DNN for BOTDA

In this chapter, the technique of DNN is used for the first time to extract the temperature distribution in the BOTDA system. The feasibility is demonstrated experimentally, which is the beginning and foundation of the whole work in this thesis. After training the DNN model, temperature distribution along the whole FUT can be directly obtained from the experimental BGS data via DNN. It skips the processes of calculating BFS and transforming it to temperature involved in conventional curve fitting methods. The results of the DNN-based temperature extraction method show comparable accuracy to that of traditional LCF.

3.1 Motivation

Since T. Horiguchi and M. Tateda proposed the BOTDA for the first time in 1989 [1], it has attracted much research interest as one type of distributed fiber optic sensor. In the past three decades, much research work investigating better system solutions and more advanced signal processing methods in this field have been reported, aimed at achieving a higher performance of BOTDA systems, including smaller spatial resolution, longer measurement distance, and higher temperature/strain measurement accuracy [2-7]. The fundamental principle of the BOTDA sensing system is that the pump pulse light will transmit its power to the counter-propagating continuous wave known as probe light under the SBS effect if the frequency difference between them is around the BFS. Since the local change of BFS is proportional to the local temperature or strain change, the temperature or strain distribution information along the FUT could be calculated from the BFS distribution. In practice, the local BGSs can be obtained generally by sweeping frequency offset of the two interacting light waves around the estimated range of BFS. Then, the local BFSs are considered the central frequency of local BGSs, by applying the conventional curve fitting technique, e.g., LCF method on the collected data.

On the other hand, the DNN, known as a machine learning/deep learning method, has been a very hot topic in recent years. It has been used in extensive fields, including conventional speech recognition [8-10] and fiber optical communication, e.g., the modulation format identification task [11]. Compared with the ANN, the DNN has a simpler structure and training process. The DNN can learn abundant features automatically through a supervised/unsupervised feature learning process. At the same time, the ANN needs a more specifically designed structure, especially when the relationship and interlayers between the input and the targeted output are "deep". Recently, our group has demonstrated the work of an ANN-based temperature extraction method for BOTDA [12], showing the advantages of the ANN-based method over conventional curve fitting techniques. Considering that the DNN has even more potential benefits, here we decide to use DNN in replace of ANN for the temperature extraction task in our BOTDA system. The essential of this method is that the DNN can learn the non-linear relation between the BGS (input) and the temperature (output) after adequate training. In this section, the DNN is used for temperature distribution extraction, and comparable accuracy to conventional LCF is achieved.

3.2 Principle of DNN

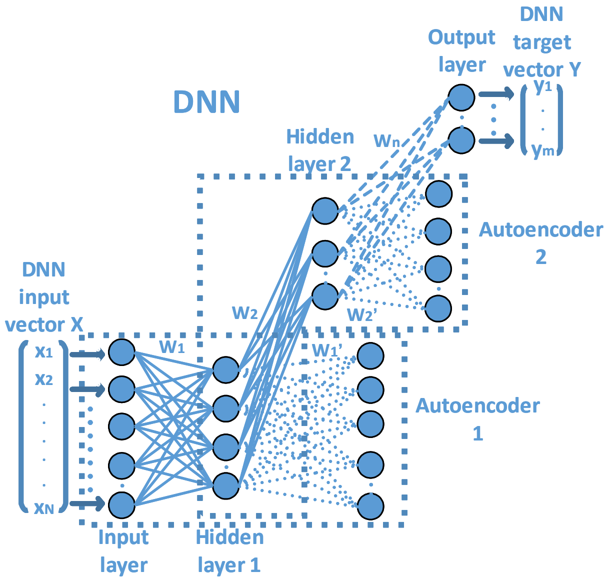

Fig. 3.1: The structure of DNN with 2 autoencoder hidden layers.

DNN is a computational model to simulate the learning process of human brains, where the information is transferred and processed by many parallel neurons layer by layer. The DNN structure, including two autoencoder hidden layers, is shown in Fig. 3.1. The DNN is constructed of one input layer, some hidden layers, and one output layer. Except for the input layer, each neuron (node) in the hidden layers or output layer has an output, which can be represented by:

$$y_j = f_j\left(\Sigma_i w_{ij} x_i - \theta_j\right). \tag{3.1}$$

Here y_j is the output of the j^{th} node. f_j is a nonlinear activation function. x_i is the i^{th} input to the node. w_{ij} is the adjustable weight connecting the input node i and the output node j. θ_j is the threshold of the j^{th} node, which is set as a constant typically. From this Equation, we can see that the output of each neuron has a linear/nonlinear relation with all neurons in the last layer. Hence the output of each neuron in the final output layer of this model has a nonlinear relation with the initial input vector. The number of neurons in each hidden layer usually decreases gradually, while the hidden layers (interlayers) extract the features.

The implementation of DNN consists of two stages: training and testing. In the training stage, firstly, each hidden layer and final output layer are trained with chosen activation functions and initial values of weight vectors layer by layer. The hidden layers are trained using the autoencoder method, which tries to make each autoencoder's output as close to its input as possible. The original input vector is used as the input of the first hidden layer, and the feature vector generated by each hidden layer serves as the input of the next hidden layer for training. In the end, the output layer is trained in a supervised way using the feature vector generated by the last hidden layer as its input, together with the targeted output vector. After all hidden layers and the output layer are trained step by step individually, the whole structure of the DNN model could be formed by cascading the input layer, the first half part of each autoencoder, and the backmost output layer. Then, prepared original input and targeted output data for training are used together to train the whole DNN model with the back-propagation (BP) algorithm in a supervised way called fine-tuning. Afterward, the DNN model is ready for testing since the training has been finished, while the DNN model has learned the nonlinear relation between the input and output. Subsequently, in the testing stage, collected experimental data are input into the DNN model, and the output will be generated fast by running the trained DNN model.

In our case, ideal BGS and T pairs are used as input and targeted output data for training. The specific number of elements in each input vector is determined by the frequency-sweeping range and sweeping step of the BOTDA experiment system. Besides, the output layer only contains one neuron representing the needed temperature information. In testing, experimental noisy BGS data along the FUT are input to the DNN model, and the temperature information will be generated as the output.

3.3 Experiment setup of the BOTDA system

The adopted BOTDA experiment system is shown in Fig. 3.2. The tunable laser generates CW light at 1550 nm. The CW light is amplified by the EDFA1 and filtered by the filter1. Then it splits into two branches via an 80/20 coupler. The upper one is modulated by the EOM1, biased at the null point to suppress the optical carrier, and

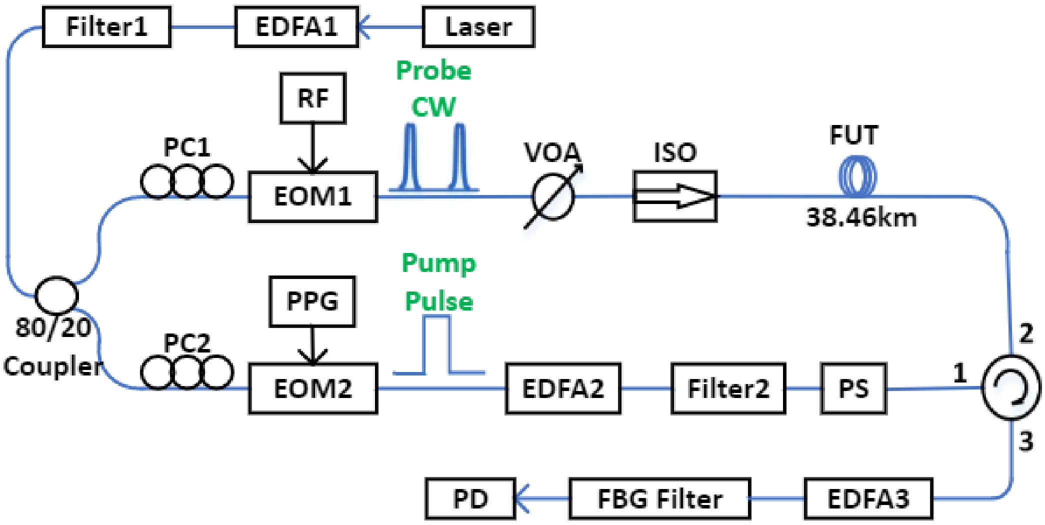

Fig. 3.2: BOTDA experiment setup, EDFA: erbium-doped fiber amplifier, PC: polarization controller, EOM: electro-optic modulator, RF: radio frequency, PG: pattern generator, VOA: variable optical attenuator, ISO: isolator, FUT: fiber under test, PS: polarization scrambler, FBG: fiber Bragg grating, PD: photodetector.

driven by an RF around BFS. A VOA controls the probe light power before entering the FUT. And an isolator is used to block the reverse light. At the lower branch, the CW light is modulated by the EOM2 with a pattern generator to generate a 20ns pump pulse, corresponding to the 2m spatial resolution. The EDFA2 amplifies the pump pulse's peak power, and the Filter2 removes the amplified spontaneous emission (ASE) noise from EDFA2. In addition, a polarization scrambler (PS) is used to suppress the polarization-dependent noise since the SBS effect is susceptible to polarization. The CW probe and pump pulse propagate in the opposite direction and interact under SBS along the FUT. Afterward, the CW probe signal is filtered through an FBG and detected by a 125 MHz photodetector. The local BGS along the FUT for final processing can be obtained by sweeping the frequency of probe light around the estimated BFS.

3.4 Results and discussions

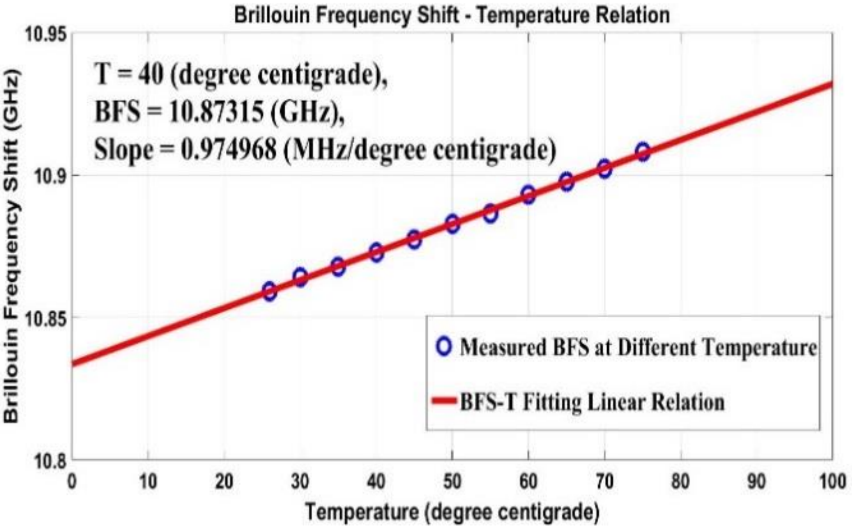

Fig. 3.3: The measured Brillouin frequency shift at different temperature and the fitting linear relation between them.

Before the temperature extraction utilizing DNN, the linear BFS-temperature relationship is measured experimentally. The corresponding coefficient is found to be 0.974968 MHz/ºC, as shown in Fig. 3.3. We use this BFS-temperature relationship and theoretical Lorentz curve to simulate ideal BGS data for DNN training as input. In contrast, the corresponding temperature is used as the targeted output. In the preparation of training data, the temperature range is from 0 to 100ºC, and the BGS under each temperature has a linewidth ranging from 40 to 70MHz at a 1MHz step, considering the practical linewidth variations. The 0.1ºC temperature step is chosen, which is adequate for training. Therefore, we have 31031 ideal BGS-temperature pairs for DNN training in total. The frequency sweeping ranges from 10.760 to 11.010GHz with a 1MHz frequency step. Thus, each input vector of our DNN model contains 251 elements, i.e., 251 neurons (nodes) in the DNN input layer. Since there is no specific rule about how many hidden layers should be adopted and how many neurons should be contained in each hidden layer, the optimization process of the DNN structure is the processing of repeated trials and adjustments. We find that the DNN model containing two hidden layers can provide better performance than that of 1 hidden layer, which is acceptable enough. A more significant number of hidden layers will bring much longer training time, increasing exponentially with the number of hidden layers but no noticeable performance improvement. Therefore, two hidden layers are determined in the finalized DNN model. Besides, after repeated trials, the numbers of neurons in the first and second hidden layers are determined to be 50 and 10. After the training of the DNN model, the measured local BGS data along 38.460 km FUT with the last 607m heated to different temperatures are given to the DNN input layer. The temperature distributions along the whole FUT with the last 607m fiber heated to 50ºC extracted by

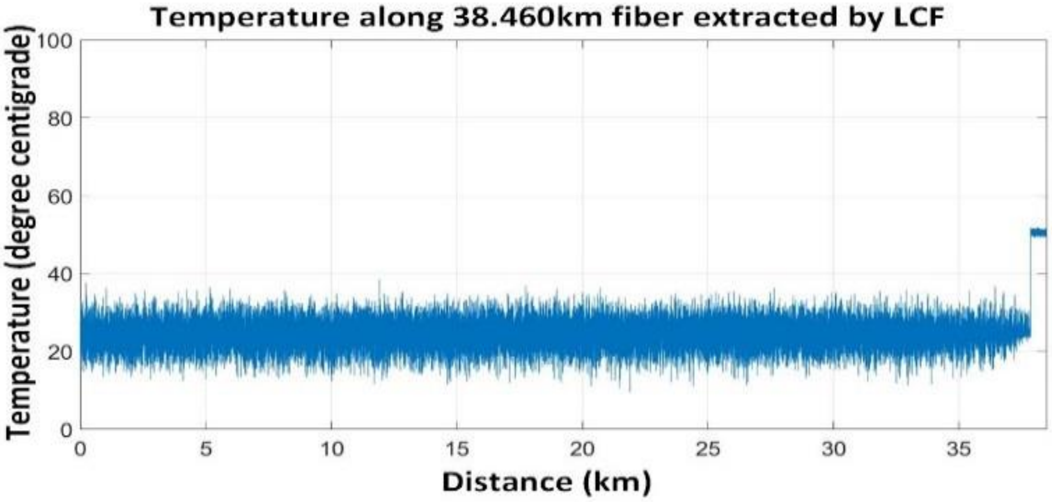

Fig. 3.4: Temperature distribution along the whole 38.460 km FUT with last 607 m fiber heated to 50 degrees centigrade extracted by LCF.

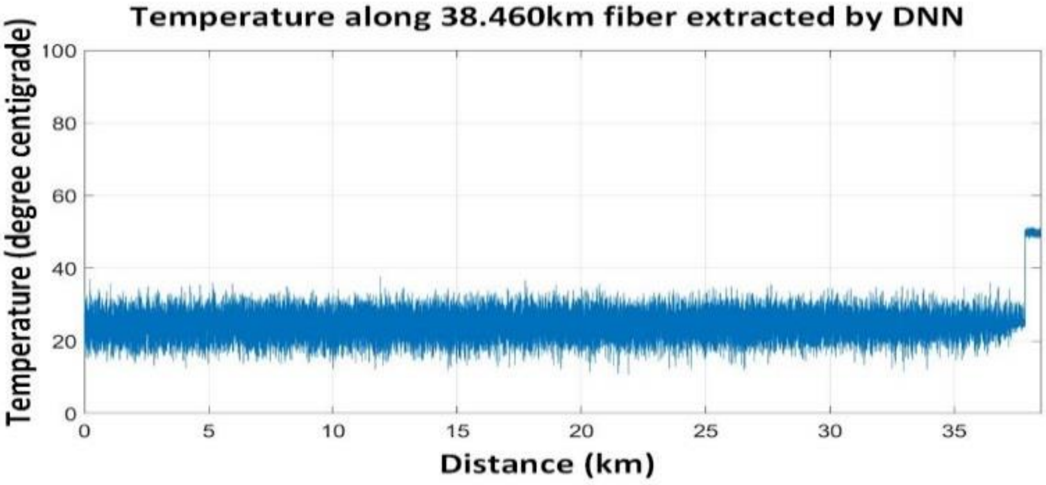

Fig. 3.5: Temperature distribution along the whole 38.460 km FUT with last 607 m fiber heated to 50 degrees centigrade extracted by DNN.

LCF and DNN are shown in Fig. 3.4 and Fig. 3.5, respectively.

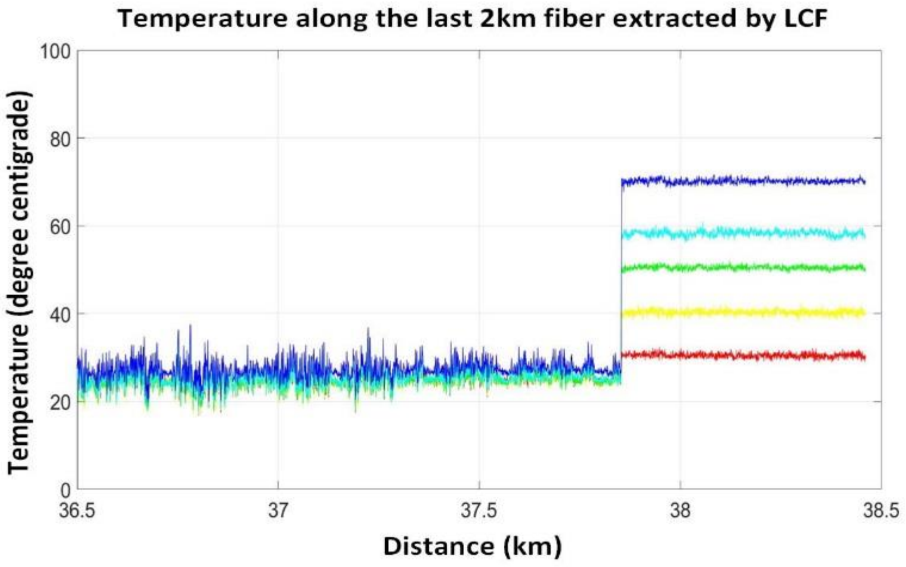

Fig. 3.6: The temperature distribution information in the last 2 kilometer fiber extracted by LCF.

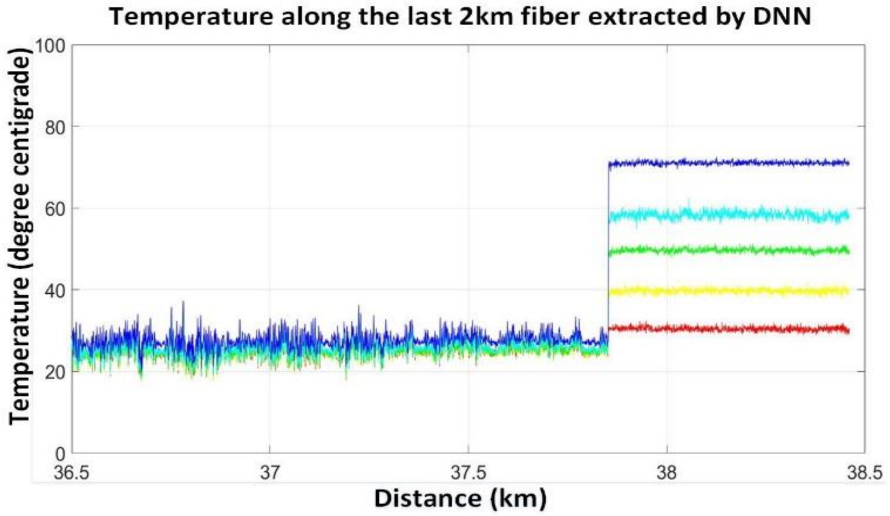

Fig. 3.7: The temperature distribution information in the last 2 kilometer fiber extracted by DNN.

Moreover, we also compare the results of using DNN and LCF, when the last fiber section is heated to 30, 40, 50, 60, and 70°C, respectively. The extracted temperature in the last 2 km FUT using LCF and DNN are shown in Fig. 3.6 and Fig. 3.7, respectively.

Table 3.1: Error performance comparison of DNN and LCF in last 607m heated fiber

Performance / Temperature	RMSE[a]		SD[b]	
	LCF	*DNN*	*LCF*	*DNN*
30	0.7533	0.6998	0.5578	0.5467
40	0.7015	0.6733	0.6172	0.6094
50	0.6769	0.6311	0.4683	0.5314
60	1.8465	1.9660	0.7354	0.9673
70	0.7387	1.2976	0.7234	0.7917

We can see that the temperature distribution extracted by DNN is as good as that by the LCF method. To show the comparison clearly, specific error performance, including root-mean-square error (RMSE) and standard deviation (SD) calculated in the last 607m heated fiber section, are shown in Table 3.1 for both LCF and DNN. Table 3.1 shows that the error performance of temperature extraction using LCF and DNN are pretty similar. The noise level of the collected experimental data is relatively low after large averaging times. Better performance of DNN is expected compared with LCF when the SNR becomes worse. Besides, the processing speed of DNN is much faster than the LCF (over 100 times), which is a significant advantage to reduce the integral data processing time for BOTDA. In the future, better performance of using DNN for temperature extraction is expected by increasing the extent of training and optimizing the structure of DNN.

3.5 Summary

We have demonstrated the temperature distribution extraction along the 38.46km FUT based on the DNN for our BOTDA system. The performance results of the DNN and conventional LCF methods show comparable temperature accuracy. Moreover, the DNN method can reduce the processing time significantly. Further investigation and optimization of the DNN model to explore other advantages and obtain better temperature accuracy for BOTDA will be conducted in the following.

References

[1] T. Horiguchi and M. Tateda, "BOTDA-nondestructive measurement of single-mode optical fiber attenuation characteristics using Brillouin interaction: theory," Journal of Lightwave Technology, vol. 7, no. 8, pp. 1170-1176, 1989.

[2] X. Bao and L. Chen, "Recent progress in Brillouin scattering based fiber sensors." Sensors, vol. 11, no. 12, pp. 4152-4187, 2011.

[3] Y. Dong, D. Ba, T. Jiang, D. Zhou, H. Zhang, C. Zhu, Z. Lu, H. Li, L. Chen and X. Bao, "High-spatial-resolution fast BOTDA for dynamic strain measurement based on differential double-pulse and second-order sideband of modulation," IEEE Photonics Journal, vol. 5, no. 3, pp. 2600407-2600407, 2013.

[4] A. Denisov, M. Soto and L. Thévenaz, "Going beyond 1000000 resolved points in a Brillouin distributed fiber sensor: theoretical analysis and experimental demonstration," Light: Science & Applications, vol. 5, no. 5, p. e16074, 2016.

[5] M. Soto, X. Angulo-Vinuesa, S. Martin-Lopez, S. Chin, J. Ania-Castanon, P. Corredera, E. Rochat, M. Gonzalez-Herraez and L. Thevenaz, "Extending the real remoteness of long-range Brillouin optical time-domain fiber analyzers," Journal of Lightwave Technology, vol. 32, no. 1, pp. 152-162, 2014.

[6] J. Mompó, J. Urricelqui and A. Loayssa, "Brillouin optical time-domain analysis sensor with pump pulse amplification," Optics Express, vol. 24, no. 12, p. 12672, 2016.

[7] R. Ruiz-Lombera, J. Urricelqui, M. Sagues, J. Mirapeix, J. Lopez-Higuera and A. Loayssa, "Overcoming nonlocal effects and Brillouin threshold limitations in Brillouin optical time-domain sensors," IEEE Photonics Journal, vol. 7, no. 6, pp. 1-9, 2015.

[8] Deng, Li, G. Hinton, and B. Kingsbury. "New types of deep neural network learning for speech recognition and related applications: An overview," 2013 IEEE International Conference on Acoustics, Speech and Signal Processing, 2013.

[9] G. Hinton, L. Deng, D. Yu, G. Dahl, A. Mohamed, N. Jaitly, A. Senior, V. Vanhoucke, P. Nguyen, T. Sainath and B. Kingsbury, "Deep neural networks for acoustic modeling in speech recognition: the shared views of four research groups," IEEE Signal Processing Magazine, vol. 29, no. 6, pp. 82-97, 2012.

[10] G. Dahl, D. Y. L. Deng and A. Acero, "Context-dependent pre-trained deep neural networks for large-vocabulary speech recognition," IEEE Transactions on Audio, Speech, and Language Processing, vol. 20, no. 1, pp. 30-42, 2012.

[11] F. Khan, K. Zhong, W. Al-Arashi, C. Yu, C. Lu and A. Lau, "Modulation format identification in coherent receivers using deep machine learning," IEEE Photonics Technology Letters, vol. 28, no. 17, pp. 1886-1889, 2016.

[12] A. Azad, L. Wang, N. Guo, H. Tam and C. Lu, "Signal processing using artificial neural network for BOTDA sensor system," Optics Express, vol. 24, no. 6, p. 6769, 2016.

4 DNN-assisted BOTDA for Simultaneous Temperature and Strain Measurement with Enhanced Accuracy

This chapter demonstrates simultaneous temperature and strain measurement with enhanced accuracy using DNN-assisted BOTDA. After training using combined ideal clean and noisy BGSs, the DNN is applied to extract the temperature and strain directly from the measured double-peak BGS in large-effective-area fiber (LEAF). Both simulated and experimental data under different temperature and strain conditions have been used to verify the reliability of DNN-based simultaneous temperature and strain measurement, demonstrating its advantages over BOTDA with the conventional equation-solving method. Avoiding the significant error induced by the minor matrix determinant, our DNN approach significantly improves the measurement accuracy. For 24km LEAF sensing fiber with a spatial resolution of 2m, the root mean square error (RMSE) and standard deviation (SD) of the measured temperature/strain by using DNN are improved to be 4.2°C/134.2με and 2.4°C/66.2με, respectively, which are much lower than the RMSE of 30.1°C/710.2με and SD of 19.4°C/529.1με for the conventional equation-solving method. Moreover, the temperature and strain extraction by DNN from 600,000 BGSs along 24km LEAF only requires 1.6s, which is much shorter than that of 5656.3s by the conventional equation-solving method. The enhanced accuracy and fast processing speed make the DNN approach a practical way of achieving simultaneous temperature and strain measurement based on the conventional BOTDA system without adding extra system complexity.

4.1 Motivation

Due to the remarkable capability of BOTDA for distributed temperature and strain measurement, it has found broad applications, especially in structural health monitoring (SHM) [1, 2]. In addition to the general goals of BOTDA to achieve long sensing distance, high spatial resolution, high measurement accuracy, and fast measurement speed [3-8], actual simultaneous temperature and strain measurement is also significant. It is difficult to realize in the conventional BOTDA due to the SBS's cross-sensitivity to temperature and strain. So far, some solutions have been proposed to achieve simultaneous temperature and strain measurement [9-22]. Hybrid sensor systems combining Brillouin scattering with Rayleigh scattering or Raman scattering have been reported to distinguish temperature and strain [9-11]. However, compared with a pure BOTDA system, hybrid systems are more complex and costly. One method for a single BOTDA system to distinguish the temperature and strain is to measure the BFS together with Brillouin peak power or bandwidth or birefringence in a polarization-maintaining fiber (PMF) [12-14]. However, introducing the particular fiber axis of PMF complicates the operation, and the power measurement is usually unstable. Another solution is to use multi-core fiber (MCF) [15], where several BFSs obtained from different fiber cores can simultaneously measure temperature and strain. In addition, using fibers with multi-peak BGS has been reported to be a potential solution, such as photonic crystal fiber (PCF) [16], large-effective-area fiber (LEAF) [17-19], dispersion compensating fiber (DCF) [20] and few-mode fiber (FMF) [21]. However, because of the slight difference in BFS-temperature/strain coefficients between Brillouin peaks, solving two BFS equations to calculate the temperature and strain produces significant errors. Hence, the obtained temperature and strain resolutions are much larger than a single temperature or strain measurement, e.g., 27°C/570με error in a 22km LEAF [18, 19]. Besides the poor accuracy, the curve fitting process to determine the BFS in the equation-solving method takes a long time, which makes the whole process of extracting temperature and strain time-consuming.

As mentioned in the previous chapter, machine learning techniques have been applied to the conventional BOTDA system to extract temperature with better performance instead of commonly used curve-fitting methods [22-25]. Among them, ANN has shown higher accuracy and a larger tolerance to measurement error compared to LCF and cross-correlation [22]. Besides, the support vector machine (SVM) has been demonstrated to have a processing speed of 100 times faster than LCF, with robustness to a wide range of experimental conditions [23, 24]. Compared with ANN, the DNN with autoencoder can be easily trained to achieve the global optimum for temperature extraction in BOTDA [25]. In order to explore further the practical value of DNN in BOTDA, we have recently reported for the first time the preliminary work on using DNN for simultaneous temperature and strain measurement [26], where a conventional BOTDA system adopting the single-mode LEAF is used with DNN to extract both the temperature and strain directly from the double-peak BGS of LEAF. Unlike the conventional equation-solving method [16-21], there is no curve fitting to obtain the BFS of Brillouin peaks and no subsequent procedure for solving two BFS equations. In contrast, the temperature and strain extraction process is regarded as a regression task for DNN, and the DNN learns the relationship between the double-peak BGS and the temperature and strain by training. Therefore, compared with the conventional equation-solving method, the DNN method can substantially improve the measurement accuracy of temperature and strain, and the whole process of temperature and strain extraction by DNN is expected to be very fast.

In this chapter, we demonstrate the enhanced accuracy and fast processing speed provided by the DNN method, and statistically analyze and compare its performance with the conventional equation-solving method through both simulation and experiment. The impact of noise added in the training of DNN is analyzed, and the optimal amount of noise needed to improve the DNN tolerance to the noise from experimental BGSs is investigated. With a specially designed experimental setup to make the strain uniform along the LEAF, we have tested a more extensive range of temperature and strain conditions in this work to verify the reliability of DNN-based simultaneous temperature and strain measurement. The results show that the measured temperature and strain by DNN have much lower measurement errors, including the RMSE and SD, which means the measured values are close to the real ones with minor fluctuations. Compared with the conventional equation-solving method, the DNN-based simultaneous temperature and strain measuring method improves the measurement accuracy by five times at least, and reduces the processing time by three orders of magnitude.

4.2 Principle and simulation

4.2.1 Principle of using DNN for simultaneous temperature and strain measurement

The structure of DNN is similar to ANN, except the training process includes both unsupervised and supervised learning for data size compression, which makes the training more efficient. Figure 4.1 illustrates a general structure of the DNN model containing an input layer, several hidden layers, and an output layer. The meaning and expression of symbols are similar to those illustrated in Fig. 3.1.

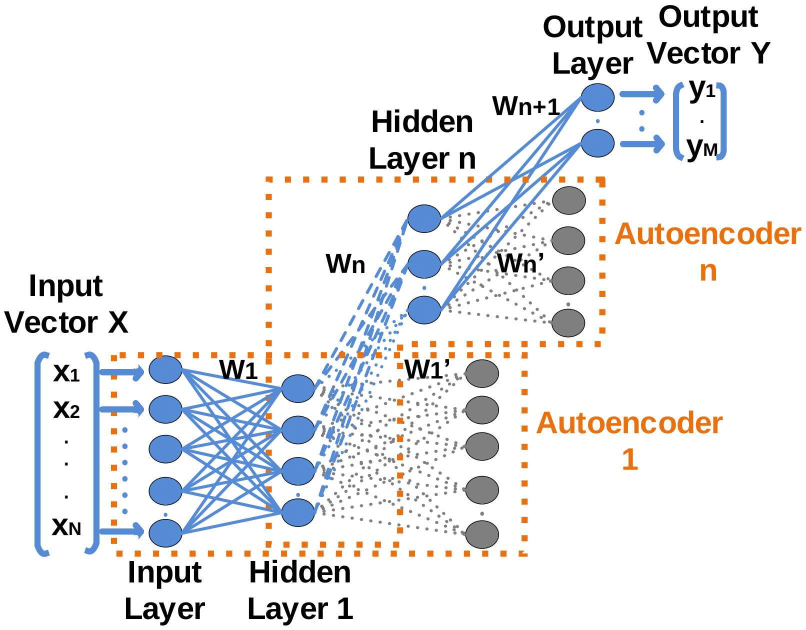

Fig. 4.1: General structure of DNN with n autoencoder hidden layers. W_n is the weight vector for the n^{th} hidden layer.

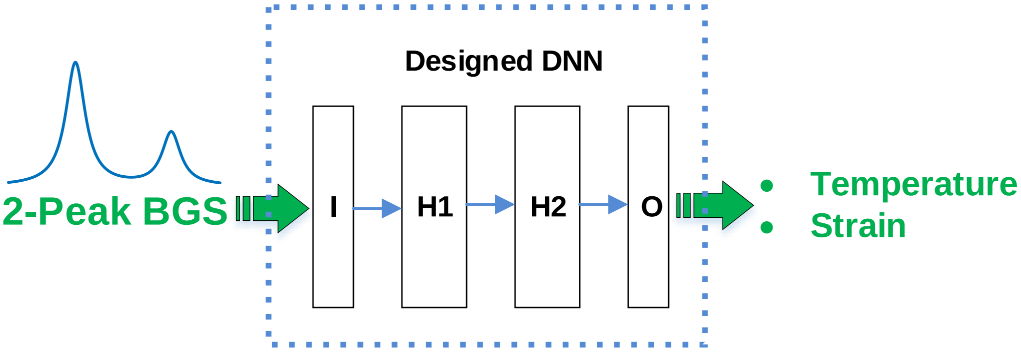

Fig. 4.2: Principle of using DNN for simultaneous temperature and strain measurement from double-peak BGS in LEAF. I: input layer; H1, H2: hidden layer; O: output layer.

Figure 4.2 shows the overall working principle. The DNN model contains one input layer (I), two hidden layers (H1 and H2), and one output layer (O). In this case, the input vector X (x_1, x_2, …, x_{226}) in Fig. 1, including 226 elements, represents the data vector for the double-peak BGS injected into the input layer of the DNN. The number of elements in X equals the number of scanned frequencies in the BOTDA system. The output vector Y (y_1, y_2) has two elements, corresponding to the temperature and strain. The utilization of DNN still contains two main stages: training and testing. Since the BFSs of the double-peak BGS in LEAF are linearly proportional to both the temperature and strain but have different responses, the DNN model can learn the relationship between the double-peak BGS and the temperature/strain after the appropriate training process. After training, the designed DNN can extract the values of temperature and strain directly from the inputted measured double-peak BGS, which is the so-called testing stage.

We use theoretical double-peak Lorentzian BGS expressed in Eq. (4.1) to train the DNN,

$$g(\upsilon)=\frac{g_B^{Peak1}}{1+[(\upsilon-\upsilon_B^{Peak1})/(\Delta\upsilon_B^{Peak1}/2)]^2}+\frac{g_B^{Peak2}}{1+[(\upsilon-\upsilon_B^{Peak2})/(\Delta\upsilon_B^{Peak2}/2)]^2}, \quad (4.1)$$

where $g(\upsilon)$ represents the normalized BGS, υ is the frequency difference between the probe and pump light in BOTDA, g_B^{Peak1} and g_B^{Peak2} are the peak gains, υ_B^{Peak1} and υ_B^{Peak2} are the BFSs, and $\Delta\upsilon_B^{Peak1}$ and $\Delta\upsilon_B^{Peak2}$ are the Brillouin gain bandwidths for Peak 1 and Peak 2, respectively. In our case, the range of υ is from 10.550GHz to 11.000GHz with a 2MHz interval, which is the same as the frequency scanning range during the acquisition of BGSs in the experiment. g_B^{Peak1} is set to be 1 and g_B^{Peak2} varies to traverse all the values from 0.13 to 0.53 with 0.10 intervals. This setting is consistent with the ratio between the 1st and 2nd Brillouin peak gains of our LEAF sensing fiber, which is pre-calibrated under different temperature and strain conditions used in the experiment. As a proof-of-concept demonstration, the temperature range in training is from 40ºC to 62ºC with a 2ºC interval, and the strain range is from 0με to 1860με with a 60με interval, both of which can be further enlarged although more time for DNN training will be consumed. Note that to make the results more generalized, the values of the temperature and strain in the testing stage will be random, including those that do not appear in the training stage, e.g., 61ºC and 1677.6με in our experiment. The two BFSs, i.e. υ_B^{Peak1} and υ_B^{Peak2} of the ideal double-peak BGS are determined using pre-calibrated BFS-temperature/strain coefficients of our LEAF sensing fiber. In order to accommodate BGS linewidth variations along the fiber [22], the range of $\Delta\upsilon_B^{Peak1}$ is from 46MHz to 66MHz with a 2MHz interval and $\Delta\upsilon_B^{Peak2}$ is from 40MHz to 80MHz with a 4MHz interval. Hence, 11 pairs of $\Delta\upsilon_B^{Peak1}$ and $\Delta\upsilon_B^{Peak2}$ values are formed for training. The above parameter setting to obtain the ideal BGSs for training is based on the pre-calibrated double-peak BGS of our LEAF sensing fiber and depends on the optimization process of the DNN model through repeated trials for optimal performance. After training, the DNN model can directly extract the temperature and strain values from the input BGS data. Since no procedure for solving two BFS equations is needed, the large error induced by a small matrix determinant can be avoided, and the accuracy will improve. As there is no time-consuming curve fitting process to obtain the BFSs of the Brillouin peaks, the whole process of both temperature and strain extraction by DNN will be speedy. In the next section, we also describe the conventional equation-solving method for comparison.

4.2.2 Conventional equation-solving method for simultaneous temperature and strain measurement

It is known that the BFSs of Peak 1 and Peak 2 in LEAF sensing fiber have linear relationships with both temperature and strain, which are shown as Eqs. (4.2) and (4.3) [16-18, 20],

$$\Delta BFS^{Peak1} = C_T^{Peak1} \cdot \Delta T + C_\varepsilon^{Peak1} \cdot \Delta\varepsilon \tag{4.2}$$

$$\Delta BFS^{Peak2} = C_T^{Peak2} \cdot \Delta T + C_\varepsilon^{Peak2} \cdot \Delta\varepsilon \tag{4.3}$$

where ΔBFS^{Peak1} and ΔBFS^{Peak2} are the BFS change of Peak 1 and Peak 2 under the temperature and strain change of ΔT and $\Delta\varepsilon$, respectively. C_T^{Peak1} and C_ε^{Peak1} are the BFS-temperature/strain coefficients for Peak 1, while C_T^{Peak2} and C_ε^{Peak2} are the coefficients for Peak 2, respectively. In the conventional equation-solving method [16-21], ΔBFS^{Peak1} and ΔBFS^{Peak2} are obtained by LCF based on Eq. (4.1), and then the temperature and strain are obtained by solving Eqs. (4.2) and (4.3) as follows [16-18, 20],

$$\Delta T = \frac{C_\varepsilon^{Peak2} \cdot \Delta BFS^{Peak1} - C_\varepsilon^{Peak1} \cdot \Delta BFS^{Peak2}}{C_T^{Peak1} \cdot C_\varepsilon^{Peak2} - C_T^{Peak2} \cdot C_\varepsilon^{Peak1}}, \tag{4.4}$$

$$\Delta\varepsilon = \frac{C_T^{Peak2} \cdot \Delta BFS^{Peak1} - C_T^{Peak1} \cdot \Delta BFS^{Peak2}}{C_T^{Peak2} \cdot C_\varepsilon^{Peak1} - C_T^{Peak1} \cdot C_\varepsilon^{Peak2}}. \tag{4.5}$$

This is generally the procedure of the equation-solving method to simultaneously measure the temperature and strain based on two BFSs of multi-peak BGS. However, as mentioned in [18, 19], since the matrix determinant $C_T^{Peak1} \cdot C_\varepsilon^{Peak2} - C_T^{Peak2} \cdot C_\varepsilon^{Peak1}$ is usually very small, a larger error will be produced when solving Eqs. (4.4) and (4.5) to obtain the temperature and strain, compared with the case of single temperature or strain measurement. Thus, except for the time-consuming curve fitting procedure, the equation-solving method imposes a stringent requirement on the resolution of BFS measurement, and it is difficult to obtain the temperature and strain with high accuracy, especially when the FUT is long (e.g., several tens of kilometers) and the BFS resolution becomes worse.

4.2.3 Simulation results

Based on the parameter setting in Section 4.2.1, there are 12 temperature conditions, 32 strain conditions, 11 BGS linewidth conditions, and 5 peak gain conditions of Peak 2. Thus, we have 12×32×11×5=21120 ideal double-peak Lorentzian BGSs and 12×32=384 target temperature and strain values in total for the DNN training. The DNN is trained using the error back-propagation (BP) algorithm. After repeated trials with a different number of hidden layers and neurons for optimal performance, the DNN model is eventually designed to have two hidden layers with 40 and 8 neurons, respectively. Two hidden layers are found to be enough for acceptable results, while more hidden layers will take a much longer time for training but without noticeable performance improvement. The following simulation and experiment results are all obtained using this DNN structure (226-40-8-2).

In this section, we first conduct a simulation using simulated double-peak BGSs in the testing stage to evaluate the performance of DNN for simultaneous temperature and strain measurement. In the simulation, noisy BGSs are simulated by adding Gaussian white noise to the profile based on Eq. (4.1), and the signal-to-noise ratio (SNR) of the simulated BGSs is controlled by the amount of noise added. Note that the SNR of the simulated BGS is calculated by using the ratio between the amplitude of the BGS peak and the standard deviation of its spectral points [27]. To improve the noise tolerance of the DNN model, we train the DNN by using combined clean and noisy BGSs. The number of clean BGSs for training is 21120. The noisy BGSs with an SNR of 10.5dB for training are obtained by adding Gaussian white noise to the clean ones. Thus, the total number of BGSs used for training is 42240. 10.5dB SNR is chosen since it just covers the lowest SNR level in our experiment, and the DNN trained with noisy BGSs of 10.5dB SNR is found to be enough to achieve the optimal performance for temperature and strain extraction in the experiment. After training, the DNN model is applied to extract both the temperature and strain from 1000 simulated testing BGSs of 20dB SNR, i.e., the case for low noise level. We have randomly selected five groups of target temperature and strain for the demonstration (40^{o}C/50με; 45^{o}C/200με; 52^{o}C/1400με; 55^{o}C/1600με; 60^{o}C/1800με). As an example, we show the results for

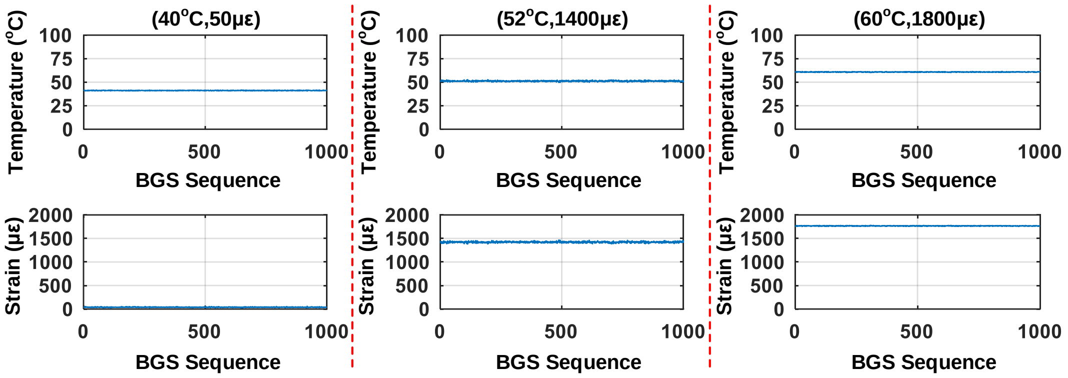

Fig. 4.3: Temperature and strain distribution extracted by DNN from 1000 simulated testing BGSs of 20dB SNR.

three groups of target temperature and strain in Fig. 4.3, which plots the extracted temperature and strain distribution by DNN. Fluctuations of the extracted temperature and strain are small, and the extracted values are close to the target ones for all three cases. The detailed error performance of DNN is analyzed by calculating the SD and RMSE of the extracted temperature and strain, which is given in Table 4.1 for all five groups of target temperature and strain conditions. SD means the uncertainty or fluctuation of the extracted values. And RMSE indicates how close the extracted temperature and strain values are to the target ones, which is calculated by comparing the target values and extracted ones by DNN. The maximum SD and RMSE of the extracted temperature are only 0.5°C and 1.2°C, respectively; while those of the extracted strain are 13.5με and 43.7με, respectively. The results show that the DNN

Table 4.1: Corresponding error performance of DNN for results in Fig. 4.3

Temperature (ºC)	***Strain (με)***	***Temperature (ºC)***		***Strain (με)***	
		SD	***RMSE***	***SD***	***RMSE***
40.0	50.0	0.2	1.2	4.9	11.7
45.0	200.0	0.4	1.1	9.2	43.7
52.0	1400.0	0.5	0.9	13.5	25.9
55.0	1600.0	0.3	0.8	8.9	14.3
60.0	1800.0	0.2	0.8	4.5	33.8

model trained using combined clean and noisy BGSs performs well when extracting the temperature and strain from noisy testing BGSs with low noise levels.

Next, we further increase the noise level in the testing BGSs, and investigate the DNN performance. The DNN model is the same as that used in Fig. 4.3. Figure 4.4 shows the extracted temperature and strain distribution from 1000 simulated testing BGSs of 10.58dB SNR, which is the lowest SNR level observed in our experiment. Due to more considerable noise in the testing BGSs, the extracted temperature and strain fluctuations become slightly larger than those in Fig. 4.3, but the extracted values are still close to the target ones. For comparison, we also use the conventional equation-solving method described in Section 4.2.2 to extract the temperature and strain from the same testing BGSs, and Fig. 4.5 gives the results. Note that we adopt the Levenberg-Marquardt algorithm (LMA) for LCF to extract BFS [23], where it starts with an initial guess for the gain parameter, central frequency parameter, and linewidth parameter, and then all of them are iteratively updated until the squared error converges. Besides large fluctuations, the extracted temperature and strain in Fig. 4.5 are far away from the target ones, and some extracted values are even out of the scales in Fig. 4.5, showing poor accuracy of the equation-solving method when the noise is relatively high. As mentioned in Section 4.2.2, the low accuracy originates from the slight difference in BFS coefficients between the two peaks, leading to significant error when solving the two BFS Eqs. (4.2) and (4.3). The detailed error performance for the results in Fig. 4.4 and Fig. 4.5 are compared in Table 4.2, which also includes the results for the other two groups of target temperature and strain. Take the target temperature and strain of (52.0^{o}C, 1400.0με) as an example. The RMSE of the extracted temperature/strain by using DNN are 3.4^{o}C/95.4με, while those by using the equations solving method are found to be 27.4^{o}C/746.2με, respectively, which indicates that the errors of extracted temperature and strain by the equation-solving method are about 8 times larger than those obtained by DNN. In all the five groups of target temperature and strain, the maximum SD of the extracted temperature/strain by DNN is 3.3^{o}C/93.5με, and the maximum RMSE is 3.4^{o}C/95.4με, respectively. While for the equation-solving method,

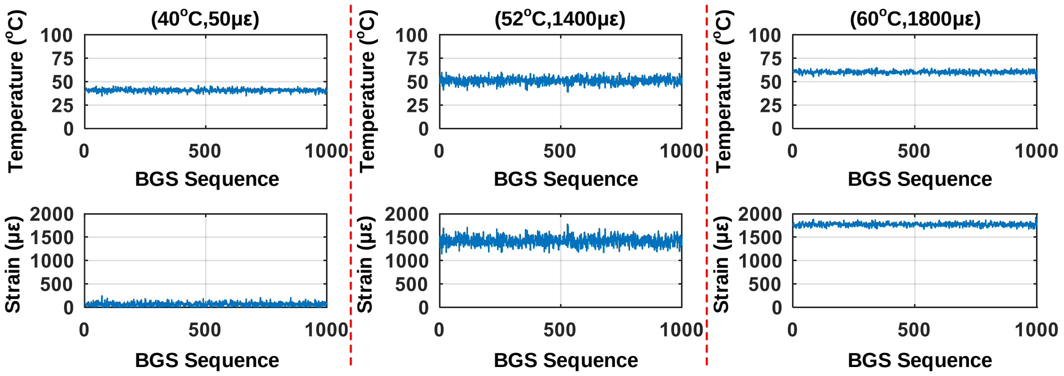

Fig. 4.4: Temperature and strain distribution extracted by DNN from 1000 simulated testing BGSs of 10.58dB SNR.

the maximum SD is 31.2°C/849.8με, and the maximum RMSE is 31.2°C/852.0με, respectively. Although the error performance of DNN degrades a little due to more extensive noise in input testing BGSs, it still has significant improvement compared to the equation-solving method.

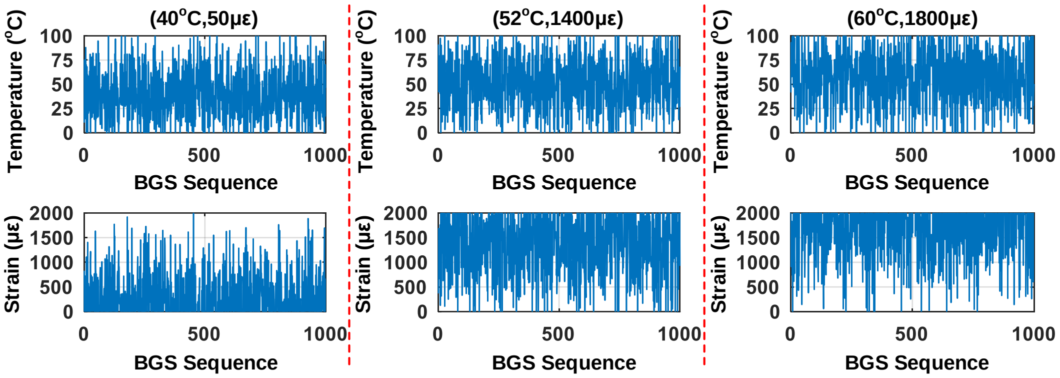

Fig. 4.5: Temperature and strain distribution extracted by the equations solving method from 1000 simulated testing BGSs of 10.58dB SNR.

Table 4.2: Corresponding error performance of DNN and the equations solving method for results in Figs. 4.4 and 4.5

Temperature (°C)	*Strain (με)*	*Temperature (°C)*				*Strain (με)*			
		DNN		*Equations solving method*		*DNN*		*Equations solving method*	
		SD	*RMSE*	*SD*	*RMSE*	*SD*	*RMSE*	*SD*	*RMSE*
40.0	**50.0**	1.7	1.9	26.2	26.2	42.3	45.3	714.7	714.7
45.0	**200.0**	2.4	2.8	25.5	25.5	63.2	74.0	693.9	694.0
52.0	**1400.0**	3.3	3.4	27.4	27.4	93.5	95.4	745.9	746.2
55.0	**1600.0**	2.4	2.6	26.9	26.9	66.1	68.6	733.5	733.8
60.0	**1800.0**	1.6	1.7	31.2	31.2	35.7	46.6	849.8	852.0

4.3 Experiment and results

In this section, experimental BGSs under different actual temperature and strain values are collected using the BOTDA setup shown in Fig. 4.6. The same DNN model as used in Fig. 4.3 and Fig. 4.4 is applied to extract both the temperature and strain distribution from experimental BGSs along the sensing fiber. The BOTDA setup is similar to that used in Chapter 3. The main difference is that a new specially designed device is used to apply uniform strain changes on the FUT under different temperatures. The peak power of the pump pulse is 20dBm, and the probe power is -8dBm, respectively. The FUT is a 24km long LEAF (Corning LEAF Optical Fiber ITU-T G.655.C), with its last 7m section heated (i.e., FUT inside the oven in Fig. 4.6) and the remaining section kept under room temperature and zero strain (i.e., FUT outside the oven in Fig. 4.6). And the 7m long FUT inside the oven is coiled on two micro-positioners, with one fixed and the other movable for applying different levels of uniform strain. Thus, different temperature and strain conditions are applied to the 7m long FUT inside the oven. In

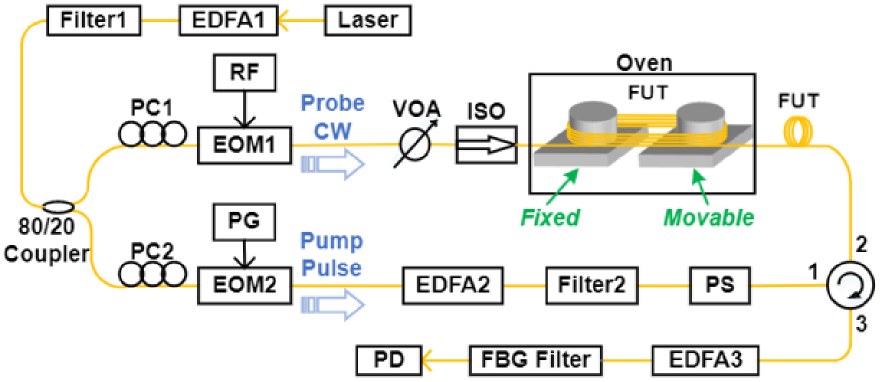

Fig. 4.6: BOTDA system setup.

order to have sufficient data points collected along the last 7m long FUT for the purpose of statistical analysis of the error performance, a relatively high sampling rate of 2.5GSample/s is adopted.

Figure 4.7(a) shows the measured BGS distribution along LEAF sensing fiber, and Fig. 4.7(b) gives the measured double-peak BGS at one location of the last 7m section when the temperature is 23.5°C and the strain is 0με. The BFS-temperature and BFS-strain relations for BGS Peak 1 and Peak 2 are shown in Fig. 4.7(c) and 4.7(d), respectively. The BFS-temperature coefficients of Peak 1 and Peak 2 are measured to be 1.0546MHz/°C and 0.9380MHz/°C, respectively. At the same time, BFS-strain coefficients of the two peaks are measured to be 0.0385MHz/με and 0.0384MHz/με,

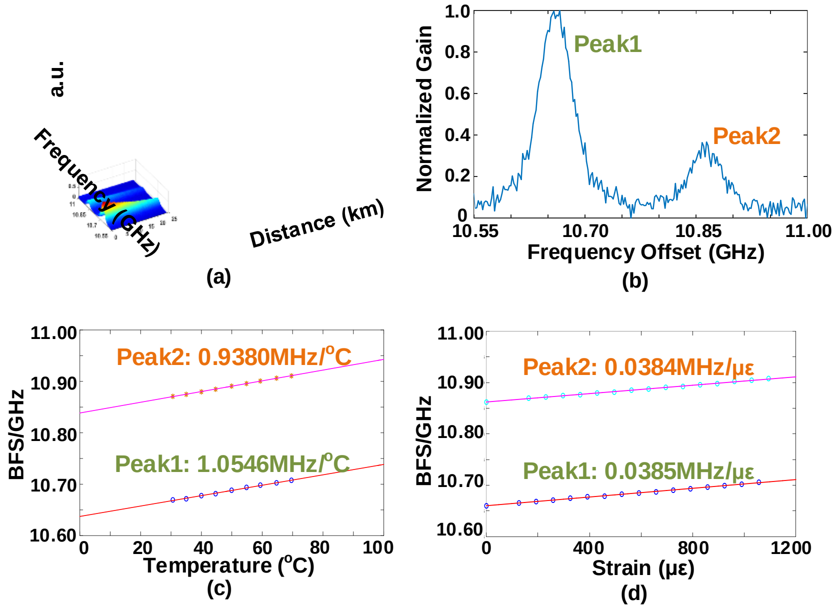

Fig. 4.7: (a) Measured BGS distribution along LEAF sensing fiber; (b) measured double-peak BGS of LEAF under room temperature of 23.5°C and strain of 0με; (c) measured BFS-temperature relations for Peak 1 and Peak 2; (d) measured BFS-strain relations for Peak 1 and Peak 2.

respectively. As mentioned in Section 4.2.1, the coefficients and relations of BFS with temperature and strain are used to obtain ideal BGSs based on Eq. (4.1) for DNN training.

In the experiment, we apply different values of temperature and strain to the last 7m FUT and collect the corresponding experimental BGSs, which serve as the input testing BGSs to the DNN model for temperature and strain measurement. Eight groups of actual temperature and strain conditions are randomly selected for the demonstration, which includes values that do not appear in the training stage, e.g. (61°C, 1861.7με). As an example, we show the results for four groups of actual temperature and strain conditions in Fig. 4.8. The blue curves in Fig. 4.8 show the temperature and strain distribution along the central part (4.7m section with relatively constant strain) of the last 7m FUT extracted by using DNN. For comparison, the equation-solving method results are also given, shown as the orange curves in Fig. 4.8. It is obvious that the fluctuations of measured temperature and strain using DNN are small, indicating small uncertainty of the measured temperature and strain. In contrast, the equation-solving method fluctuations are much more significant. In addition, the measured values by using DNN are close to the actual temperature and strain values, while those by using the equation-solving method considerably deviate from the actual values, e.g., the group of (56.0^{o}C, 1660.8με) in Fig. 4.8. This means that the equations solving method has worse error performance, which agrees well with that in [18].

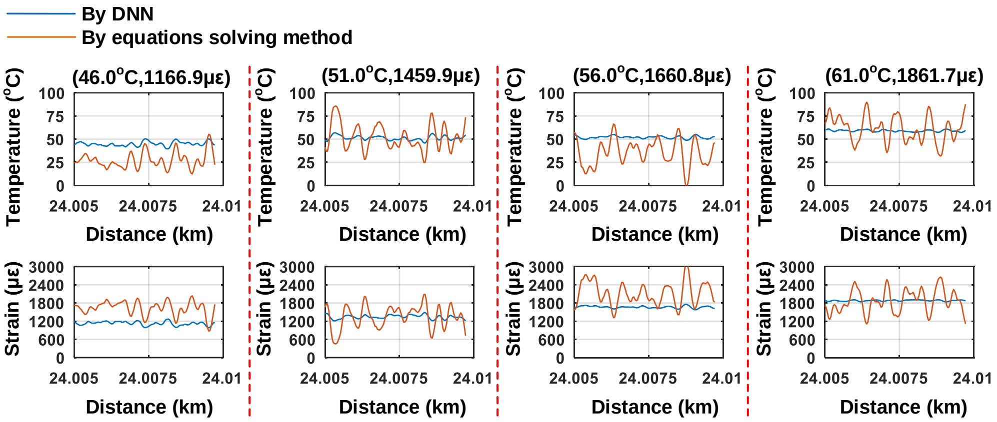

Fig. 4.8: Temperature and strain distribution along the central part of the last 7m FUT extracted by DNN (blue curve) and the equations solving method (orange curve), respectively.

Table 4.3: Corresponding error performance of DNN and the equations solving method for results in Fig. 4.8

Temperature (ºC)	*Strain (με)*	*Temperature (ºC)*				*Strain (με)*			
		DNN		*Equations solving method*		*DNN*		*Equations solving method*	
		SD	*RMSE*	*SD*	*RMSE*	*SD*	*RMSE*	*SD*	*RMSE*
46.0	**1166.9**	2.4	2.6	8.8	20.6	63.7	76.1	237.1	517.3
46.0	**1351.0**	2.4	2.4	11.9	24.4	66.2	96.5	320.9	616.2
51.0	**1459.9**	2.3	2.3	13.9	13.9	63.3	134.2	378.0	394.3
51.0	**1551.9**	2.0	3.4	11.8	15.1	59.5	90.2	322.9	356.9
56.0	**1660.8**	1.4	4.2	14.3	24.9	36.0	36.0	385.9	603.4
56.0	**1752.9**	1.3	3.1	14.3	30.1	26.8	65.7	383.2	710.2
61.0	**1677.6**	1.3	4.2	19.4	19.6	35.6	38.9	529.1	527.1
61.0	**1861.7**	1.0	2.3	14.1	14.1	18.8	26.2	383.2	381.6

A detailed comparison between the error performance using DNN and that using the equation-solving method has been given in Table 4.3 for all eight groups of actual temperature and strain conditions. Similar to the simulation, we also evaluate the error performance of the experimental results, including the SD and RMSE. The SD indicates the fluctuation of the measured temperature and strain, while the RMSE reflects how close the measured values are to the real ones. The actual temperature values are read from a reference thermometer, and the actual strain values are obtained from the reading of the micro-positioner during the experiment. Since the strain along the central 4.7m section of the last 7m FUT is relatively uniform, the SD and RMSE are calculated using the data points along this section (117 data points in total under a sampling rate of 2.5GSample/s). From Table 4.3, we can see that in each group of temperature and strain, both the RMSE and SD using DNN are much lower than those using the equation-solving method. Taking the group of (51.0°C, 1551.9.0με) as an example, the RMSE and SD of the measured temperature/strain by DNN are 3.4°C/90.2με and 2.0°C/59.5με, respectively; while the RMSE and SD by the equations solving method are found to be 15.1°C/356.9με and 11.8°C/322.9με, respectively. The measured temperature and strain errors by the equation-solving method are more than four times larger than those by DNN. For DNN, the worst RMSE of the measured temperature/strain in Table 3 is 4.2°C/134.2με, and the worst SD is 2.4°C/66.2με, respectively. While for the equation-solving method, the worst RMSE is 30.1°C/710.2με, and the worst SD is 19.4°C/529.1με, respectively. As shown in Fig. 4.8, much lower RMSE by DNN represents that the measured temperature and strain values are closer to the actual values, and lower SD by DNN implies that the fluctuations of the measured values are much more minor. Thus, DNN for simultaneous temperature and strain measurement has significantly improved the accuracy compared with the equation-solving method. Moreover, since there are 600,000 BGSs along 24km LEAF at a 2.5GSample/s sampling rate, the equation-solving method with a time-consuming LCF process takes 5656.3s to extract both the temperature and strain distribution from such a large number of sensing points (computer platform: i7-6700K CPU and 16G RAM). While the DNN only consumes 1.6s for the same purpose, showing breakneck processing speed for simultaneous temperature and strain measurement.

Besides the above situations with constant temperature and strain along the FUT inside the oven, we also implement the experiment with abrupt environment changes along the FUT. The experiment setup is the same as that in Fig. 4.6, except the FUT inside the oven now has a length of 45m and is divided into three sections (i.e., Section 1 of 19m, Section 2 of 7m, Section 3 of 19m), with the strain only applied to the middle Section 2. For example, for the demonstration, we set the oven's temperature to 46.0oC and the applied strain to 1166.9με. We compare the performance of the same DNN model and the equation-solving method used before, shown in Fig. 4.9 and Table 4.4. Similarly, we can see that the fluctuations of measured temperature and strain using DNN are small, while those using the equation-solving method are much larger. Moreover, both the RMSE and SD using DNN are much lower than those using the equation-solving method, as given in Table 4.4 for each section of FUT, implying better error performance of DNN when compared with the equation-solving method.

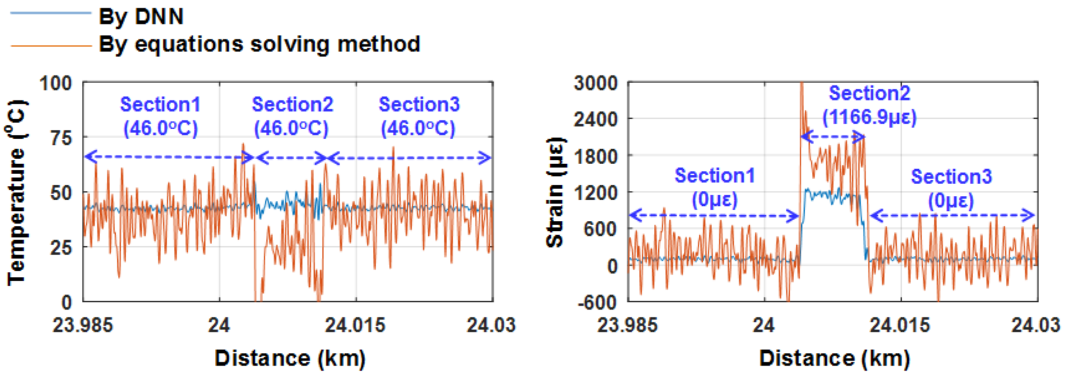

Fig. 4.9: Temperature and strain distribution along the FUT inside the oven extracted by DNN (blue curve) and the equations solving method (orange curve), respectively.

Table 4.4: Corresponding error performance of DNN and the equations solving method for results in Fig. 4.9

Fiber section	***Temperature (°C)***				***Strain (με)***			
	DNN		***Equations solving method***		***DNN***		***Equations solving method***	
	SD	***RMSE***	***SD***	***RMSE***	***SD***	***RMSE***	***SD***	***RMSE***
1	0.9	3.5	10.8	12.6	23.6	97.0	292.0	339.5
2	2.4	2.6	8.7	20.6	63.7	76.1	237.1	517.3
3	0.9	3.4	10.0	11.5	22.4	99.8	272.3	315.7

In our experiment, the total length of the FUT is 24km, and our spatial resolution is 2m. The worst uncertainty of measured temperature and strain by the equation-solving method is 19.4°C/529.1με, and they are improved to be 2.4°C/66.2με by using DNN. Note that Ref. [18] reports temperature and strain errors of 27°C/570με by the equation-solving method for 22km LEAF length. Other works by the equation-solving method demonstrate better error performance but within much shorter sensing distances, e.g., 3.9°C/83με in 2m PCF with a spatial resolution of 15cm [16], 5°C/60με in 3.7km LEAF with a spatial resolution of 2m [17], 1.8°C/37με in 377m LEAF with a spatial resolution of 4m [19], 2.6°C/64.6με in 1km DCF with a spatial resolution of 2m [20], and 1.2°C/21.9με in 3km few-mode fiber with a spatial resolution of 2.5m [21]. Furthermore, in [28], ANN has been used to classify the effect of temperature and strain in a standard single-mode fiber (SSMF), without the capability of measuring exact temperature/strain values and the analysis of measured temperature/strain errors. Therefore, compared to the results in literature with similar sensing distance, our DNN approach shows much better accuracy than the equation-solving method.

It is worth mentioning that in this work, DNN extracts both the temperature and strain mainly from the two BFSs of double-peak BGS in LEAF, but it can also be applied to replace all the equations solving methods where any two of the parameters (e.g., BFS, Brillouin peak power, bandwidth, birefringence, etc.) are measured to build up the equations [12-21]. The significant error induced by the minor matrix determinant during the equation-solving can be avoided, and the accuracy improves as a result. Moreover, multiple measured parameters can be potentially combined as the input to the DNN model to improve the accuracy of simultaneous temperature and strain measurement further.

4.4 Summary

The simultaneous temperature and strain measurement has been achieved using the DNN-based method in BOTDA along 24km LEAF with 2m spatial resolution. DNN is trained by using combined ideal clean and noisy BGSs, and then the temperature and strain are extracted directly from the measured double-peak BGS with high accuracy. Both simulation and experiment under different temperature and strain conditions have been conducted to evaluate this DNN-based method, compared with the conventional equation-solving method in measurement accuracy and processing time. The DNN scheme avoids the significant error induced by the minor matrix determinant of solving two BFS equations. Thus, it significantly improves measurement accuracy. The worst temperature/strain RMSE using DNN is 4.2°C/134.2με, which is much smaller than that of 30.1°C/710.2με from the equation-solving method. Moreover, the worst temperature/strain uncertainty using DNN is 2.4°C/66.2με, which is much lower than that of 19.4°C/529.1με from the equation-solving method, respectively. In addition, without the curve fitting process, the temperature and strain extraction process using DNN is speedy. DNN needs only 1.6s to extract both the temperature and strain from 600,000 BGSs along 24km LEAF, which is much shorter than that of 5656.3s by the conventional equation-solving method. We believe that the enhanced accuracy and fast processing speed promote the practicability of using DNN to achieve simultaneous temperature and stain measurement in a single BOTDA system.

References

[1] A. Barrias, J. R. Casas, and S. Villalba, “A review of distributed optical fiber sensors for civil engineering applications,” Sensors, 16(5): 748 (2016).

[2] C. Hong, Y. Zhang, G. Li, M. Zhang, and Z. Liu, “Recent progress of using

Brillouin distributed fiber sensors for geotechnical health monitoring," Sensors and Actuators A: Physical, 258: 131-145 (2017).

[3] M. Soto, X. Angulo-Vinuesa, S. Martin-Lopez, S. Chin, J. Ania-Castanon, P. Corredera, E. Rochat, M. Gonzalez-Herraez, and L. Thevenaz, "Extending the real remoteness of long-range Brillouin optical time-domain fiber analyzers," J. Lightwave Technol., 32(1), 152-162 (2014).

[4] S. Diakaridia, Y. Pan, P. Xu, D. Zhou, B. Wang, L.Teng, Z. Lu, D. Ba, and Y. Dong, "Detecting cm-scale hot spot over 24-km-long single-mode fiber by using differential pulse pair BOTDA based on double-peak spectrum," Opt. Express 25(15), 17727–17736 (2017).

[5] X. Jia, H. Chang, K. Lin, C. Xu, and J. Wu, "Frequency-comb-based BOTDA sensors for high-spatial-resolution/long-distance sensing," Opt. Express 25(6), 6997-7007 (2017).

[6] M. A. Soto and L. Thévenaz, "Modeling and evaluating the performance of Brillouin distributed optical fiber sensors," Opt. Express 21(25), 31347-31366 (2013).

[7] D. Zhou, Y. Dong, B. Wang, T. Jiang, D. Ba, P. Xu, H. Zhang, Z. Lu, and H. Li, "Slope-assisted BOTDA based on vector SBS and frequency-agile technique for wide-strain-range dynamic measurements," Opt. Express, 25(3), 1889-1902 (2017).

[8] X. Bao and L. Chen, "Recent progress in Brillouin scattering based fiber sensors," Sensors, 11(12), 4152-4187 (2011).

[9] K. Kishida, Y. Yamauchi, and A. Guzik, "Study of Optical Fibers Strain-Temperature Sensitivities Using Hybrid Brillouin-Rayleigh System," Photonics Sensors, 4(1), 1-11 (2014).

[10] M. N. Alahbabi, Y. T. Cho, and T. P. Newson, "Simultaneous temperature and strain measurement with combined spontaneous Raman and Brillouin scattering," Opt. Lett.

30(11), 1276-1278 (2005).

[11] Z. Zhao, Y. Dang, M. Tang, L. Duan, M. Wang, H. Wu, S. Fu, W. Tong, P. P. Shum, and D. Liu, "Spatial-division multiplexed hybrid Raman and Brillouin optical time-domain reflectometry based on multi-core fiber," Opt. Express 24(22), 25111-25118 (2016).

[12] X. Bao, Q. Yu, and L. Chen, “Simultaneous strain and temperature measurements with polarization-matiaining fibers and their error analysis using distributed Brillouin loss system,” Opt. Lett. 29(12), 1341-1344 (2004).

[13] W. Zou, Z. He, and K. Hotate, “Complete discrimination of strain and temperature using Brillouin frequency shift and birefringence in a polarization-maintaining fiber,” Opt. Express, 17(3), 1248-1255 (2009).

[14] Y. Dong, L. Chen, and X. Bao, “High-spatial-resolution simultaneous strain and temperature sensor using Brillouin scattering and birefringence in a polarization-maintaining fibre,” IEEE Photon. Technol. Lett., 22 (18), 1364-1366 (2010).

[15] Z. Zhao, Y. Dang, M. Tang, B. Li, L. Gan, S. Fu, H. Wei, W. Tong, P. Shum, and D. Liu, "Spatial-division multiplexed Brillouin distributed sensing based on a heterogeneous multicore fiber," Opt. Lett. 42(1), 171-174 (2017).

[16] L. Zou, X. Bao, S. Afshar, and L. Chen, “Dependence of the Brillouin frequency shift on strain and temperature in a photonic crystal fiber,” Opt. Express, 29(13), 1485-1487 (2004).

[17] C. C. Lee, P. W. Chiang, and S. Chi, “Utilization of a dispersion-shifted fiber for simultaneous measurement of distributed strain and temperature through Brillouin frequency shift,” IEEE Photonics Technology Letters, 13(10), 1094-1096 (2001).

[18] M. Alahbabi, Y. T. Cho, and T. P. Newson, “Comparison of the methods for discriminating temperature and strain in spontaneous Brillouin-based distributed

sensors," Opt. Lett., 29(1), 26-28 (2004).

[19] X. Liu and X. Bao, "Brillouin spectrum in LEAF and simultaneous temperature and strain measurement," J. Lightwave Technol., 30(8), 1053-1059 (2012).

[20] Z. Li, L. Yan, X. Zhang, and W. Pan, "Temperature and Strain Discrimination in BOTDA Fiber Sensor by Utilizing Dispersion Compensating Fiber," IEEE Sensors Journal, 18(17), 7100-7105 (2018).

[21] A. Li, Y. Wang, J. Fang, M. Li, B. Y. Kim, and W. Shieh, "Few-mode fiber multi-parameter sensor with distributed temperature and strain discrimination," Opt. Lett., 40(7), 1488–1491 (2015).

[22] A. Azad, L. Wang, N. Guo, H. Tam, and C. Lu, "Signal processing using artificial neural network for BOTDA sensor system," Opt. Express, 24(6), 6769-6782 (2016).

[23] H. Wu, L. Wang, N. Guo, C. Shu, and C. Lu, "Brillouin optical time domain analyzer assisted by support vector machine for ultrafast temperature extraction," J. Lightwave Technol., 35(19), 4159-4167 (2017).

[24] H. Wu, L. Wang, N. Guo, C. Shu, and C. Lu, "Support vector machine assisted BOTDA utilizing combined Brillouin gain and phase information for enhanced sensing accuracy," Opt. Express, 25(25), 16534-16549 (2017).

[25] B. Wang, N. Guo, F. N. Khan, A. K. Azad, L. Wang, C. Yu, and C. Lu, "Extraction of Temperature Distribution Using Deep Neural Networks for BOTDA Sensing System," in 2017 Conference on Lasers and Electro-Optics Pacific Rim (CLEO-PR), paper s2027.

[26] B. Wang, L. Wang, C. Yu, and C. Lu, "Simultaneous temperature and strain measurement using deep neural networks for BOTDA sensing system," in The Optical Fiber Communication Conference and Exhibition 2018 (OFC), paper Th2A.66, pp. 1-3.

[27] A. Lopez-Gil, M. A. Soto M A and X. Angulo-Vinuesa, A. Dominguez-Lopez, S.

Martin-Lopez, L. Thévenaz, and M. Gonzalez-Herraez, “Evaluation of the accuracy of BOTDA systems based on the phase spectral response,” Opt. Express, 24(15): 17200-17214 (2016).

[28] R. Ruiz-Lombera, A. Fuentes, L. Rodriguez-Cobo, J. M. Lopez-Higuera, and J. Mirapeix, “Simultaneous temperature and strain discrimination in a conventional BOTDA via artificial neural networks”, J. Lightwave Technol., 36(11), 2114-2121 (2018).

5 Robust and Fast Temperature Extraction for BOTDA Using Denoising Autoencoder based DNN

In this chapter, a method of robust and fast temperature extraction for BOTDA uwsing the denoising autoencoder (DAE) based DNN is proposed and investigated. It is explored and improved based on the method used in previous work in Chapter 3 and Chapter 4. After sufficient training, the DAE can suppress the noise in the measured BGS, and improves the signal-to-noise ratio (SNR) by 9.96dB in our experiment. The DAE is stacked as the basic block for the temperature extraction task to construct the DNN model. Since the DNN model is based on DAE, it possesses both the advantages of DAE and the advantages of DNN itself mentioned in previous work. It means that denoising and fast temperature extraction can be achieved simultaneously using only a single DNN model. As a result, this method is more robust and faster than the conventional LCF method, especially when the SNR of input data is very low. In the case of 4.6dB SNR, the SD of the measured temperature at the end of 40km FUT decreases from 2.4°C to 1.2°C using DAE-based DNN compared with LCF, and the corresponding RMSE decreases from 2.4°C to 1.3°C. In addition, the DAE-based DNN method promotes the temperature extraction speed by 500 times faster than that of LCF. The combination of denoising and fast processing advantages makes the DAE-based DNN more practical for temperature extraction in BOTDA.

5.1 Motivation

During the development and application process of BOTDA over the past three decades [1-6], the SNR is one of the critical parameters which limits the performance in respect of available sensing range, spatial resolution, and measurement accuracy in BOTDA systems [7]. Typically, higher SNR requires higher probe light power or pump light power injected. However, the highest light power is limited by the non-local effects [8] and nonlinear effects [9,10]. Recently, some new signal processing methods have been introduced to improve the BOTDA system performance limited by the SNR of collected data. Among them, some image denoising techniques, including non-local means (NLM), wavelet denoising (WD), and block-matching and 3D filtering (BM3D), have been used in BOTDA and have shown the effects of improving the SNR of collected data [11,12]. Besides, a machine learning method called denoising convolutional neural networks (DnCNNs) has also been used for data denoising in BOTDA [13]. However, after the data denoising using these methods, one additional procedure involving the conventional curve fitting methods, such as the LCF, is still needed to obtain the needed temperature/strain information, which makes the whole data processing even more time-consuming.

On the other side, some ML methods, including the ANN, the support-vector machine (SVM), and the DNN, have also been utilized in BOTDA for direct temperature/strain extraction, with obvious advantages over conventional curve fitting methods [14-16]. Based on our preliminary work about using the DAE for noise suppression of collected BGS data and DAE-based DNN for direct temperature extraction in BOTDA recently

[16], in this Chapter, we investigate further the denoising effect of DAE and compare the detailed temperature extraction performance of the DAE-based DNN and the conventional LCF. Since the DAEs rather than ordinary autoencoders are used to compose the DNN model, the DNN can not only suppress the noise but also quickly extract the temperature directly from the BGS data in one single step. Utilization of the DAE-based DNN for temperature extraction combines the advantages of both the image denoising and ML methods.

5.2 Principle of DAE-based DNN for temperature extraction in BOTDA

Similar to the ordinary autoencoder, the typical structure of DAE contains one input layer, one interlayer, and one output layer [17-19], as shown in Fig. 5.1. In this structure, all W and W' represent the weight vectors while $X(x_1, x_2, ..., x_N)$ is the input vector and $X'(x_1', x_2', ..., x_N')$ represents the target or output vector. The numbers of neurons in the input and output layers are the same, corresponding to the actual application's data dimensions. Moreover, the interlayer neuron numbers are set and adjusted after optimization. They are generally less than the neuron numbers in the input and output layers, since the DAE interlayer extract features and compress the dimension of input data. For the DAE training, the simulated corrupted data (or noisy data) and corresponding clean data are provided in pairs as the input and target output, respectively. The DAE structure can be divided into two parts: the encoder part (green box in Fig. 5.1) and the decoder part (yellow box in Fig. 5.1). The encoder part extracts the features of noisy input data. Then, the decoder part recovers the clean data.

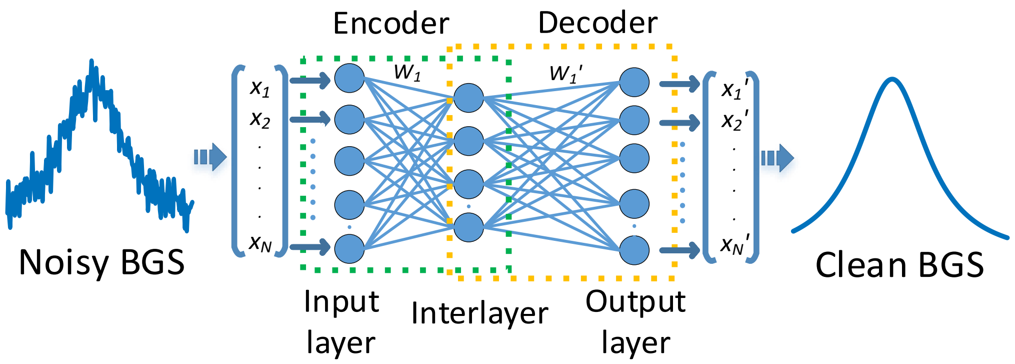

Fig. 5.1: The structure of a DAE used for denoising and feature extraction of the collected BGS in BOTDA.

For the DAE denoising, the simulated BGS with 201 frequency sampling points of the Lorentzian lineshape is used in the training process. Although adding the additive white Gaussian noise (AWGN) into the simulated clean BGS seems to conform to the nature of noise in BOTDA and can provide enough simulated noisy BGS for the training process [14-16], we have also tried the way of data corruption which was adopted in the previous work of DAE [17]. After repeated trials of these two different ways of generating simulated training data, involving adjustments of the noise level in the AWGN method and the corruption ratio in corruption methods, we find that the corruption method can provide better performance of the model. Thus, the corrupted BGS is chosen instead of the normal noisy BGS with AWGN for training in our experiment finally. For an example of corruption, when there are 200 sampling points in the BGS and a 20% corruption ratio is chosen, the values of 40 random points in the

BGS are set to 0. Repeated trials and optimization determine the final corruption ratio. After the training process of DAE, the experimentally collected BGS can be used as the input of the trained DAE. Then, the valuable features of input BGS will be extracted by the encoder part, which is used for the following temperature extraction task directly. On the other hand, the extracted information/features can be used to recover the clean BGS employing the decoder part. In this way, the whole DAE implements the BGS denoising. In this work, the recovered BGS by the DAE will be observed to show the capability of extracting useful features and suppressing the noise in input data when the DAEs are stacked to construct the DNN model for robust temperature extraction.

Figure 5.2 shows the DAE-based DNN model structure for temperature extraction in the BOTDA system, which contains one input layer, three hidden layers, and one output layer. In this structure, the hidden layers are formed by stacking the encoder parts of three DAEs after individual training of these DAEs. W_1, W_2, and W_3 represent the weight vectors in these three hidden layers, and W_o represents the weight vector of the output layer. Y is the output vector which contains only one element y_1, corresponding to the generated temperature. In this case, the input vector X represents the BGS data, and the N elements in X represents the frequency sampling points on BGS in BOTDA. After training all DAE hidden layers and the output layer, the DNN is trained as a whole model using the simulated clean BGS data as input and the corresponding temperature value as target output based on the classical error back-propagation (BP) algorithm. Then, the temperature can be directly generated in the testing process. Actually, we have optimized the number of hidden layers by repeated adjustments and trials. When the number of hidden layers increases from 1 to 3, the performance is improved. However, when it continues to increase, there is no noticeable performance improvement but the longer processing time induced. Thus, three hidden layers are determined finally.

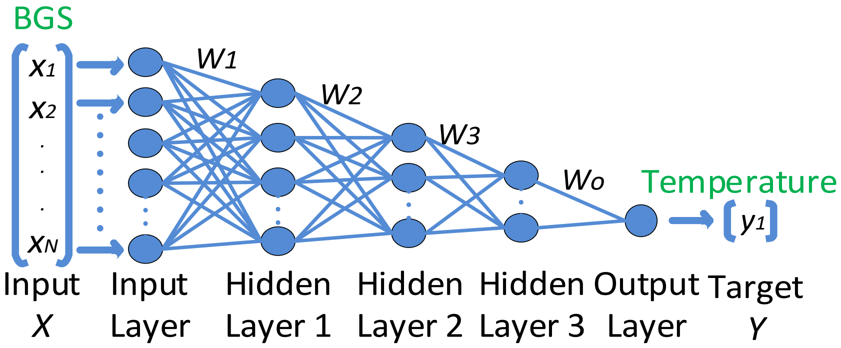

Fig. 5.2: Structure of the DNN model based on three DAE hidden layers used for direct temperature extraction from the noisy BGS for the BOTDA system.

The clean BGS data of Lorentzian lineshape are simulated based on Eq. (2.9). In our case, the range of ν is from 10.750GHz to 10.950GHz with a 1MHz interval, which is the same as the frequency scanning range during the acquisition of BGS data in the experiment. g_B is set to be 1 since the BGS is normalized. The BFS ν_B of the ideal BGS is determined by the temperature and pre-calibrated BFS-temperature coefficient of the FUT used in the BOTDA system. To generalize the model for different temperature conditions, 61 temperatures (20 to 80°C with 1°C interval) are used in training processes. Moreover, in order to accommodate BGS linewidth variations along the fiber, the range of $\Delta\nu_B$ varies from 20MHz to 120MHz with 4MHz interval, resulting in 26 $\Delta\nu_B$ cases of training data. Although the Brillouin linewidth is larger than 30MHz in most cases, the range of BGS linewidth in training data is set from 20MHz to ensure that the linewidths of all empirical data will arise in this range. In total, there are 1586 simulated ideal BGSs for training. The above setting of parameters to obtain the simulated ideal BGSs for training is based on the experimentally obtained BGS of the FUT. Furthermore, the choice of these parameters also depends on the optimization process of the DNN model through repeated trials for optimal performance. After appropriate training, the temperature of experimental BGS data can be obtained as the output of the DNN model directly as long as the temperature and bandwidth of the tested data are within the ranges used in the training data, no matter whether the data case takes place precisely in the training process. It is because the DNN model can learn the relation between the BGS and temperature instead of simply memorizing the appeared BGS-T pairs in training.

In addition, to strengthen further the robustness of the DNN model, a novel way of using the training data is investigated. Several identical simulated BGSs instead of one single BGS are combined to generate one new input vector in the training dataset while the corresponding target remains the same, which means the dimension of the input vector expands while the total quantity of input vectors for training remains the same. In testing, several adjacent collected BGS data around each local fiber position are combined as one input vector, and the corresponding temperature of the local point will be output by the DNN. Finally, after repeated trials and optimization processes, the DNN model using 5 BGSs as input at one time is chosen, and the optimal structure of the DNN model used for temperature extraction is decided to be 1005-120-25-5-1. The corruption ratio used in training is set to be 20%.

5.3 Experiment and results

Figure 5.3 shows the BOTDA experimental setup, which is almost the same as those used in previous chapters. The 20ns pump pulse light is used again (corresponding to 2m spatial resolution). The peak power of the pump power injected is 20dBm, and its extinction ratio (ER) is beyond 40dB in the experiment, which is high enough to avoid possible detrimental effects of poor ER. In addition, a polarization switch (PSW) is used to suppress the polarization-dependent noise instead of the polarization scrambler (PS). A 40.170km SMF serves as the FUT. The last 203m loose fiber section and a 6m loose fiber section are put into an oven. The other parts of FUT are put in the environment of room temperature as illustrated in Fig. 5.3. Experimental BGSs under different temperature conditions and different averaging times (16, 50, 150, 300, 500 for each polarization direction) are collected with 500MSample/s sampling rate. Then, the

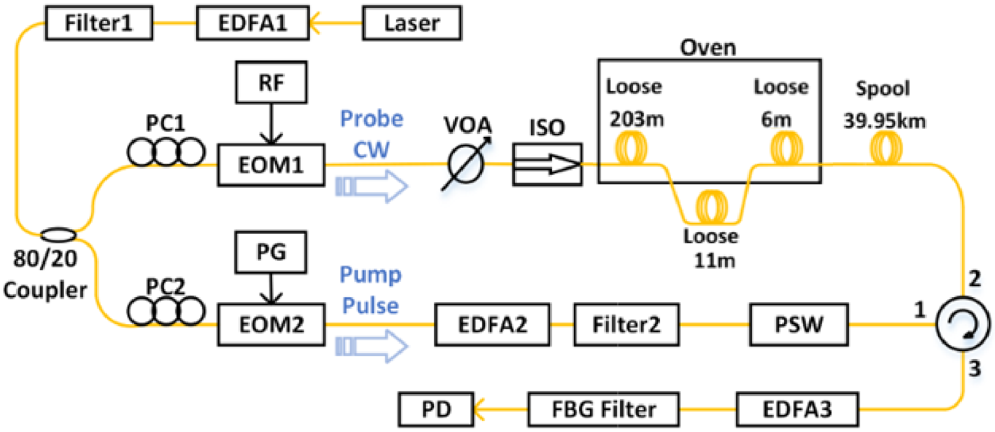

Fig. 5.3: BOTDA system setup.

optimized DNN model is used to extract the temperature from collected BGSs along the FUT after training.

To demonstrate the denoising effect of DAE on input collected data, both the collected BGS raw data along the 40.170km FUT and the corresponding BGS distribution after denoising by one single trained DAE are shown in Fig. 5.4. It is noticed that the BGS distribution becomes more evident and the noise level of BGS data decreases after the DAE processing. Besides, Figure 5.5 shows the measured BGS and recovered BGS after the DAE processing at the 2km and 40km distance, respectively. It is seen that the noise level has decreased significantly in the frequency-

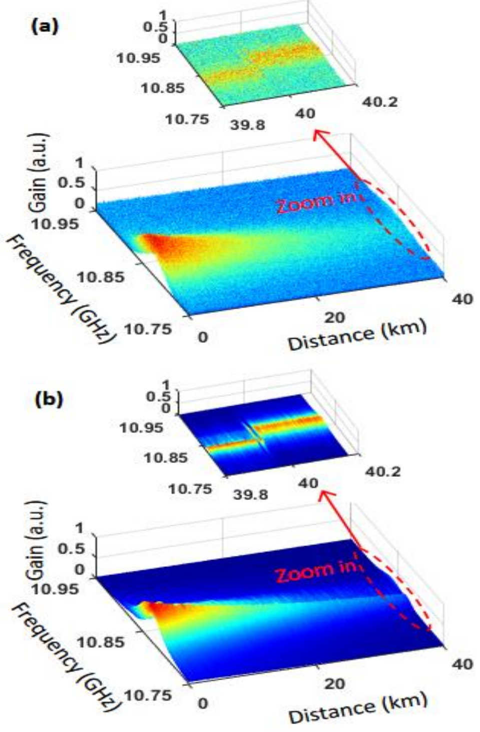

Fig. 5.4: (a) Measured BGS distribution along the 40.170km FUT with 16 averaging times; (b) reconstructed BGS distribution along the 40.170km FUT after processing by the trained DAE. Insets: BGS distribution along the last 400m FUT.

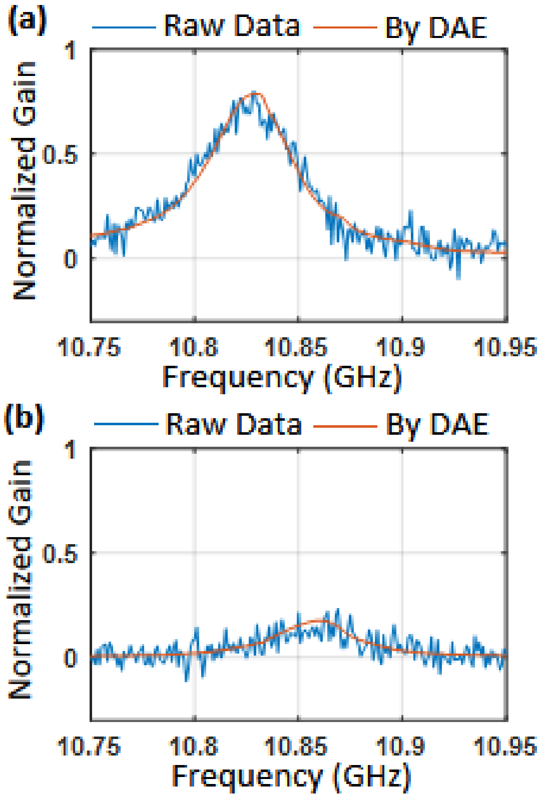

Fig. 5.5: (a) Measured BGS and reconstructed BGS by DAE at the 2km FUT position; (b) Measured BGS and reconstructed BGS by DAE at the 40km FUT position.

domain after using DAE, which demonstrates the denoising effect of DAE to extract useful features with suppression of noise from the BGS data. The SNR distribution of the raw data with 16 averaging times and the one denoised by the DAE method along the whole FUT are both shown in Fig. 5.6. The SNR is calculated by the ratio between the mean amplitude along that one trace at the BFS in room temperature and its standard deviation. In Fig. 5.6, the value of each SNR point is calculated using the mean amplitude of 200 adjacent spatial sampling points. After processing by the DAE, the averaging SNR has been improved by 9.96dB, compared to that of raw data, calculated by subtracting two SNR values at each spatial position and then averaging the differences at all positions.

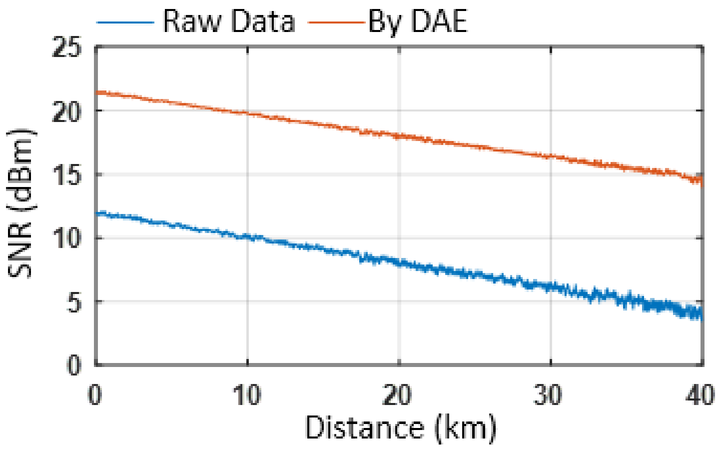

Fig. 5.6: The SNR distribution of raw data with 16 times of averaging and the corresponding one denoised by using DAE along the FUT.

After the individual training processes of three DAEs, the encoder parts of them are stacked together with a linear layer as the output layer to form the DNN model, which is used to extract the temperature information directly from the experimental BGS data after appropriate training. The following results are all obtained using the optimized 5-BGS DNN model with the optimal structure of 1005-120-25-5-1. The temperature distribution obtained by using the conventional LCF method and that obtained by using the DNN model are shown in Fig. 5.7, respectively. The temperature information of the whole FUT, including the temperature changing at some different positions, can be extracted accurately by the DNN method, and the uncertainty of temperature measured by the DNN is much less than that obtained by the LCF method.

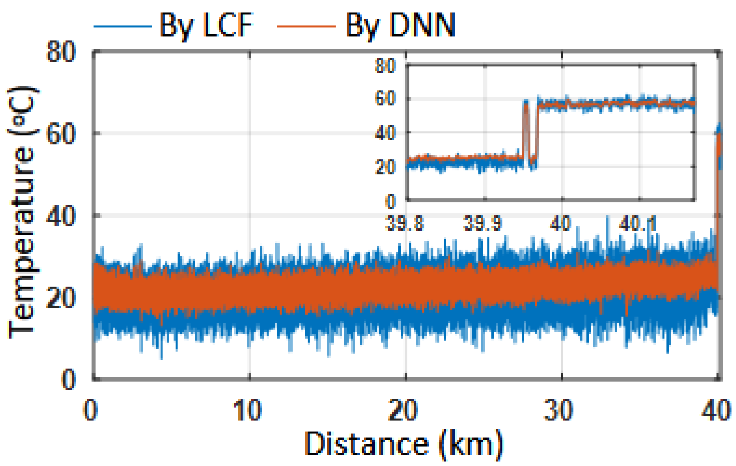

Fig. 5.7: The temperature distribution obtained by the conventional LCF method and by the DNN method along the whole 40.170km FUT when the temperature of the oven is set to be 55ºC. 16 times of averaging are used for BGS collection. Inset: the temperature distribution along the last 370m FUT.

Furthermore, to prove the actual robustness of the DNN model in terms of different SNR levels of the input BGS data, the error performance of temperature extracted by using the DNN method in the last 203m FUT is explored and compared with that obtained by using the conventional LCF method. Figure 5.8 shows the error performance parameters, including the SD and the RMSE calculated from 1015 data points along the last 203m FUT. The BGS data of different levels of SNR are collected with different averaging times, i.e., 16, 50, 150, 300, and 500, which correspond to the SNR levels of 4.6dB, 7.0dB, 8.9dB, 9.8dB, and 11.0dB in the last 203m FUT (obtained using the ratio between the mean amplitude along the last 203m FUT trace at the BFS in the heating temperature 55ºC and its standard deviation), respectively. Figure 5.8 shows that when the SNR of input data decreases from 9.8dB to 4.6dB, both the SD and RMSE of temperature obtained by the LCF increase obviously, while those obtained by the DNN only increase slightly, which shows the robustness of the DNN for temperature extraction. In particular, when the SNR is 4.6dB, corresponding to relatively low averaging times of 16, the measured temperature SD by the DNN is reduced from 2.4°C to 1.2°C, and the RMSE is reduced from 2.4°C to 1.3°C, compared to the corresponding results using the LCF. Thus, the proposed method based on DNN can be used in the data collection with low averaging times to reduce the data acquisition and processing time with only a slight sacrifice of the measurement accuracy. Note that the whole temperature distribution in Fig. 5.7 is obtained based on the assumption that the strain along the whole FUT on the fiber spool is zero. However, the strain on the fiber spool is not zero actually, contributing to the fluctuation and overall changing trend in the temperature distribution. In this case, it is difficult to determine the actual value of the strain or temperature in the fiber spool section. Moreover, this fact may have also contributed to the observed deviation between the extracted temperature using the DNN and LCF. Thus, evaluating the actual performance of the adopted methods is more credible based on the obtained temperature in the last heated FUT section with constant strain. Certainly, the evaluation of temperature fluctuation and deviation in the last heated FUT section is represented as the SD and RMSE in Fig. 5.8. The results show that not only the fluctuation but also the deviation from actual temperature (55°C) have been reduced by using the DNN method. And note that the temperature accuracy in the FUT end represented by the RMSE/SD in the case of 16 averaging times is improved by a factor close to 2 (3dB),

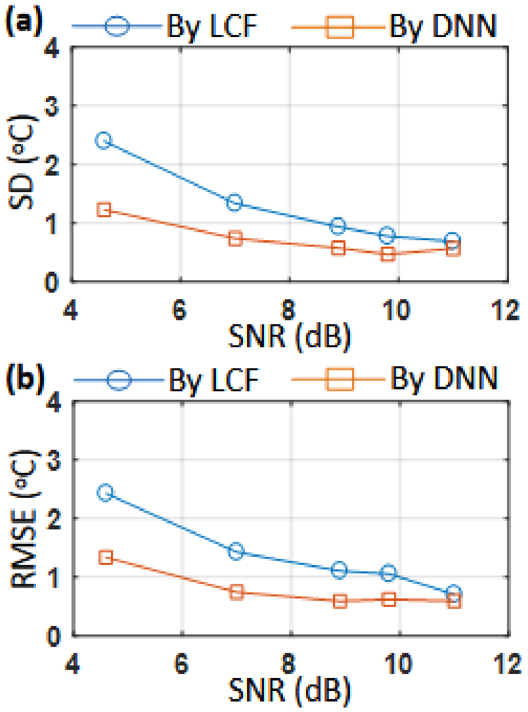

Fig. 5.8: (a) The SD of temperature along the last 203m FUT in different SNR conditions by the LCF method and by the DNN method, respectively; (b) the RMSE of temperature along the last 203m FUT in different SNR conditions by the LCF method and the DNN method, respectively.

while the average SNR of the whole trace is improved by 9.96dB. This inconsistency between the temperature accuracy and SNR improvement can be explained by the fact that the proportional relation between the temperature accuracy and the SNR is based on the supposed statistical independence of each point within the BGS. However, the use of DAE, which functions like a filter, will correlate all spectral points within the BGS and hence break the proportional relationship. Thus, the actual improvement of the temperature accuracy is not as significant as that of the SNR. This phenomenon has also been mentioned in Ref. [20].

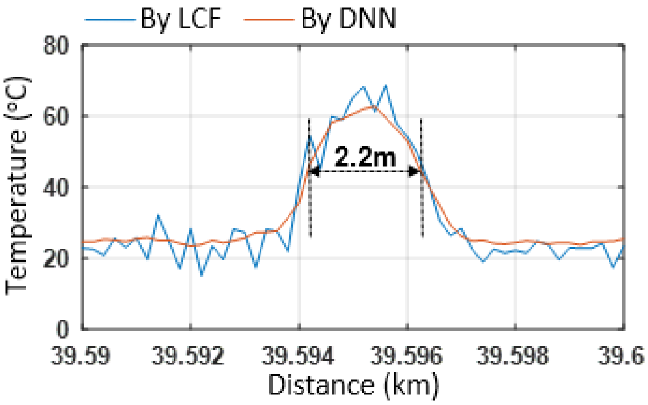

Fig. 5.9: The temperature distribution around a 2m heated FUT section obtained by the LCF and DNN method.

Besides, to demonstrate the actual spatial resolution using the proposed DNN method in our experiment, we add one group of measurements where the heated section is set to 2m which is equal to the ideal theoretical spatial resolution of 2m (20ns pump pulse in the experiment). The temperature distribution obtained by the LCF and DNN around the 2m heated FUT section is shown in Fig. 5.9, where the experimental spatial resolution is calculated to be 2.2m using the full width at half maximum (FWHM) of the section with transient temperature. Thus, the proposed DNN method only introduces a minimal degradation of the spatial resolution and can be effective in practical applications.

In order to compare the processing speed of the proposed DNN method with the LCF method, the processing time of data with five different averaging times is recorded and shown in Table 5.1. The processing of 200,000 BGSs along 40.170km SMF by the DNN method for temperature extraction requires only 4s, which is about 500 times shorter than the processing time needed by the LCF method. It is proved

Table 5.1: The processing time (unit: s) needed for temperature extraction of BGS along the whole 40.170km FUT using LCF and DNN methods

Averaging Times	***LCF***	***DNN***
16	2164.80s	4.22s
50	2132.76s	4.28s
150	2130.84s	4.32s
300	2144.30s	4.48s
500	2126.51s	4.20s

that the proposed DAE-based DNN method can improve the processing speed and enhance the accuracy of extracted temperature in different SNR conditions. Since this method using the DAE-based DNN is proposed as a fast and robust temperature extraction method for BOTDA, we also compare its performance with that of the SVM method, which has been proved to be an ultrafast temperature extraction method in Ref. [15]. In [15], the SNR of raw data with trace averaging times of 16, 50, 200, and 400 is measured to be 4.3 dB, 6.1 dB, 8.6 dB, and 9.9dB, respectively, which are very similar to the conditions in our experiment. However, the improvement of SD/RMSE provided by the SVM is less than 1dB in these cases. In addition, the SVM method's processing speed is 125 times faster than that of the LCF method. Thus, the speed of the proposed DNN method in this work is 4 times faster than the SVM with greater tolerance of low SNR as well.

5.4 Summary

In conclusion, this chapter demonstrates a new method of using DAE-based DNN for temperature extraction in the BOTDA sensing system. The DAE serves as the primary block of the DNN and is trained individually to denoise the experimental noisy BGS data, which shows that the noise level could be reduced in the reconstructed BGS, and the SNR can be improved by 9.96dB in our experiment. The useful features of input BGS have been successfully extracted by the encoder part of DAE, with the noise primarily suppressed in the meanwhile. Our experimental results using the proposed DNN method have proved the robustness of the DAE-based DNN for direct temperature extraction under different SNR levels for the experimental data compared with those using the conventional LCF method. In the case of 4.6dB SNR of experimental data, the SD/RMSE of measured temperature at the end of the 40.170km FUT are reduced from 2.4ºC/2.4ºC to 1.2ºC/1.3ºC by using the DNN when compared with those using LCF. In addition, about 500 times processing time reduction due to the use of the proposed DNN method has been demonstrated. Our DAE-based DNN for temperature extraction combines the advantages of both denoising and fast processing speed, which makes it a promising method for robust and fast temperature extraction in BOTDA systems. In addition, this DAE-based DNN method also has the potential on other similar sensing systems based on Brillouin scattering for robust and fast extraction of measurand information. Moreover, we believe that this work using the DAE-based DNN can be helpful for the further detailed comparison between different neural network methods applied in BOTDA systems in the future.

References

[21] X. Bao and L. Chen, "Recent progress in Brillouin scattering based fiber sensors," *Sensors*, vol. 11, no. 4, pp. 4152-4187, 2011.

[22] A. Barrias, J. R. Casas, and S. Villalba, “A review of distributed optical fiber sensors for civil engineering applications,” *Sensors*, vol. 16, no. 5, 748, 2016.

[23] C. Hong, Y. Zhang, G. Li, M. Zhang, and Z. Liu, “Recent progress of using Brillouin distributed fiber sensors for geotechnical health monitoring,” *Sensors and Actuators A: Physical*, vol. 258, pp. 131-145, 2017.

[24] M. Soto, X. Angulo-Vinuesa, S. Martin-Lopez, S. Chin, J. Ania-Castanon, P. Corredera, E. Rochat, M. Gonzalez-Herraez, and L. Thevenaz, "Extending the real remoteness of long-range Brillouin optical time-domain fiber analyzers," *J. Lightwave Technol.*, vol. 32, no. 1, pp. 152-162, 2014.

[25] S. Diakaridia, Y. Pan, P. Xu, D. Zhou, B. Wang, L.Teng, Z. Lu, D. Ba, and Y. Dong, “Detecting cm-scale hot spot over 24-km-long single-mode fiber by using differential pulse pair BOTDA based on double-peak spectrum,” *Opt. Express*, vol. 25, no. 15, pp. 17727-17736, 2017.

[26] X. Jia, H. Chang, K. Lin, C. Xu, and J. Wu, “Frequency-comb-based BOTDA sensors for high-spatial-resolution/long-distance sensing,” *Opt. Express*, vol. 25, no. 6, pp. 6997-7007, 2017.

[27] M. A. Soto, L. Thévenaz, “Modeling and evaluating the performance of Brillouin distributed optical fiber sensors,” *Opt. Express,* vol. 21, no. 25, pp. 31347-31366, 2013.

[28] A. Dominguez-Lopez, X. Angulo-Vinuesa, A. Lopez-Gil, S. Martin-Lopez, and M. Gonzalez-Herraez, “Non-local effects in dual-probe-sideband Brillouin optical time domain analysis,” *Opt. Express*, vol. 23, no. 8, pp. 10341-10352, 2015.

[29] L. Thévenaz, S. F. Mafang, and J. Lin, “Effect of pulse depletion in a Brillouin optical time-domain analysis system,” *Opt. Express*, vol. 21, no. 12, pp. 14017-14035, 2013.

[30] M. Alem, M. A. Soto, and L. Thévenaz, “Modelling the depletion length induced by modulation instability in distributed optical fibre sensors,” *in Proc. SPIE, 23rd International Conference on Optical Fiber Sensors 2014 (OFS)*, paper 91575S, pp. 1-4, Spain, 2014.

[31] M. A. Soto, J. A. Ramírez, and L. Thévenaz, “Intensifying the response of distributed optical fibre sensors using 2D and 3D image restoration,” *Nat. Commun.,* 7, 10870, 2016.

[32] H. Wu, L. Wang, Z. Zhao, N. Guo, C. Shu, and C. Lu, "Brillouin optical time domain analyzer sensors assisted by advanced image denoising techniques," *Opt. Express*, vol. 26, no. 5, pp. 5126-5139, 2018.

[33] H. Wu, Y. Wan, M. Tang, Y. Chen, C. Zhao, R. Liao, Y. Chang, S. Fu, P. P. Shum, and D. Liu, "Real-time denoising of Brillouin optical time domain analyzer with high data fidelity using convolutional neural networks," *J. Lightwave Technol.*, vol. 37, no. 11, pp. 2648-2653, 2018.

[34] Azad, L. Wang, N. Guo, H. Tam, and C. Lu, "Signal processing using artificial neural network for BOTDA sensor system," *Opt. Express*, vol. 24, no. 6, pp. 6769-6782, 2016.

[35] H. Wu, L. Wang, N. Guo, C. Shu and C. Lu, "Brillouin optical time domain analyzer assisted by support vector machine for ultrafast temperature extraction," *J. Lightwave Technol.*, vol. 35, no. 19, pp. 4159-4167, 2017.

[36] B. Wang, N. Guo, L. Wang, C. Yu, and C. Lu, "Denoising and robust temperature extraction for BOTDA systems based on denoising autoencoder and DNN," *in Proc. SPIE, 26th International Conference on Optical Fiber Sensors 2018 (OFS)*, paper WF29, pp. 1-4, Switzerland, 2018.

[37] P. Vincent, H. Larochelle, I. Lajoie, Y. Bengio, and P. Manzagol, "Stacked denoising autoencoders: learning useful representations in a deep network with a local denoising criterion," *Journal of machine learning research*, pp. 3371-3408, 2010.

[38] X. Lu, Y. Tasao, S. Matsuda, and C. Hori, "Speech enhancement based on deep denoising autoencoder," *Interspeech 2013*, pp. 436-440, France, 2013.

[39] J. Li, Z. Struzik, L. Zhang, and A. Cichocki "Feature learning from incomplete EEG with denoising autoencoder," *Neurocomputing*, vol. 165, pp. 23-31, 2015.

[40] S. Zaslawski, Z. Yang, M. A. Soto, and L. Thévenaz, "Impact of fitting and digital filtering on signal-to-noise ratio and Brillouin frequency shift uncertainty of BOTDA measurements," *in Proc. SPIE, 26th International Conference on Optical Fiber Sensors 2018 (OFS)*, paper ThE27, pp. 1-4, Switzerland, 2018.

6 Long-distance BOTDA sensing systems using Video-BM3D denoising for both static and slowly varying environment

In this chapter, we propose and demonstrate the video block-matching and 3D filtering (VBM3D) denoising experimentally for the first time in a 100.8km long-distance BOTDA sensing system with 2m spatial resolution. We have performed both experiments under static and slowly varying temperature environments. In static temperature measurement, a temperature uncertainty of 0.43°C has been achieved with denoising by VBM3D. As far as we know, this is one of the best temperature uncertainties reported for BOTDA with a sensing distance beyond 100km. On the other hand, the temperature at the end of 100.8km fiber has also been accurately measured in slowly varying temperature measurements. VBM3D exploits both the spatial and temporal correlations of the data for denoising. As a result, it can significantly reduce temperature fluctuations and keep the measured values close to the actual temperature even if the temperature is temporarily changing. We believe it would be helpful for long-distance sensing where the measurand may have temporal evolution in the slowly varying environment.

6.1 Motivation

As discussed in previous chapters, temperature-strain cross-sensitivity is one of the significant issues in BOTDA systems, which makes it challenging to achieve simultaneous temperature and strain measurement [1]. Besides the temperature-strain cross-sensitivity, achieving a long sensing distance beyond 100km is also challenging. The signal-to-noise ratio (SNR) is a crucial parameter that directly limits the measurement accuracy and the sensing distance. Due to the fiber attenuation, the SNR worsens, and the measurement accuracy degrades for longer sensing distances, limiting the sensing distance. Although increasing injected powers of the pump and probe light can enhance the SNR in principle, the highest pump and probe powers are limited by the non-local effect [2] and fiber nonlinearities [3], respectively. Therefore, to extend the sensing range beyond 100km with acceptable spatial resolution and measurement accuracy, some techniques have been proposed, including optical pulse coding [4-10], time/frequency-division multiplexing [11-13], Raman amplification [7,8,13-17], random fiber laser amplification [14,18], novel probe modulation and scanning [19-21], Brillouin loss configuration [21], and optical chirp chain BOTDA [22]. The works mentioned above with sensing distances beyond 100km are summarized in Table 6.1. However, most of the above methods require modifications of the conventional BOTDA setup, making the system more complicated.

On the other hand, image denoising techniques have been used to improve the SNR without the need to modify the conventional setup, such as non-local means (NLM) and wavelet denoising (WD) [23]. The NLM reduces the noise by using the non-local principle based on the high degree of similarity and redundancy contained in the sensing data, while the WD filters the noise by using wavelet transform and wavelet shrinkage. A 50km sensing distance with 0.19MHz BFS uncertainty using the 2D WD has been demonstrated [23]. Moreover, NLM denoising in a conventional BOTDA setup has helped to achieve a 100km sensing distance with 0.77MHz BFS uncertainty and 2m spatial resolution [24], as summarized in Table 6.1. Recently we have proposed a novel block-matching and 3D filtering (BM3D) image denoising method to enhance the SNR [25]. Since BM3D combines the advantages of NLM and WD, it achieves better measurement accuracy with less spatial resolution degradation compared to NLM and WD for denoising [25]. However, all these image denoising methods only exploit the data correlation in the space domain for denoising, while ingnoring the temporal data correlation usually. Thus, the 2D image denoising techniques are only suitable for the static environment where the measurand remains unchanged without temporal evolution. In fact, the temporal data correlation can also be used together with the spatial data correlation for better denoising performance, especially when the measurand varies slowly with time. Utilizing both the temporal and spatial correlation of the data for denoising, 3D video denoising can easily deal with the situations for both the static and slowly varying environment, which denoise the video sequence formed by consecutive measurements of 2D BGS distribution along the FUT. The video sequence is similar to that in a BOTDA of 50km sensing distance using the NLM video denoising [23].

Table 6.1: Summary of previous works in BOTDA with sensing distance beyond 100km

Techniques	Fiber Length	Resolution	BFS Uncertainty
Bipolar pulse coding [4]	100km	2m	0.8MHz
Simplex coding [5]	120km	3m	3.1MHz
Frequency coding [6]	100km	3m	1.5MHz
RZ pulse coding and second-order Raman amplification [7]	100/120km	3/5m	1.5/1.9MHz
Distributed Raman amplification (DRA) and simplex coding [8]	142.2km	5m	1.5MHz
Cyclic coding [9]	164km	1m	3MHz
Bipolar coding [10]	100km	2m	0.9MHz
Time-division multiplexing (TDM) [11]	100km	2m	2MHz
Frequency-division multiplexing (FDM) [12]	150km	2m	1.5MHz
Distributed Raman and Brillouin amplifications, FDM, TDM [13]	150.62km	9m	0.82MHz
Random fiber laser (RFL) based hybrid distributed Raman amplification (H-DRA) [14]	154.4km	5m	1.4MHz
First-order Raman amplification [15]	100km	2m	1.2MHz
Second-order Raman amplification [16]	100km	2m	3MHz
First-order bi-directional Raman amplification [17]	120km	2m	2.1MHz
High-order random fiber laser amplification (RFLA) [18]	175km	8m	2.06MHz
Orthogonally-polarized four-tone probe [19]	104km	2m	5MHz
Novel probe scanning with fixed frequency difference [20]	100km	2m	2.4MHz
Brillouin loss configuration and probe frequency modulation [21]	100km	1m	1MHz
Optical chirp chain (OCC) and pattern recognition [22]	100km	4m	1.3MHz
Non-local means (NLM) image denoising [24]	100km	2m	0.77MHz

In this chapter, we extend the BM3D image denoising to video denoising, i.e., VBM3D, to involve one more temporal dimension and take the dynamical property of the environment into account. The following content is organized in this way: Section 6.2 describes the principle and algorithm of VBM3D. Section 6.3 analyzes and optimizes the primary parameters in the VBM3D algorithm. This section also includes the experiment results performed for both the static and slowly varying temperature environments using VBM3D. For the static temperature measurement, a BFS uncertainty of 0.44MHz (0.43°C temperature uncertainty) with 100.8km sensing distance and 2m spatial resolution has been achieved. Furthermore, the slowly varying temperature at the end of 100.8km FUT has also been measured successfully after VBM3D denoising. Finally, Section 6.4 gives the summary.

6.2 Working principle of VBM3D denoising

VBM3D is one of the state-of-the-art video denoising methods developed in 2007 for the first time [26]. It reduces the noise by exploiting the signal's spatial and temporal correlation. When using the VBM3D for BOTDA signal denoising, each 2D (position-frequency) measurement (i.e., one BGS distribution sample along the FUT collected by the BOTDA) constitutes one frame of a video sequence (e.g., Frame 1, 2, 3 in Fig. 6.1). And successive measurements can obtain more video frames to form the 3D video sequence, which will be denoised by VBM3D then. Figure 6.1 illustrates the flowchart of the proposed VBM3D denoising for BOTDA. Similar to 2D BM3D denoising [27], VBM3D denoising also consists of two repetitive phases (Phase 1 and Phase 2), and each phase includes three similar steps: grouping, hard-thresholding (in Phase 1)/collaborative Wiener filtering (in Phase 2), and aggregation. Only the second step is different between Phase 1 and Phase 2. The brief procedures of these three steps in each phase are expressed as follows:

1) Grouping. In this step, matched blocks noted as “M”, which are similar to the reference block noted as “R”, are searched using the block-matching method and then stacked together to form a 3D array for each reference block in the video, as shown in Fig. 6.1. A straightforward approach to extend BM3D to VBM3D is to use a fixed-size 3D video search neighborhood. However, using a large size will lead to high computation complexity, while using a small size will give rise to unsatisfactory grouping and poor denoising results. Thus, the predictive-search block-matching method is utilized in VBM3D instead of the typical block-matching method used in BM3D for grouping. The predictive-search block-matching method includes two parts: an exhaustive-search block-matching and a predictive search [26]. It should be noted that the search range of block-matching in VBM3D is 3D video sequences rather than 2D images as in BM3D.

2) Hard-thresholding/collaborative Wiener filtering. The hard-thresholding and collaborative Wiener filtering are two different approaches to achieving 3D transform-domain shrinkage. First, following step 1 of Phase 1, we apply a 3D transform on the 3D array from step 1. Second, we use the hard-thresholding (in Phase 1) to reduce the noise and invert the 3D transform to generate estimates of

all grouped blocks. Then we return all basic estimated blocks to their original positions. After finishing an entire loop of Phase 1 (including steps 1-3), we repeat steps 1-3 in Phase 2 again, using the collaborative Wiener filtering in step 2 instead, to boost the denoising performance further and obtain the final estimates.

3) Aggregation. After step 2, we can obtain a basic (in Phase 1)/final (in Phase 2) estimate of the genuine video frames by aggregating all of the local estimates produced from step 2 with a weighted average.

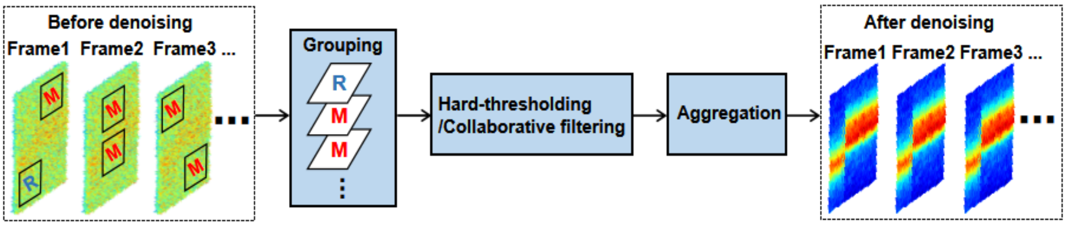

Fig. 6.1: Flowchart of the proposed VBM3D denoising mothed for BOTDA. “R” and “M” represent the reference blocks and the matched ones.

The experimental noise results from all equipment and components of the experimental system, especially the laser, EDFA and PD. And the total experimental noise in the BOTDA system is usually considered a Gaussian noise, denoted as $\eta(\cdot)\sim\mathcal{N}(0,\sigma^2)$. The collected noisy video is regarded as $z(x)=y(x)+\eta(x)$, where y is the actual video signal and η represents the noise. Here, $x=(x_1,x_2,t)$ are coordinates in the 3D spatio-temporal domain. The first two components (x_1,x_2) are the spatial coordinates, and the third one t is the time (frame) index (coordinate). The noise variance σ^2 is assumed a priori known, and the standard deviation (SD) σ of noise is set to an estimated value before using the VBM3D algorithm. To specify the

VBM3D denoising method containing two phases (each phase containing three steps) more clearly, we introduce the VBM3D algorithm in detail as follows [26]:

1) Phase 1. Obtaining a basic estimate by grouping within the noisy video and the collaborative hard-thresholding method.
    a) For each coordinate x, we perform: $S_x = PS\text{-}BM(Z_x)$, where Z_x represents a block in the noisy video z at the position x;
    b) $\hat{Y}_{S_x} = T_{3D}^{-1}(HARD\text{-}THR(T_{3D}(Z_{S_x}), \lambda_{3D}\sigma))$, where $\hat{Y}_{S_x}$ is a group of the blockwise estimates $\hat{Y}^x_{x'}$, $\forall x' \in S_x$;
    c) We produce the basic estimate of the entire video $\hat{y}^{basic}$ by aggregation of the blockwise estimates $\hat{Y}^x_{x'}$ at each position x, using weighted averaging while $weight(\hat{Y}^x_{x'}) = \frac{1}{\sigma^2 N_{har}(x)} W_{2D}$;
2) Phase 2. Obtaining the final estimate by grouping within the noisy video and the collaborative Wiener filtering method that uses the spectra of the corresponding groups from the basic estimate.
    a) For each coordinate x, we perform: $S_x = PS\text{-}BM(\hat{Y}^{basic}_x)$;
    b) $\hat{Y}_{S_x} = T_{3D}^{-1}\left(T_{3D}\left(Z_{S_x}\right)\frac{\left[T_{3D}\left(\hat{Y}^{basic}_{S_x}\right)\right]^2}{\left[T_{3D}\left(\hat{Y}^{basic}_{S_x}\right)\right]^2+\sigma^2}\right)$, where T_{3D} and T_{3D}^{-1} denotes the 3D transform and inverse 3D transform.
    c) We produce the final estimate of the entire video $\hat{y}^{final}$ by aggregation of $\hat{Y}^x_{x'}$, using weighted averaging while $weight\left(\hat{Y}^x_{x'}\right) = \sigma^{-2}\left\|\frac{[T_{3D}(\hat{Y}^{basic}_{S_x})]^2}{[T_{3D}(\hat{Y}^{basic}_{S_x})]^2+\sigma^2}\right\|_2^{-2} W_{2D}$, where $\|\cdot\|_2$ denotes $\ell^2\text{-}norm.$

Notation:

- Z_x denotes a block of size $N_1 \times N_1$ in z , whose upper-left corner is position x. $\hat{Y}_{x\prime}^{x}$ and $\hat{Y}_{x}^{basic}$ use similar notations. The former is an estimate for the block located at position x', obtained while processing the reference block Z_x. And the latter is a block located at position x extracted from the basic estimate $\hat{y}^{basic}$.
- $S_x = PS\text{-}BM(Z_x)$ performs predictive-search block-matching using Z_x as a reference block, where the set S_x are the results, containing the coordinates of the matched blocks. For Phase 2, we perform the search process inside the basic estimate instead of inside the noisy video.
- Z_{S_x} represents a group (i.e., a 3D array) formed by stacking together the blocks $Z_{x \in S_x}$. The same notation is used for $\hat{Y}_{S_x}$ and $\hat{Y}_{S_x}^{basic}$. The size of these groups is $N_1 \times N_1 \times |S_x|$.
- $HARD\text{-}THR(T_{3D}(Z_{S_x}), \lambda_{3D}\sigma))$ applies the hard-thresholding on the coefficients in the 3D transform domain using threshold $\lambda_{3D}\sigma$, where λ_{3D} is a constant threshold parameter. In detail, the hard-thresholding makes two conditional operations on the transform coefficients: when the values of the coefficients are less than the threshold, we set them to zero; and when the values of the coefficients are larger than or equal to the threshold, we reserve them.
- $N_{har}(x)$ is the number of nonzero coefficients retained after hard-thresholding $T_{3D}(Z_{S_x})$. Since the DC is always reserved, $N_{har}(x) > 0$.
- W_{2D} is a 2D Kaiser window of size $N_1 \times N_1$.

6.3 Experiment and results

6.3.1 BOTDA setup

Figure 6.2 shows the BOTDA experiment setup used to measure BGS distribution along the FUT for VBM3D denoising. This system is similar to those used in previous chapters. The sweepomg frequency of the RF source is from 10.751GHz to 10.950GHz with 1MHz interval. Again, we use 20ns pump pulse, corresponding to 2m spatial resolution. The pump peak power and probe power injected into the FUT are 20dBm and -3dBm, respectively, which are below the upper limits to avoid the non-local effect [2] and fiber nonlinearities [3]. The extinction ratio of the pump pulse in our experiment is 40dB. In addition, a polarization scrambler (PS) is used to suppress the polarization dependent noise. After passing through the FUT, the probe signal is amplified by EDFA3 and filtered to remove the higher frequency sideband. Finally, it is detected by a 125 MHz photodetector and collected on an oscilloscope. The sampling rate of 500MSample/s is adopted for data collection on an oscilloscope, which means 0.2m spatial distance between two adjacent data points. A 100.8km long SMF is used as the FUT, and its last 196m fiber section is put in the oven to evaluate the measurement accuracy at the far end of the FUT. Another 2.3m loose fiber section is also put inside the oven to verify the experimental spatial resolution. In the experiment for static temperature measurement, we adopt 2000 times averaging. For experiments with slowly varying temperature , we choose 200 times averaging instead to not only accelerate the total data collection speed but also maintain good signal quality for each group of data.

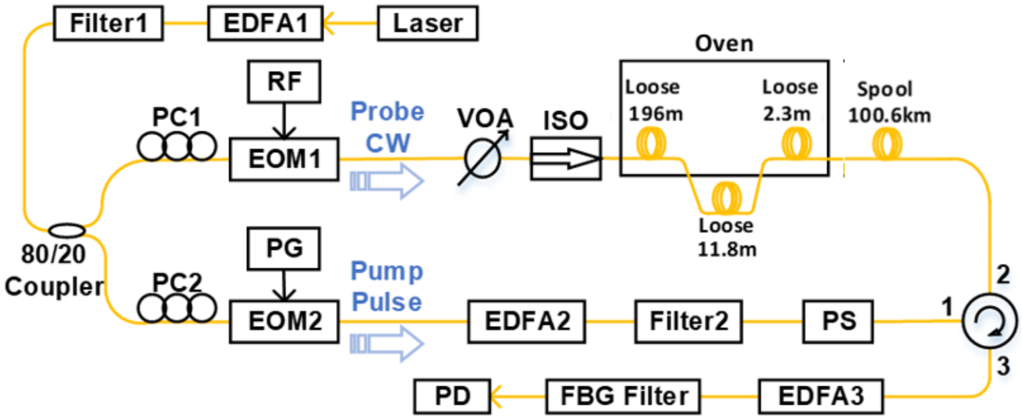

Fig. 6.2: BOTDA experiment setup.

6.3.2 Optimization of VBM3D parameters

At first, we monitor and analyze the effect of the VBM3D parameters on the denoising performance by experiment. The parameters of VBM3D include the estimated SD of the experimental noise σ, the fixed block size, the maximum number of similar blocks, the search-window sliding step, the search neighborhood range, the threshold for the block distance, and the threshold for the hard-thresholding λ_{3D}. Among them, σ and λ3D, two primary parameters, are found to impact the denoising performance significantly. Thus, we focus on these two parameters and optimize them using experimental data obtained under the static temperature environment (the oven temperature maintains 60°C). In our experiment, we take 20 consecutive measurements of BGS distribution along the last 300m FUT to form a video sequence, corresponding to a maximum frame number of 20. Then the video is denoised by VBM3D. Using LCF and the BFS-temperature coefficient (1.034MHz/°C) of the FUT, we can obtain the temperature distribution, from which we calculate the temperature uncertainty at the FUT end to evaluate the denoising performance. Moreover, we randomly select one frame (the 15th frame in our case) from these 20 frames for the following performance comparisons. In our tentative trials, we find that by increasing the value of λ_{3D} better temperature uncertainty is observed, but no more improvement is seen when its value is larger than 6. Thus, we set the value of λ_{3D} to be 6 at first and then gradually change the value of σ from 0.004 to 0.78. The obtained temperature uncertainty at the end of FUT in the 15th frame after denoising by VBM3D (the frame number is set to be 20) is shown in Fig. 6.3(a). The uncertainty decreases significantly from 8.86°C to 0.43°C while σ increases from 0.004 to 0.20. Then the uncertainty keeps almost unchanged even if σ still increases. Therefore, to avoid over-denoising and maintain excellent denoising performance, the value of σ is chosen to be 0.20. On the other hand, we keep the value of σ to be 0.20 and gradually increase the value of λ_{3D} from 0.1 to 20 (the frame number is set to be 20). The result is shown in Fig. 6.3(b), where we can see that the uncertainty decreases significantly and then keeps at the level of 0.43°C when λ_{3D} is larger than 3. We also find that when the frame number is smaller than the maximum value of 20, larger λ_{3D} is needed for the temperature uncertainty to reach a minimum value. To guarantee optimal performance for different frame numbers, we use a little larger value for λ_{3D}, i.e., 6 in our case. Finally, considering the effect of other parameters, the values of σ and λ3D are determined to be 0.2 and 6 for the following experiment under both static and slowly varying temperature environments, respectively.

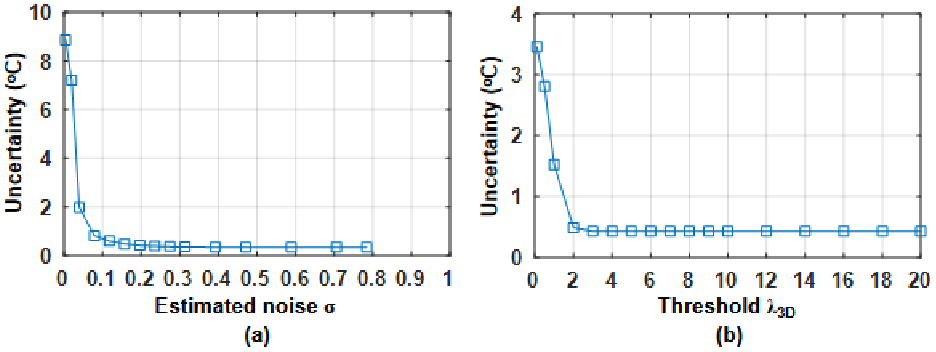

Fig. 6.3: Temperature uncertainty as a function of (a) estimated SD of noise σ; (b) threshold λ3D.

6.3.3 VBM3D denoising under a static temperature environment

As mentioned above, under a static temperature environment, 20 consecutive measurements of BGS distribution along the last 300m FUT have been taken to form a video sequence, meaning the maximum frame number can be set to be 20. Here we set

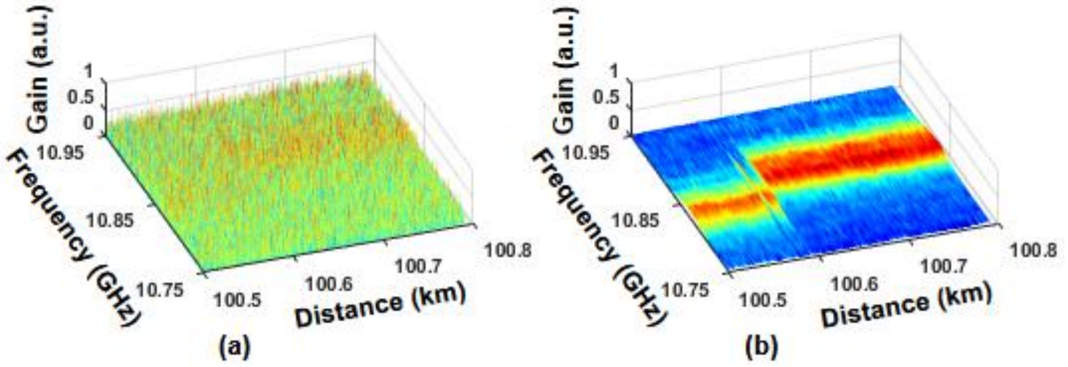

Fig. 6.4: One of the 20 measured BGS distributions along the last 300m FUT (a) before denoising; (b) after denoising by using VBM3D with a frame number of 20.

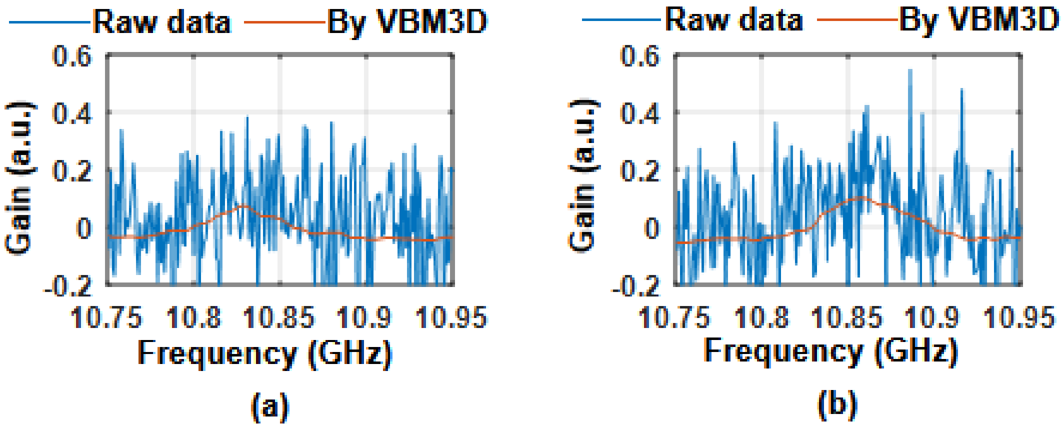

Fig. 6.5: Two BGSs at the locations of (a) 100.53km and (b) 100.74km with/without VBM3D denoising.

the frame number to be the maximum value of 20 for denoising at first. Fig. 6.4(a) shows one of the 20 measured BGS distributions along the last 300m FUT without the denoising by VBM3D, where the two heated FUT sections in the oven can not be observed due to very low SNR at the FUT end. As a contrast, Fig. 6.4(b) gives the corresponding BGS distribution after denoising by using VBM3D with a frame number of 20, where an SNR improvement of 13.2dB (improved from -2.4dB to 10.8dB) has been achieved, and the two heated sections are clearly observed at the FUT end. Note that the SNR is calculated using a 20m fiber section (101 data points) at the FUT end. And the 15th frame from these 20 frames is randomly selected for analysis, and other frames all exhibit similar performance. From Fig. 6.4, we plot two BGSs at the locations of 100.53km (at room temperature) and 100.74km (heated at 60°C) before and after denoising, as shown in Fig. 6.5, implying that clear BGSs can be reconstructed from the raw data after denoising by VBM3D.

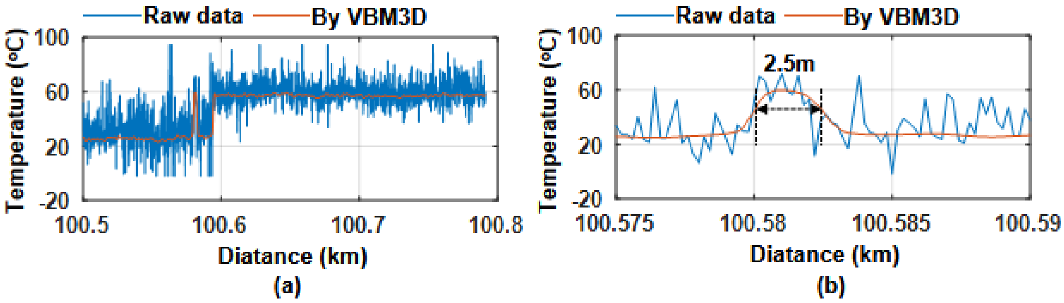

Fig. 6.6: Temperature distribution before and after denoising by VBM3D (a) along the last 300m FUT; (b) around the 2.3m heated section.

Then, the corresponding temperature distribution is obtained using LCF and the BFS-temperature coefficient (1.034MHz/°C), as shown in Fig. 6.6(a). It is clear that the temperature fluctuations are reduced significantly after denoising by VBM3D. Hence the temperatures of the two heated sections at the FUT end are precisely observed. The temperature uncertainty at the far end of FUT is improved from 9.0°C of raw data to 0.43°C (0.44MHz BFS uncertainty) after denoising by VBM3D. Fig. 6.6(b) shows the temperature distribution around the 2.3m heated section, and indicates an experimental spatial resolution of 2.5m (calculated using the full width at half maximum (FWHM) of the temperature transition section [28]), which has a minimal degradation of the spatial resolution after denoising. This result agrees well with our previous work of using 2D BM3D denoising for BOTDA [25], showing the advantage of BM3D denoising again. It is worth mentioning that in Fig. 6.4 and Fig. 6.6, we only present the data along the last 300m FUT because our oscilloscope does not have enough memory to collect the data along the whole 100.8km FUT at the sampling rate of 500MSample/s. Since the temperature only changes at the end of FUT and other sections of FUT remain at room temperature, the data along the last 300m FUT is good for demonstrating temperature measurement at the worst SNR.

It is worth mentioning that the frame number is also a key parameter in VBM3D, which determines the search range during the block-matching process. Hence the frame number will also affect the denoising performance. In the results of Fig. 6.4 to Fig. 6.6, we use the maximum frame number of 20 in VBM3D denoising, which means that the block search range is the whole 20 measurements of the BGS distribution. In order to analyze the denoising performance using VBM3D with different frame numbers, we change the frame number in the VBM3D algorithm. Fig. 6.7 shows the temperature uncertainty at the far end of FUT as a function of the frame number, where the best temperature uncertainty among all frames after denoising is adopted. When the frame number is 1, there is only one measurement of BGS distribution, and VBM3D works the same way as 2D BM3D. Note that for static temperature environment, we adopt 2000 times averaging for each measurement. The temperature uncertainty obtained using VBM3D with the frame numbers 1, 2, 5, 10, 15, and 20 are 2.13, 1.93, 1.38, 1.12, 0.52, and 0.43°C, respectively. We can see that the temperature uncertainty becomes better with the increase of the frame number, which indicates the superiority of the VBM3D over the 2D BM3D that VBM3D can use not only the spatial correlation within each frame but also the temporal correlation among different frames for denoising. The temporal correlation used in denoising is significant in the slowly varying temperature measurement, which will be verified in the next section. Moreover, as a comparison, the temperature uncertainty obtained by using linear averaging of multiple measurements is also given in Fig. 6.7. The temperature uncertainty obtained using linear averaging of 1, 2, 5, 10, 15, and 20 measurements are 9.0, 6.2, 4.1, 3.1, 2.8 and 2.5°C, respectively. The temperature uncertainty obtained by VBM3D is much smaller than that by linear averaging, showing the capability of VBM3D to achieve accurate data denoising rather than just averaging redundant data.

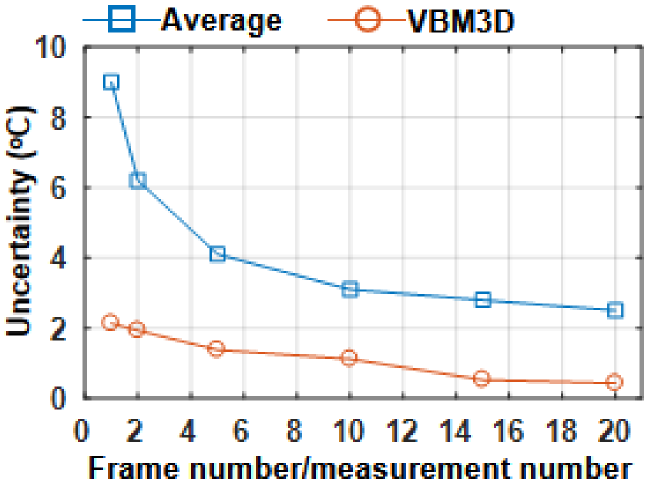

Fig. 6.7: Temperature uncertainty obtained by using VBM3D and linear averaging as a function of frame number (for VBM3D) or measurement number (for linear averaging).

6.3.4 VBM3D denoising under a slowly varying temperature environment

In this section, we perform the experiment under a slowly varying temperature environment, where the temperature inside the oven changes slowly. In the beginning, the temperature in the oven is kept at 40°C and stabilized for about 40mins. Then, it increases linearly from 40°C to 60°C, which lasts about 140mins. At last, it remains at

60^{o}C for about 45mins. Therefore, the whole temperature change process occupies a time of 225mins, controlled by a computer program connected to the oven. Thus the temperature in the oven changes by 20^{o}C within 140mins, corresponding to a temperature change speed of 0.14^{o}C/minute. For each measurement of BGS distribution along the FUT, 200 times averaging is adopted to make the data acquisition speed fast enough to sense the temperature change and maintain good signal quality for such a long FUT. The acquisition time of each measurement along FUT costs 3mins, within which the temperature changes by 0.42^{o}C, corresponding to a BFS change of 0.43MHz (BFS-temperature coefficient of 1.034MHz/^{o}C). Since 0.43MHz is even less than one-half of the frequency-sweeping interval of 1MHz, the temperature can be regarded as constant within the data acquisition process of each measurement. The measurement starts almost at the same time when the temperature change process begins, and hence the total measurement time is approximately equal to that of the temperature change process, i.e., 225mins, during which 76 consecutive measurements of BGS distribution along FUT have been finished. After data collection, they are combined to form a video, which is then denoised by VBM3D with a specific frame number. For example, supposing the frame number is 10, the block search range will be adjacent ten measurements, and the denoising process will be finished using this block range for all 76 measurements, as depicted in Fig. 6.1. Figure 6.8 shows the temperature as a function of time obtained from a thermometer inside the oven (black curve, denoted as actual temperature), raw data (red curve) and corresponding data after VBM3D denoising with different frame numbers (1, 2, 5, 10, 15 and 20). Note that for the raw data and those after denoising by VBM3D, the measured temperature is the average temperature along the last 196m FUT in the oven. From Fig. 6.8, we can see that the temperature obtained from the raw data has large fluctuations without denoising, and the values deviate from those measured by the thermometer (i.e., actual temperature). While with the denoising by VBM3D, both the temperature fluctuations and deviations decrease when the frame number increases from 1 (pink curve) to 15 (blue curve), which clearly indicates that VBM3D can effectively make use of the temporal correlation between each frame to denoise the data under slowly varying temperature environment. However, when the frame number increases to 20, we find that the temperature after denoising starts to deviate from the actual temperature, which may originate from the loss of some valuable details of the data due to excessive denoising when using a large frame number. The impact of the frame number on the measurement accuracy under a slowly varying environment is analyzed quantitatively by calculating the root-mean-square error (RMSE) and uncertainty of the measured temperature values in Fig. 6.8. The RMSE is calculated by comparing temperatures obtained from 76 measurements (i.e., 76 measured temperature values) with those from the thermometer, which represents how close the measured values are to the actual temperature reading from the thermometer. The expression of RMSE is given in Eq. (6.1), where T^{measured} is the temperature values in Fig. 6.8 obtained from raw data or those after denoising by VBM3D, and T^{ture} is the values read from the thermometer.

$$RMSE = \sqrt{\frac{\sum_{k=1}^{76}(T_k^{measured}-T_k^{true})^2}{N}} \tag{6.1}$$

While the uncertainty is calculated using the standard deviation (SD) of the temperature values obtained at the FUT end for a randomly selected actual temperature, e.g., 53.0^{o}C at the time of 111mins (i.e., the 38th data frame in our case). The RMSE represents the deviations of the measured temperature values from the real ones, while the SD depicts the fluctuations of the measured temperature values. The results of RMSE and SD are given in Fig. 6.9. Note that a frame number equal to zero means the result is obtained from the raw data. From Fig. 6.9(a), we can see that the RMSE decreases from 12.86^{o}C to 3.35^{o}C as the frame number increases from 0 to 15. Then it starts to increase when the frame number becomes larger than 15, which agrees well with those in Fig. 6.8. Since the image/video denoising is achieved at the expense of sacrificing some details in the data [36], more details of the measured data will be lost due to excessive denoising when using larger frame number, resulting in the deviation of the measured temperature from the actual temperature and hence the increase of RMSE under larger frame number. On the other hand, the uncertainty has been significantly improved from 21.26^{o}C of raw data to a minimum value of 2.90^{o}C when the frame number is 15, as shown in Fig. 6.9(b). Similar results of the temperature uncertainty can be obtained for other cases. Taking the case of (58.8^{o}C, 150mins) for example, the temperature uncertainty obtained with frame numbers of 0, 1, 2, 5, 10, 15, and 20 are 18.48, 8.03, 5.72, 5.41, 3.86, 3.39, and 3.75^{o}C, respectively. We also obtain the minimum value with the frame number of 15.

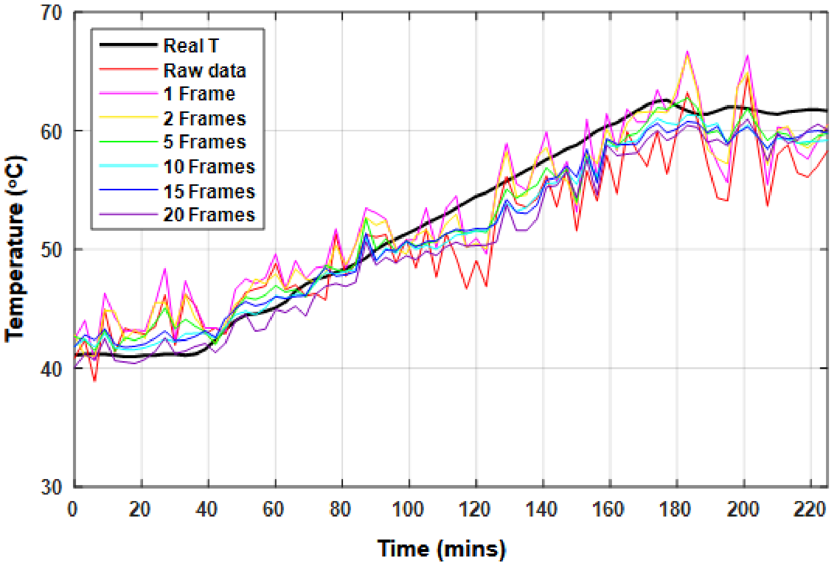

Fig. 6.8: Temperature as a function of time obtained from a thermometer inside the oven, raw data and data after denoising by VBM3D with different frame numbers (1, 2, 5, 10, 15 and 20) . Real T denotes the temperature obtained from the thermometer.

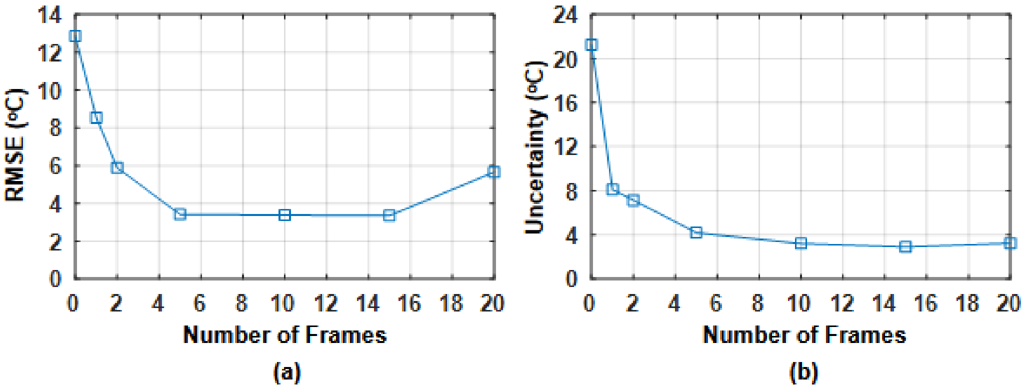

Fig. 6.9: (a) RMSE and (b) uncertainty of the measured temperatures in Fig. 6.8 as a function of the frame number.

We also compare the performance of VBM3D and linear averaging under a slowly varying temperature environment. Here a frame number of 15 is used for the denoising by VBM3D, while linear averaging of 15 adjacent measurements is adopted for a fair comparison. The results are plotted in Fig. 6.10, where the actual temperature (black curve), the measured temperatures by the raw data (red curve) and by the data denoised using VBM3D with a frame number of 15 (blue curve) are the same as those in Fig. 6.8. The green curve gives the temperature as a function of time obtained from the linear averaging. It can be seen that the temperature from the raw data has large fluctuations due to poor SNR at the end of 100.8km FUT. The linear averaging reduces the fluctuations, but it makes the deviation of the measured temperature from the actual temperature even larger, as depicted by the green curve in Fig. 6.10. It is because the linear averaging damages the temporal correlation among the data of adjacent measurements and hence cannot take the slowly varying temperature changing into account. On the other hand, the measured temperature after VBM3D denoising provides small fluctuations and little deviation from the actual temperature. As calculated above, the RMSE of the measured temperature using VBM3D with a frame number of 15 is 3.35^{o}C, compared with the RMSE of 12.86^{o}C for raw data and 15.17^{o}C for the data after linear averaging. This significant improvement of measurement accuracy under slowly varying environments proves the advantage of VBM3D, which exploits both temporal and spatial correlation for denoising with only little sacrifice of data details even when the environment temperature is slowly changing.

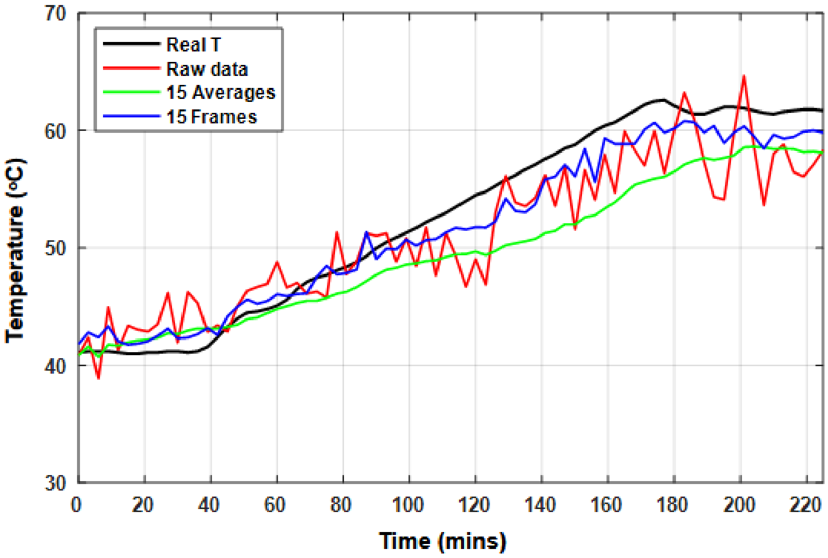

Fig. 6.10: Comparison of the real temperature by the thermometer (black curve), the measured temperatures by the raw data (red curve), by the data after averaging 15 adjacent measurements (green curve), and by the data denoised using VBM3D with a frame number of 15 (blue curve).

6.4 Summary

We have proposed and experimentally demonstrated using VBM3D for denoising in a BOTDA system with 100km long-distance with 2m spatial resolution under static and slowly varying temperature environments. The consecutive measurements of 2D BGS distribution along the FUT form the video sequence. Then it is denoised by VBM3D in both time and space domains. Under a static temperature environment, we achieve the temperature uncertainty of 0.43°C (0.44MHz BFS uncertainty) at the far end of FUT. To our knowledge, this is one of the best BFS uncertainty reported for a sensing distance beyond 100km. On the other hand, we have also successfully measured the slowly varying temperature with a temperature RMSE/uncertainty of 3.35°C/2.90°C. The processing of 1501 (number of sensing points along the last 300m FUT) ×200 (number of scanned frequencies) and ×20 (number of consecutive measurements) data points on our PC with Intel i7-6700k CPU and 16G memory takes 111s. If GPU instead of CPU is used to implement the algorithm, we can reduce the time to 15s [29], and the VBM3D method would be helpful in quasi-real-time monitoring scenarios. The reliable denoising performance of the proposed VBM3D method makes it a practical way of improving the measurement accuracy and sensing distance, especially when there is temporal evolution of the measurand under a slowly varying environment.

References

[1] X. Bao, and L. Chen, “Recent progress in distributed fiber optic sensors,” Sensors, **12**(7). 8601-8639 (2012).

[2] A. Dominguez-Lopez, X. Angulo-Vinuesa, A. Lopez-Gil, S. Martin-Lopez, and M. Gonzalez-Herraez, “Non-local effects in dual-probe-sideband Brillouin optical time domain analysis,” Opt. Express, 23(8), 10341-10352 (2015).

[3] L. Thévenaz, S. F. Mafang, and J. Lin, “Effect of pulse depletion in a Brillouin optical time-domain analysis system,” Opt. Express, 21(12), 14017-14035 (2013).

[4] M. A. Soto, S. Le Floch, and L. Thévenaz, “Bipolar optical pulse coding for performance enhancement in BOTDA sensors,” Opt. Express, 21(14), 16390-16397 (2013).

[5] M. A. Soto, G. Bolognini, and F. Di Pasquale, “Long-range simplex-coded BOTDA sensor over 120km distance employing optical preamplification,” Optics letters, 36(2), 232-234 (2011).

[6] S. Le Floch, F. Sauser, M. Llera, and E. Rochat, “Novel Brillouin optical time-domain analyzer for extreme sensing range using high-power flat frequency-coded pump pulses,” Journal of Lightwave Technology, 33(12), 2623-2627 (2015).

[7] M. A. Soto, X. Angulo-Vinuesa, S. Martin-Lopez, S. H. Chin, J. D. Ania-Castanon, P. Corredera, E. Rochat, M. Gonzalez-Herraez, and L. Thevenaz, “Extending the real remoteness of long-range Brillouin optical time-domain fiber analyzers,” Journal of Lightwave Technology, 32(1), 152-162 (2014).

[8] X. Jia, Y. Rao, Z. Wang, W. Zhang, C. Yuan, X. Yan, J. Li, H. Wu, Y. Zhu, and F. Peng, "Distributed Raman amplification using ultra-long fiber laser with a ring cavity: characteristics and sensing application," Opt. Express, 21(18), 21208-21217 (2013).

[9] H. Iribas, A. Loayssa, F. Sauser, M. Llera, and S. L. Floch, "Cyclic coding for Brillouin optical time-domain analyzers using probe dithering," Opt. Express, 25(8), 8787-8800 (2017).

[10] Z. Yang, M. A. Soto, and L. Thévenaz, "Increasing robustness of bipolar pulse coding in Brillouin distributed fiber sensors," Opt. Express, 24(1), 586-597 (2016).

[11] Y. Dong, L. Chen, and X. Bao, “Time-division multiplexing-based BOTDA over 100km sensing length,” Optics Letters, 36(2), 277-279 (2011).

[12] Y. Dong, L. Chen, and X. Bao, “Extending the sensing range of Brillouin optical time-domain analysis combining frequency-division multiplexing and in-line EDFAs,” Journal of Lightwave Technology, 30(8), 1161-1167 (2012).

[13] Y. Fu, Z. Wang, R. Zhu, N. Xue, J. Jiang, C. Lu, B. Zhang, L. Yang, D. Atubga, and Y. Rao, “Ultra-long-distance hybrid BOTDA/φ-OTDR,” Sensors, 18(4), 976 (2018).

[14] X. H. Jia, J. Y. Rao, C. X. Yuan, J. Li, X. D. Yan, Z. N. Wang, W. L. Zhang, H. WU, Y. Y. Zhu, and F. Peng, “Hybrid distributed Raman amplification combining random fiber laser based 2nd-order and low-noise LD based 1st-order pumping,” Optics express, 21(21), 24611-24619 (2013).

[15] X. Angulo-Vinuesa, S. Martin-Lopez S, J. Nuño, P. Corredera, J. D. Ania-Castanon, L. Thevenaz, and M. Gonzalez-Herraez, “Raman-assisted Brillouin distributed temperature sensor over 100 km featuring 2 m resolution and 1.2 oC uncertainty,” Journal of Lightwave Technology, 30(8), 1060-1065 (2012).

[16] S. Martin-Lopez, M. Alcon-Camas, F. Rodriguez, P. Corredera, J. D. Ania-Castanon, L. Thevenaz, and M. Gonzalez-Herraez. “Brillouin optical time-domain analysis assisted by second-order Raman amplification,” Opt. Express, 18(18), 18769-18778 (2010).

[17] Marcelo A. Soto, Gabriele Bolognini, and Fabrizio Di Pasquale, "Optimization of long-range BOTDA sensors with high resolution using first-order bi-directional Raman amplification," Opt. Express, 19(5), 4444-4457 (2011).

[18] Fu, Yun, R. Zhu, B. Han, H. Wu, Y. Rao, C. Lu, and Z. Wang, "175km repeaterless BOTDA with hybrid high-order random fiber laser amplification." Journal of Lightwave Technology, DOI: 10.1109/JLT.2019.2916413 (2019).

[19] X. Hong, W. Lin, Z. Yang, S. Wang, and J. Wu, "Brillouin optical time-domain analyzer based on orthogonally-polarized four-tone probe wave," Opt. Express, 24(18), 21046-21058 (2016).

[20] A. Dominguez-Lopez, Z. Yang, M. A. Soto, X. Angulo-Vinuesa, S. Martin-Lopez, L. Thevenaz, and M. Gonzalez-Herraez, "Novel scanning method for distortion-free BOTDA measurements," Opt. Express, 24(10), 10188-10204 (2016).

[21] J. J. Mompó, J. Urricelqui, and A. Loayssa, "Brillouin optical time-domain analysis sensor with pump pulse amplification," Opt. Express, 24(12), 12672-12681 (2016).

[22] B. Wang, B. Fan, D. Zhou, C. Pang, Y. Li, D. Ba, and Y. Dong, "High-performance optical chirp chain BOTDA by using a pattern recognition algorithm and the differential pulse-width pair technique," Photonics Research, 7(6), 652-658 (2019).

[23] M. A. Soto, J. A. Ramírez, and L. Thévenaz, “Intensifying the response of distributed optical fibre sensors using 2D and 3D image restoration,” Nature Communications, 7, 10870 (2016).

[24] M. A. Soto, J. A. Ramírez, and L. Thévenaz, “Optimizing Image Denoising for Long-Range Brillouin Distributed Fiber Sensing,” Journal of Lightwave Technology, 36(4), 1168-1177 (2017).

[25] H. Wu, L. Wang, Z. Zhao, N. Guo, C. Shu, and C. Lu, "Brillouin optical time domain analyzer sensors assisted by advanced image denoising techniques," Opt. Express, 26(5), 5126-5139 (2018).

[26] K. Dabov, A. Foi, and K. Egiazarian, “Video denoising by sparse 3D transform-domain collaborative filtering,” in Proc. European Signal Processing Conference (EUSIPCO) (IEEE, 2007), Poznan, 145-149 (2017).

[27] K. Dabov, A. Foi, V. Katkovnik, and K. Egiazarian, “Image denoising by sparse 3-D transform-domain collaborative filtering,” IEEE Transactions on Image Processing, 16 (8), 2080-2095 (2007).

[28] Y. Dong, H. Zhang, L. Chen, and X. Bao, “2 cm spatial-resolution and 2 km range Brillouin optical fiber sensor using a transient differential pulse pair,” Applied Optics, 51(9), 1229-1235 (2012).

[29] S. Sarjanoja, J. Boutellier, and J. Hannuksela, “BM3D image denoising using heterogeneous computing platforms,” in Conf. on Design and Architectures for Signal and Image Processing (DASIP 2015), pp. 4159–4167 (2015).

7 Towards Detecting Red Palm Weevil Using Machine Learning and Fiber Optic Distributed Acoustic Sensing

RPW is a detrimental pest that has wiped out many palm tree farms worldwide. Early detection of RPW is challenging, especially in large-scale farms. Here, we introduce the combination of machine learning and fiber optic DAS techniques as a solution for the early detection of RPW in vast farms. Within the laboratory environment, we reconstructed the conditions of a farm that includes an infested tree with about 12-day-old weevil larvae and another healthy tree. Meanwhile, some noise sources are introduced, including wind and bird sounds around the trees. After training with the experimental time- and frequency-domain data provided by the fiber optic DAS system, a fully-connected ANN and a convolutional neural network (CNN) can efficiently recognize the healthy and infested trees with high classification accuracy values (99.9% by ANN with temporal data and 99.7% by CNN with spectral data, in reasonable noise conditions). This work paves the way for deploying the high-efficiency and cost-effective fiber optic DAS to monitor RPW in open-air and large-scale farms containing thousands of trees.

7.1 Motivation

The date palm is a high-value fruit crop that provides healthy nutrition security to millions worldwide [1]. It is further regarded as an essential source of export revenue for rural smallholders worldwide. Unfortunately, the date production and trade are in danger because of the RPW, also named Rhynchophorus ferrugineus [2,3]. RPW is a Coleopteran snout pest, considered the single most destructive pest of palm trees. Young and soft trees aged less than 20 years, representing about 50% of the total cultivated date palm trees, are vulnerable since RPW typically targets them [4]. Besides date palms, RPW attacks coconut, oil, and ornamental palms [4,5]. RPW has been found in more than 60 countries in the past few decades, including the Mediterranean region, Central America, the Middle East, and North Africa [4,6]. This plague has globally destroyed many palm farms causing severe economic losses in the form of lost production or pest-control costs. As representative examples, Figure 7.1 shows the RPW's impact on two date palm trees, after treating the trees with scraping to remove the RPW entirely.

Fig 7.1: Two representative examples of treated trees by scraping to remove red palm weevil (RPW).

In the early stage of infestation, chemical treatments can heal palm trees [7]. However, a palm tree only shows visual distress signs in a well-advanced stage of infestation, where it is difficult to save the tree. Many techniques have been reported in the literature for the early detection of RPW [8-10]. Some detection methods, such as x-ray-based tomography [9] and trained dogs [10], are accurate; however, they lack feasibility in large-scale farms because of their slow scanning processes. The most promising early detection methods base on sensing the larvae's sound while chewing the core of a palm trunk. The larvae start to produce eating sounds in an early infestation stage, where the larvae are less than two weeks old [11]. Existing acoustic detection technologies rely on inserting acoustic probes within the individual tree trunks and building a wireless network to communicate with the sensors [8]. Unfortunately, assigning a sensor per tree is cost-ineffective, especially for vast farms containing thousands of trees. Additionally, this method is invasive and may harm the trees or create nests for insects.

We recently reported a solution of using a fiber optic DAS for the early detection of RPW, such that a single optical fiber is noninvasively wound around the palm trees to possibly scan a large-scale farm within a short time [11,12]. As reported in [11], distinguishing the healthy and infested trees was achieved through a straightforward signal processing algorithm since the experiment was conducted in a controlled environment. Identifying infested trees in open-air farms, where the optical fiber might be subjected to harsh environmental noises, would require a more advanced signal processing technique to classify the larvae sound and other noise sources.

To pave the way for utilizing the fiber optic DAS to monitor real farms, here, we introduce neural network-based machine learning algorithms to classify healthy and infested trees, based on the data collected by a fiber optic DAS. Within a laboratory environment, we mimic a farm's environmental conditions, including the healthy/infested palm tree and other noise sources. In particular, the sound of about 12-day-old weevil larvae is played inside a tree trunk. And meanwhile, the tree is subjected to external wind and bird sounds as noise sources. We use a fully-connected ANN [13] and a CNN [14] to recognize the infested and healthy trees in the noisy environment. We further investigate the impact of different optical fiber jackets on mitigating the external noise around the trees. This work would be highly beneficial for the future deployment of the fiber optic DAS for the early detection of RPW in vast real farms.

7.2 Experimental design

Figure 7.2(a) shows the entire scheme of our experiment. We integrate the optical and electronic components of the DAS system inside a sensing unit. We inject the output light from the sensing unit into an SMF and wind a section of the fiber around a tree trunk. Inside the trunk, we implant a loudspeaker (SRS-XB21, Sony, 20Hz-20000Hz frequency transmission range), continuously playing an eating sound of about 12-day-old weevil larvae. At around 1m distance from the tree, a fan blows air, with a speed of about 3m/s, toward the optical fiber and tree. Also, at around 1m distance from the tree, we locate another loudspeaker (AudioCube, Allococac, 40Hz-20000Hz frequency transmission range) continuously producing bird sounds. At the outer surface of the tree, we place a sound level meter that can record the various sound intensity levels used in the experiment. The measured sound intensity level of the background noise within the laboratory is around 51dB, caused by the instruments working in the laboratory, which rises to about 71dB when only playing the bird sounds. The intensity level of the bird sounds is roughly equal to that we hear on farms. According to the literature [8] and our experience, humans can hear the larvae sound under acceptable environmental noise. As measured by the meter, when only the loudspeaker within the tree turns on, we set the intensity levels of the larvae sound to be within the range [51dB to 75dB]. The low-level cannot be distinguished from the background noise by the meter, while the other high-threshold is obvious. The selected larvae sound intensity levels within this range should represent all possible degrees of infestation (weak, medium, and strong

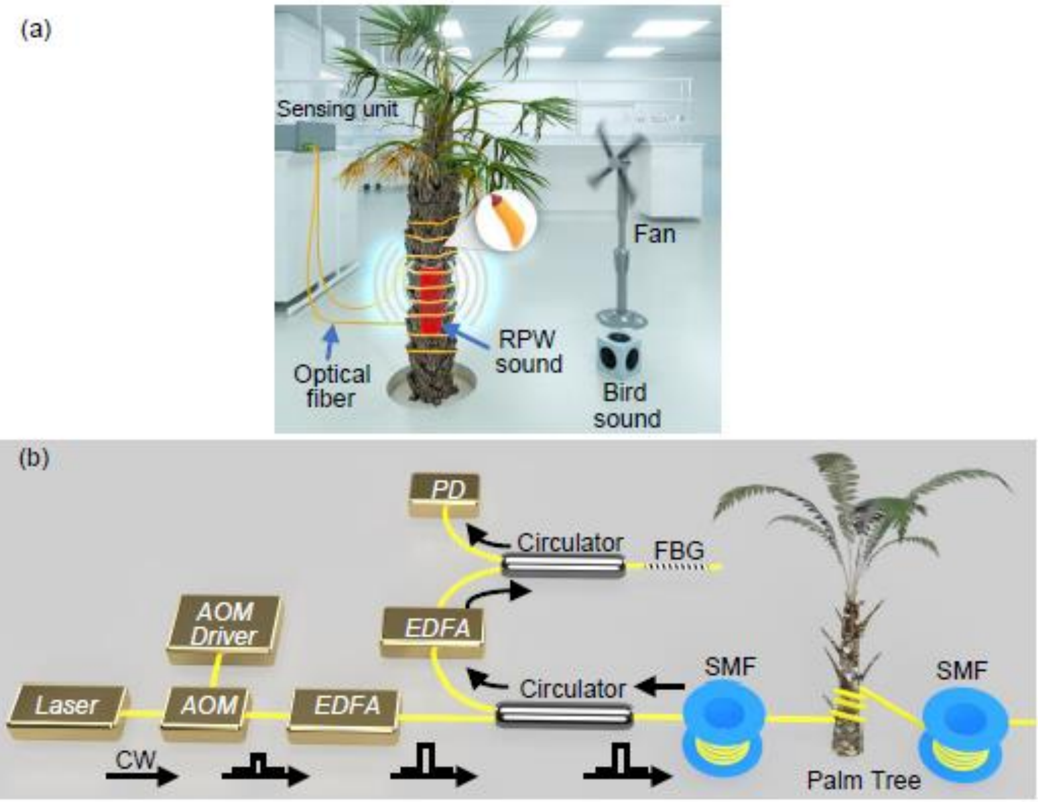

Fig 7.2: (a) Overall scheme of using the DAS system to detect the RPW sound. (b) Experimental setup of the DAS interrogation unit.

infestation).

The sensing unit contains the interrogation part of the DAS except for the sensing fiber (Fig. 7.2(b)), which has the same principle as the phase-sensitive optical time-domain reflectometry (Φ-OTDR) [15]. A very narrow linewidth laser generates a CW light of a 100Hz linewidth and a 40mW optical power. Then, an acousto-optic modulator (AOM) converts the light into optical pulses with a 50ns pulse width and a 5kHz repetition rate, corresponding to a 5m spatial resolution. The power of the optical pulses is amplified using an EDFA, while its output light is injected through a circulator into a standard SMF of about 2km long. At around 1km distance from the beginning position of the SMF, we wind a 5m fiber section around the tree trunk. The backscattered signal from the SMF is amplified with another EDFA. And then an FBG removes its ASE noise. The filtered Rayleigh signal is detected by a PD and sampled by a digitizer of a 200MHz sampling rate. Finally, we record the Rayleigh signals as 1s periods (5000 traces per period). This experiment includes the utilization of two different standard SMFs, protected with different jackets of a 900μm diameter (Thorlabs, SMF-28-J9, denoted as "JKT1") and a 5mm diameter (YOFC, YOFC-SCTX3Y-2B1-5.0-BL, denoted as "JKT2"), respectively.

Figure 7.3 shows an example of a Rayleigh trace read by the DAS system. The high-power signal located at the start of the SMF is typical and corresponds to the Fresnel reflection from the front facet of the SMF. In the ideal scenario, when there is no refractive index perturbation along the SMF, the shape of the Rayleigh trace remains stationary in the time-domain for all the spatial points along the entire fiber [15,16].

Consequently, the differences between the temporal subsequent Rayleigh traces and an initial reference one would be ideally zeros. In contrast, a larvae sound within the tree trunk can modulate the fiber's refractive index at the tree position, which changes the corresponding temporal Rayleigh signal only at the tree location. The location of an infested tree and the larvae sound frequencies can be identified by applying the normalized differential method [17] and fast Fourier transform (FFT) to the temporal Rayleigh traces.

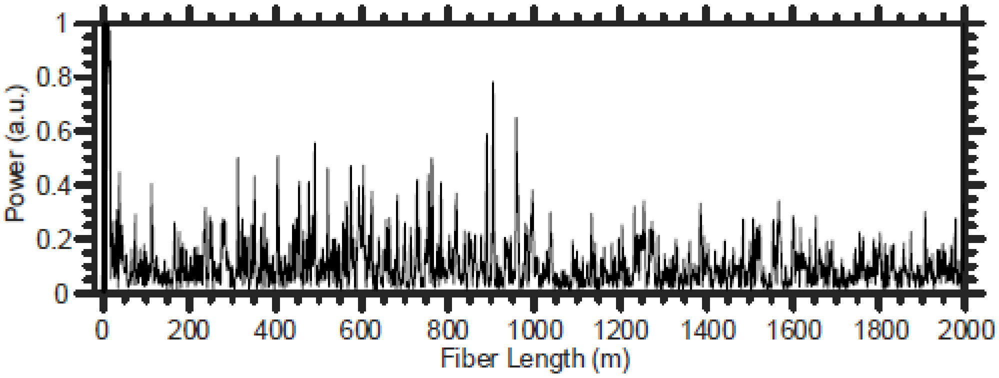

Fig 7.3: A representative example of a Rayleigh trace recorded by the fiber optic DAS.

7.3 Investigating the impact of the noise sources on the DAS system

In this section, we explore the possible ways of mitigating environmental noises, such as wind and bird sounds, which may degrade the performance of the fiber optic DAS system when detecting the RPW. The suggested techniques for reducing the noise include applying a spectral band-pass filter to alleviate the noise level within the recorded signals and further trying various optical fiber jackets that the wind might shake. This investigation is necessary to improve the performance of the machine learning algorithms while classifying the healthy and infested trees and also to make the DAS system more feasible for accurate RPW detection.

Firstly, we explore the spectral components of the actual larvae sound. In particular, a commercial voice recorder (ICD-UX570, Sony, 50Hz-20000Hz frequency response) is implanted inside an indeed infested tree trunk and next to about 12-day-old larvae, shown in Fig 7.4(a), such that the voice recorder stores the larva's sound using the uncompressed linear pulse-code modulation (LPCM) format to have a pristine quality audio file all the time [18]. We select this specific RPW life stage to examine if our sensor can detect the larvae's sound at an early stage. Thus, the palm tree can still be saved and cured. During the recording time, the larvae eat and move naturally within the trunk without restriction. Consequently, the quality of the simulated sound in the laboratory should be comparable to the real one. The age of the larvae can be well controlled via an artificial infestation process [11], which is carried out in a secured research facility to avoid spreading the RPW to other healthy trees. Interestingly, we observe that the larvae almost continuously produce the sound while they are chewing the tree trunk. Figure 7.4(b) shows two different representative examples of the larvae sound's power spectra, each corresponding to a 0.5s recording interval. The results of Fig. 7.4(b) indicate that most larvae sound's optical power is around 400Hz.

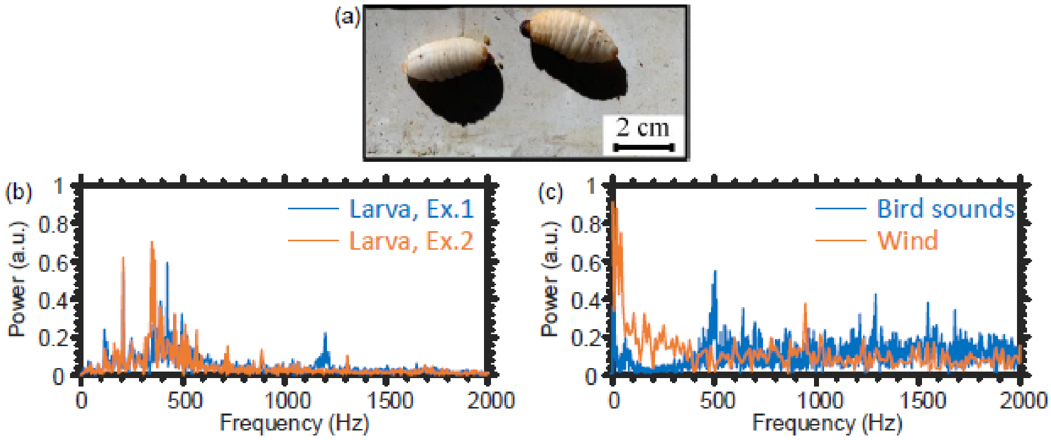

Fig 7.4: (a) ~12 days old weevil larvae. (b) Two representative examples of the larvae sound's spectra, marked as Ex. 1 and Ex. 2, produced using the data of the voice recorder. (c) Examples of the power spectra produced by bird sounds and wind.

In contrast, the used bird sounds have a broad spectrum (Fig 7.4(c), blue line), which interferes with that of the larvae. Regarding the wind as a noise source, the orange line in Fig 7.4(c) represents an example of the vibration's power spectrum caused by wind when shaking the "JKT2" fiber. The tree swinging dominates the vibration caused by wind, which has low-frequency components. However, wind may also directly shake the optical fiber to produce other vibrations of high frequencies, which may overlap with the larvae sound. Because the vibration strength caused by the wind is larger than that of the larvae sound, the wind's high-frequency vibration must be considered a noise source. Given the results of Figs 7.4(b), 7.4 (c), for the entire following temporal vibration data that we collect using the fiber optic DAS, we will apply a [200Hz-800Hz] band-pass filter to enhance the SNR of our system. It is because the spectral filter can remove the low vibration frequency components, less than 200Hz, to avoid the inevitable mechanical vibration in the laboratory and the tree swinging caused by wind. Meanwhile, it filters out the high-frequency (larger than 800Hz) components, produced by the electronic/optical components in the system, without impacting the larvae sound's dominant frequencies (around 400Hz).

Focusing on the experimental design of Fig. 7.2(a), we initially switched off the fan and the outside noise loudspeaker, while we only played the larvae sound using the loudspeaker implanted inside the tree trunk. Figures 7.5(a-d) show two representative examples of the normalized differential time-domain signals recorded using the DAS system [17], followed by applying the [200Hz-800Hz] band-pass filter, when using the SMF of JKT1/JKT2. Obviously, the two fibers accurately locate the position of the infested tree at about 1km distance from the input ports of the fibers. The other noisy signals, which sometimes appear at the start of the SMFs, result from the fiber front

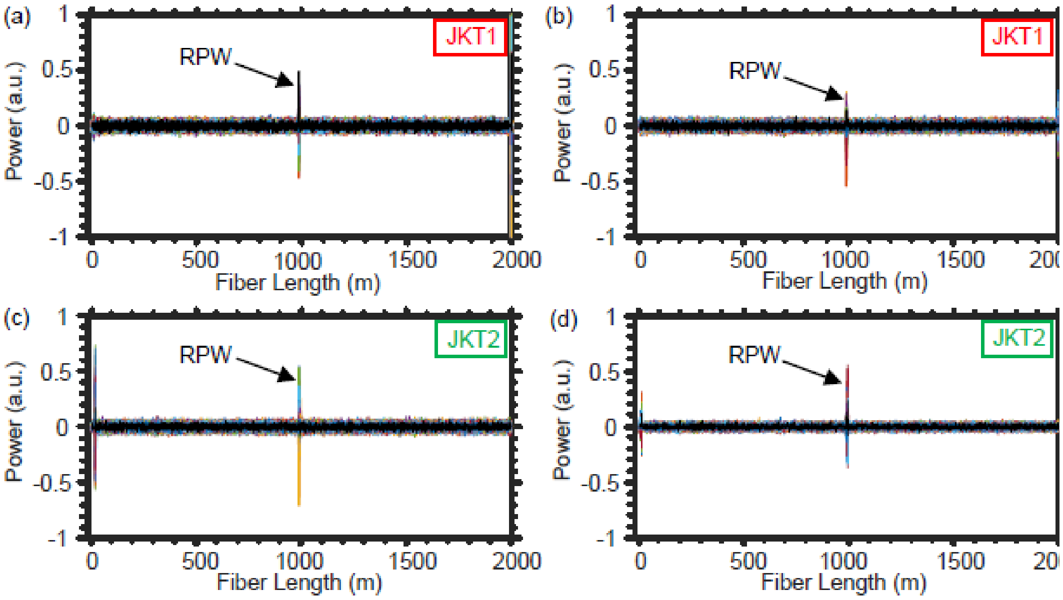

Fig. 7.5: Representative examples of the infested tree’s position information when using the SMF of JKT1 (a), (b) and JKT2 (c), (d).

facet's reflection.

Next, we turn off the two loudspeakers and only turn on the fan to inspect the impact of the wind on the two SMFs. The wind would be regarded as the primary noise source in open-air farms, mainly because our detection technique is noninvasive, and the fiber would typically be affected by vibrations caused by wind. Even with applying the [200Hz-800Hz] band-pass filter, the SMF of JKT1 is affected by the wind to produce temporal vibrations, as shown in Fig. 7.6(a,b). The low-frequency vibrations, produced by tree swinging caused by the wind, can be easily removed while filtering out frequencies below 200Hz [19]. However, signal frequencies, due to fiber shaking from blowing the wind directly to the optical fiber, rely on the thickness and material of the fiber's jacket. As shown in Fig.7.6(a,b), the SMF of JKT1 with a relatively small diameter (900μm) generates vibration signals caused by the wind, which may be similar

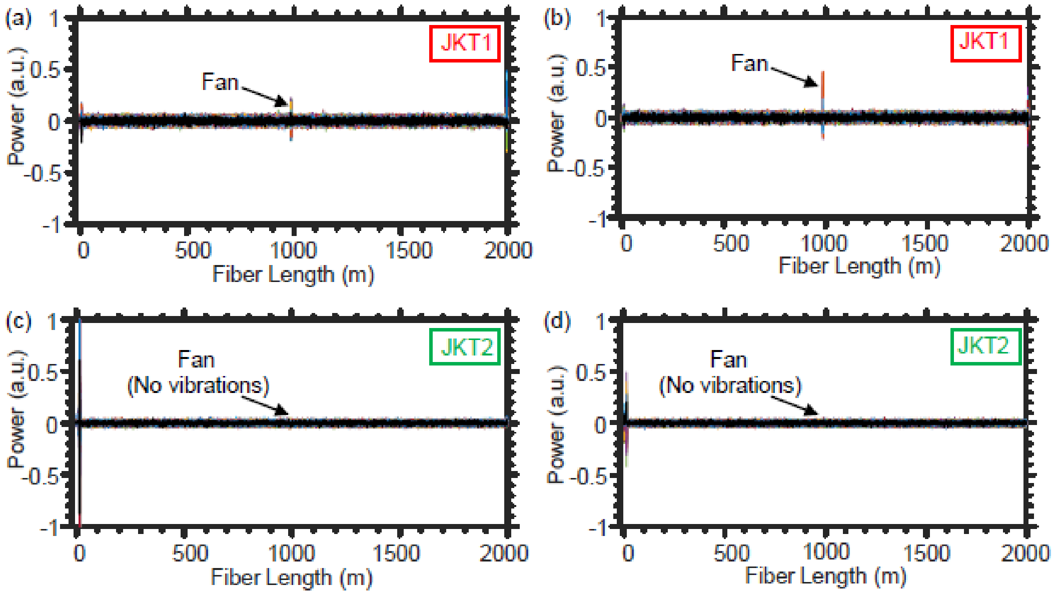

Fig. 7.6: Representative examples of the temporal vibrations caused by the wind when using the SMF of JKT1 (a), (b) and JKT2 (c), (d).

to those of the larvae sound. This phenomenon may confuse machine learning algorithms when recognizing healthy and infested trees.

Similarly, while switching off the two loudspeakers and turning only the fan on, we use the DAS system when winding the SMF of JKT2 around the tree trunk. Since the JKT2 is relatively thick (5mm diameter), the fiber rarely generates shaking frequencies within the [200Hz-800Hz] range because of the wind, shown in Fig 7.6(c,d). Such a comparison between the two fiber jackets in terms of mitigating the noise produced by wind is crucial for determining the proper optical fiber cable we can utilize in real farms in the future. Besides, compared with JKT1, JKT2 has an additional advantage: it is durable enough to sustain the harsh environmental conditions of farms, and the SMF inside JKT2 cannot be easily broken by, for example, stepping on the fiber by farmers.

We further investigate the impact of the noise produced by the bird that may surround the optical fiber in farms. In particular, we switch off the larvae sound's loudspeaker and the fan, while playing only the outside loudspeaker. Fortunately, the two SMFs of JKT1 and JKT2 cannot “hear” the bird sounds, as shown in Fig. 7.7(a,b), respectively. It is because the air between the loudspeaker and the optical fiber jackets significantly attenuates the vibration energy of the bird sounds. Typically, we can use a fiber optic DAS system to detect sound propagating through the air, with a thin metallic sheet attached to the fiber to amplify the attenuated vibration energy by air [20]. However, our experiment does not use a metallic sheet to avoid recording the acoustic noise signals generated around the tree.

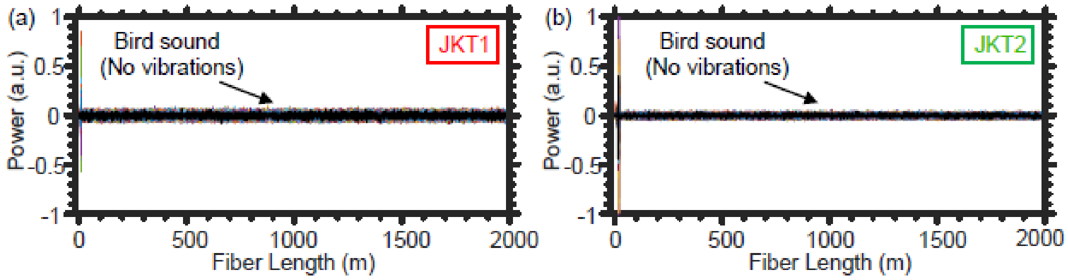

Fig. 7.7: Representative examples of the temporal vibrations caused by the bird sounds when using the SMF of JKT1 (a) and JKT2 (b).

It is also worth discussing the impact of using the JKT1 and JKT2 on the overall noise floor. The noise floor depends on many factors, such as temporal pulse intensity fluctuation, laser phase noise and frequency drift, the low extinction ratio of the launched pulses, photodetector thermal, and shot noise [15,21], which are all common when using the JKT1 or JKT2. However, another major factor contributing to the noise floor is the overall isolation of the optical fiber from externally induced vibrations. Consequently, the thicker jacket, i.e., JKT2, typically provides a lower noise floor.

7.4 Classifying infested and healthy trees using machine learning methods

Machine learning methods trained through supervised learning can effectively identify infested and healthy trees. Machine learning can reveal patterns associated with the larvae sound and simultaneously deal with the large amount of data produced by the DAS system. In this work, we compare the efficiencies of classifying the healthy and infested trees when using the time- and frequency-domain data as separate inputs to neural networks designed using the fully-connected ANN and CNN architectures. Given the advantages mentioned above of the SMF of JKT2, we decided to use it in the subsequent analyses of classifying the healthy and infested trees using machine learning methods.

We initially focus on organizing and labeling the time- and frequency-domain data for the ANN. As mentioned above, we wind a 5m fiber section around the tree, with a 200MHz data sampling rate of the digitizer. Consequently, given the time-of-flight within the OTDR sensing system, the optical fiber section around the tree is represented by 10 spatial points (i.e., the digitizer's sampling resolution is about 0.5m). For each point, the digitizer reading takes a 1s period, i.e., 5000 readings in the time-domain per one reading period because the pulse repetition rate is 5kHz. Since the digital band-pass filter typically distorts a short-interval at the beginning of the time-domain signal, we discard the first 250 time-domain readings for each spatial point. Thus, we organize each trial's temporal data as a vector of 47500 length (concatenating 4750 time-domain readings x10 spatial points). In contrast, by applying the FFT to the time-domain data of each spatial point, we get 2375 frequency components. Subsequently, we organize the spectral data of each trial as a vector of 23750 length (concatenating 2375 frequency components x10 spatial points).

We label the data as “infested” or “healthy” tree, based on the SNR value of the acoustic signal at the tree position. We define the SNR as the ratio between the root-mean-square (RMS) value of the time-domain signal at the tree position and that at another calm reference fiber section of a 5m length. We evaluate the ability of the machine learning algorithms to classify the infested and healthy trees in two cases, without and with the presence of wind. Considering the first case, when ignoring the wind, we play the loudspeaker within the tree trunk and stop the fan to mark the signals of the infested tree. If the SNR>2dB, the minimum acceptable SNR of a DAS system [17], we record and label the signal as “infested”. We collect 2000 examples of the infested signals, when setting the sound of the larvae loudspeaker at various intensity levels within the range [51dB-75dB] mentioned above. In contrast, when we turn off the larvae loudspeaker and fan, we record other 2000 samples for the “healthy” signals. We record the “healthy” signal examples despite the SNR value being higher or lower than the 2 dB threshold.

Focusing on labeling the data when considering the presence of the wind, we simultaneously turn on the larvae loudspeaker and the fan to record the examples of the “infested” signals. Similarly, we recorded 2000 different examples of SNR values exceeding the 2 dB threshold. Next, we switch off the larvae speaker while keeping the fan on to record the other 2000 examples, regardless of the SNR values, for the healthy tree.

The ANN models used to handle the time- and frequency-domain data have a similar architecture, shown in Fig. 7.8. This structure consists of one input layer, two hidden layers, and one output layer. The number of nodes in the input layer matches the number of elements in the data vectors, i.e., 47500 and 23750 for the time- and frequency-domain data, respectively. Besides, the first and second hidden layers comprise 500 and 50 nodes, depending on repeated and sufficient trials towards

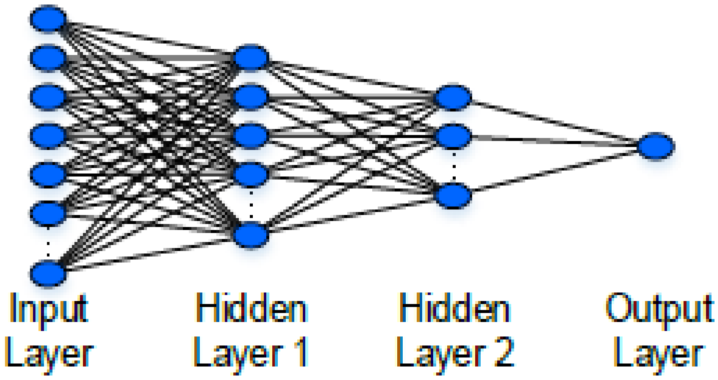

Fig. 7.8: The ANN structure for detecting the RPW infestation using the temporal/spectral data.

maximum classification accuracy. At the end of the fully-connected ANN, there is an output layer of one node for the binary classification (infested or healthy). Regarding the activation functions, we use the rectified linear unit (ReLU) for the hidden layers and the sigmoid function for the output layer.

When the wind is ignored (the fan is turned off), we split the collected temporal/spectral data as 60% (2400 examples) training, 20% (800 examples) validation, and 20% (800 examples) testing datasets. In this case, Figure 7.9(a,c) shows the evolution of the training/validation accuracy and loss with the epoch, when using the temporal [spectral] data. At the end of the training cycles, validation accuracy values of 82.0% and 99.8% are produced for the time- and frequency-domain data, accordingly. When using the temporal data, shown in Fig. 7.9(a), the final validation accuracy is clearly lower than that of the training process, which presents the lack of generalization capability of the model. In contrast, as shown in Fig. 7.9(c) of the spectral data, the validation accuracy perfectly matches the training one, confirming that the ANN model learns the features well instead of just remembering the input data.

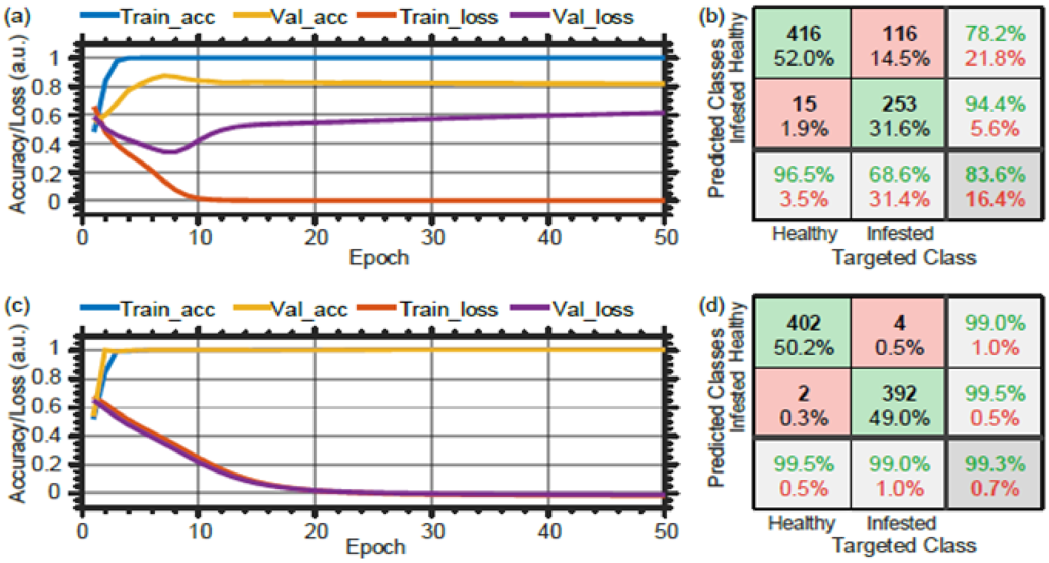

Fig. 7.9: Training and validation history (a)/(c) and confusion matrix (b)/(d) when ignoring the wind and using the temporal/spectral dataset with the ANN. Train_acc: training accuracy; Val_acc: validation accuracy; Train_loss: training loss; Val_loss: validation loss.

Following the training and validation processes, we use the testing datasets to estimate the performance of the two models. Figures 7.9(b,d) show the confusion matrices using the time- and frequency-domain data, respectively. In general, a confusion matrix comprises four leading indices denoted as true negatives (TN), false negatives (FN), false positives (FP), and true positives (TP), which compare the actual target values with those predicted by the machine learning model [22]. Besides, some other essential performance metrics (accuracy, precision, recall, and false alarms) are also included in the confusion matrix and defined as [22]:

$$Accuracy = (TP+TN)/(TP+FP+TN+FN),$$

$$Precision = TP/(TP+FP),$$

$$Recall = TP/(TP+FN),$$

$$False\ Alarm = \quad FP/(TP+FP).$$

As shown in the confusion matrices of Fig. 7.9(b,d), the temporal data provides a total classification accuracy of 83.6%, while that of the spectral data is 99.3%. The entire ANN's performance parameters are summarized in Table 7.1, first and second rows, when neglecting the wind and using the temporal and spectral data. As a result, it is recommended to use the ANN with the spectral data of the larvae sound to get a high distinguishing accuracy between the infested and healthy trees. It is because the larvae chewing sound can be shifted within the 1 s recording frame, making it difficult for the ANN model to learn using a limited dataset. However, the shifted temporal acoustic signals produce similar spectra, which facilitate the classification process using the frequency-domain data. Given this conclusion, we decide to rely on the spectral components with the ANN to analyze the following more complex conditions in consideration of the wind’s impact.

We split again the spectral data, collected when we turn on the fan, as 60% (2400 examples) training, 20% (800 examples) validation, and 20% (800 examples) testing datasets. After the training and validation processes, we use the spectral testing dataset to examine the performance of the trained model. For this case, the third row of Table 7.1 shows a summary of the ANN’s performance results. The ANN model provides a total classification accuracy of 99.6%, slightly higher than that produced in the case of neglecting the wind. The precision, recall, and false alarm rates also show minor improvements. These results indicate that the ANN model can perfectly learn the larvae sound’s spectral pattern in the two scenarios, without and with wind, while the tiny perturbations caused by the wind slightly increases the robustness and generalization ability of the model.

Table 7.1: Summary of the ANN's performance for the various environmental conditions

Data	*Accuracy*	*Precision*	*Recall*	*False Alarm*
Temporal data, without wind	83.6%	94.4%	68.6%	5.6%
Spectral data, without wind	99.3%	99.5%	99.0%	0.5%
Spectral data, with wind	99.6%	99.7%	99.5%	0.3%
Spectral data, combined	99.9%	99.9%	99.9%	0.1%

A more realistic case to consider is combining the two spectral datasets, with and without the wind as a noise source. It is reasonable since the air blows intermittently in real farms. Thus, we merge the two datasets to have 8000 examples totally for the infested and healthy trees. Again, we split the entire data into 60% (4800 examples) training, 20% (1600 examples) validation, and 20% (1600 examples) testing datasets. When using the combined data, the classification accuracy, precision, recall, and false alarm rates are improved (shown in the fourth row of Table 7.1), compared to the two former separate cases. These results indicate that the performance of the ANN model is enhanced given the larger quantity and greater variety of training data. Thus, we can conclude that the ANN model performs well when using the combined spectral data of the more realistic condition in farms; however, the ANN model has relatively poor performance with the temporal input data.

CNN is one distinguished category of the deep neural network [14], which is not sensitive to the position of the features and would be effective in handling the temporal larvae sound shifting in the time-domain. In addition, compared with the fully-connected ANN, CNN has relatively fewer parameters to train, which makes CNN easier and more efficient to train with the same dataset size [14,23]. Since CNN has proven high efficiency in classifying images, we arrange the temporal and spectral data in two-dimensional matrix forms. In particular, we arrange the time- and frequency-domain examples as 10 (spatial points) ×4750 (temporal readings) and 10 (spatial points) ×2375 (spectral components), respectively. As representative examples, Figure 7.10(a-d) show the CNN model's input images of the (a) temporal and "infested", (b) temporal and "healthy", (c) spectral and "infested", and (d) spectral and "healthy" data, respectively.

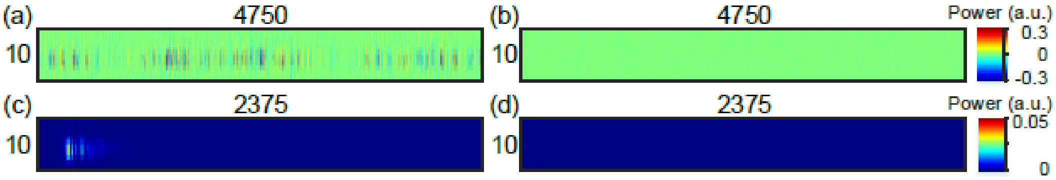

Fig. 7.10: CNN model's input images of the (a) temporal and "infested", (b) temporal and "healthy", (c) spectral and "infested", and (d) spectral and "healthy" data.

Figure 7.11 shows the architecture of the CNN model used to handle the temporal and spectral input data separately. The architecture comprises an input layer, two pairs of convolutional and max pooling layers, a flatten layer, a fully-connected layer, and an output layer. The first (second) convolutional layer has the ReLU activation function and includes 32 (64) filters of a 3×50 (3×5) size and 1×25 (1×5) stride. The two max pooling layers have the same 2×2 pool size and 2×2 stride. After the flatten layer, the fully-connected layer has the ReLU activation function and consists of 50 nodes. Similar to the ANN, the output layer of the CNN also has one node with a sigmoid activation function for binary classification (healthy or infested).

Regarding the data labeling and splitting for the CNN model, we adopt the same techniques and data quantity as those used with the fully-connected ANN. Considering the ideal scenario when the wind is ignored (the fan is turned off), Fig. 7.12(a,c) show the evolution of the training/validation accuracy and loss with the epoch for the temporal and spectral data, respectively. After finishing the training cycles, we obtain the validation accuracy values of 100% and 99.5% accordingly using the time- and frequency-domain data. Besides, the two confusion matrices when using the temporal and spectral testing datasets are shown in Fig. 7.12(b,d), respectively. The results of the confusion matrices show that the performance of the CNN with the temporal data is excellent, with 100.0% accuracy, while that of the spectral data is slightly lower (99.3%). Obviously, compared with the results of Fig. 7.9, the CNN significantly

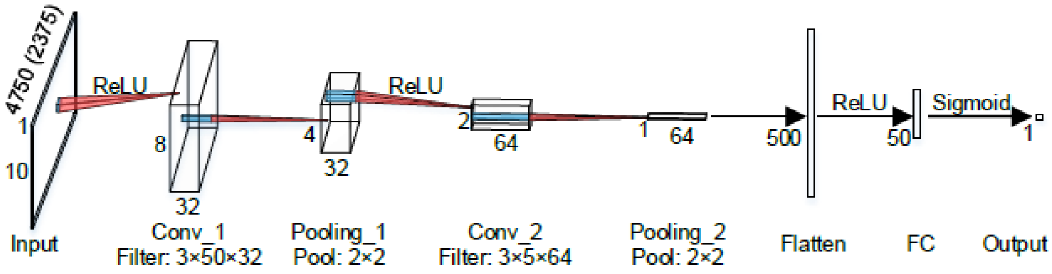

Fig. 7.11: The CNN structure for detecting the RPW infestation using the temporal/spectral data. Conv: convolutional; FC: fully-connected.

improves the classification efficiency in the time-domain. It proves the two main advantages mentioned above of the CNN model over the fully-connected ANN model, i.e., the CNN's spatial invariance and fewer parameters to train. These results are essential since using CNN would offer real-time detection of RPW without applying the intensive FFT to the time-domain data.

Table 7.2 summarizes the CNN's performance when using the temporal and spectral data, in case of ignoring or considering the wind, or mixing the two scenarios.

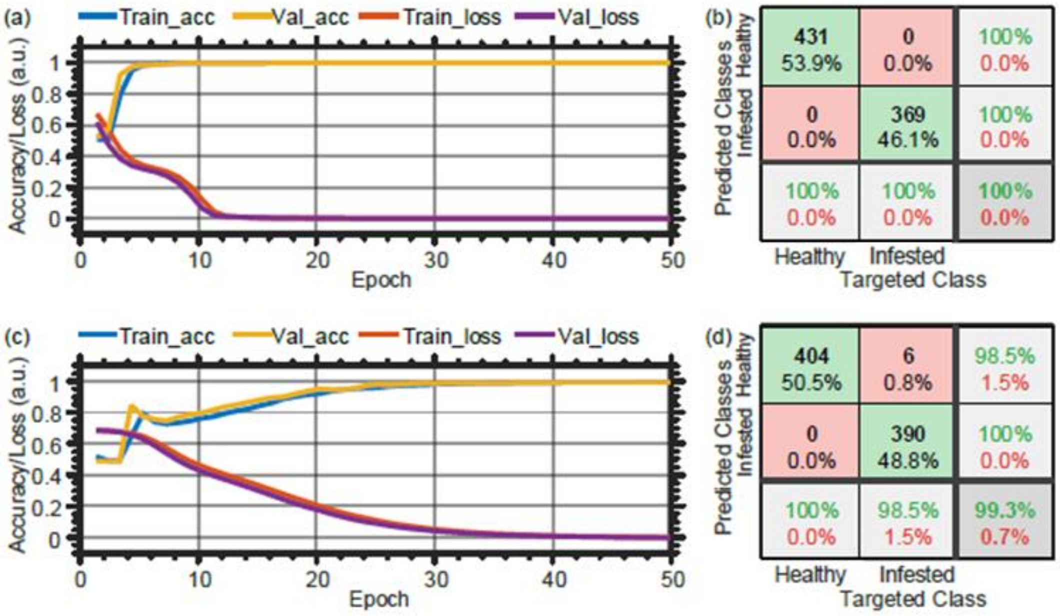

Fig. 7.12: Training and validation history (a)/(c) and confusion matrix (b)/(d) when ignoring the wind and using the temporal/spectral dataset with the CNN. Train_acc: training accuracy; Val_acc: validation accuracy; Train_loss: training loss; Val_loss: validation loss.

As can be observed, the CNN model has a superior performance in the various situations with a minimum classification accuracy of 98.3%. Considering that the time-domain data is easier to process, compared with the spectral data that require additional

FFT steps, we recommend using the CNN and time-domain data for the feasible detection of RPW. Given this conclusion and considering the more convincing case of the combined data, the CNN with the temporal data provides 99.7% accuracy, 99.5% precision, 99.9% recall, and 0.5% false alarm [third row, Table 7.2]. The high precision and low false alarm values confirm the reliability of the CNN model in classifying healthy and infested trees. On the other side, the high recall value represents the great ability and sensitivity of the CNN model to locate the "infested" signals from a mixed "healthy" and "infested" set. In general, the 99.9% and 99.7% can be used to represent the accuracy results of ANN and CNN, respectively. It is because that spectral data and

Table 7.2: Summary of CNN's performance under various environmental conditions

Data	*Accuracy*	*Precision*	*Recall*	*False Alarm*
Temporal data, without wind	100.0%	100.0%	100.0%	0.0%
Temporal data, with wind	99.9%	99.7%	100.0%	0.3%
Temporal data, combined	99.7%	99.5%	99.9%	0.5%
Spectral data, without wind	99.3%	100.0%	98.5%	0.0%
Spectral data, with wind	98.3%	99.5%	97.0%	0.5%
Spectral data, combined	99.1%	99.7%	98.3%	0.3%

temporal data have been found most appropriate for ANN and CNN, respectively. And these accuracies are obtained under the combined conditions (data with wind and data without wind), which best represents the actual environment. A more direct reason why spectral and temporal data are more appropriate for ANN and CNN respectively is that the temporal data includes a lot of noise which may affect the decision of the model, while the CNN has the capability of performing convolutions on the data, which principle is similar as that of Fourier transform and can separate signals and noises.

7.5 Discussion

We have examined the possibility of using machine learning and fiber optic DAS to distinguish healthy and infested trees, in the laboratory environment. However, in actual farm conditions, much more financial and technical issues must be considered during the practical implementation. As reported in the literature [24], the sensing range of the fiber optic DAS can be typically extended to about 10km with a spatial resolution down to 1m. Assuming the separation between two consecutive trees is about 10m and we wind around 1m fiber section around each tree, a DAS sensing unit can simultaneously monitor about 1000 trees. Our entire DAS system costs about 37000USD, including the sensing unit and the optical fiber cable. Thus, the monitoring cost per tree is about 37USD. A recommended deployment plan comprises permanent installation of the optical fiber cables in farms, because fiber optics are relatively cheap and easy to be plugged in/out of the DAS unit, while sharing a portable DAS sensing unit between the farms. Such a plan can significantly reduce the monitoring cost per tree, as the 5m fiber section, wound around a tree in our experiment, costs only about 2 USD. Alternatively, if the farms are close to each other, TDM [25] could be adopted by connecting the farms' optical fibers with a single sensing unit via an optical switch, to scan the individual farms in different time frames.

Besides, in a real palm tree farm, the optical fiber cable might be broken because of the farming activities around the trees. Fortunately, the SMF (YOFC, YOFC-SCTX3Y-2B1-5.0-BL) is well protected with metallic rods to make the fiber shockproof. Furthermore, the outer jacket layer of the fiber optic cable can sustain temperatures as high as 60°C, which helps the fiber to "survive" in the farms' harsh environments. We recommend burying the optical fiber in the soil between the trees for more protection. In the worst-case scenario, if the fiber is getting broken for any reason, the OTDR system can accurately locate the fault point with the spatial resolution of the system [26]. We can use a portable fusion splicer to quickly fix the optical fiber on-site.

In the case of adopting the spiral winding of the optical fiber around trees in a farm, we will need annual maintenance of the sensing system because the trees' girth grow. Advanced planning for redundant fiber lengths between trees will help readjust the fiber wraps around the trees later as they grow. Alternative to the spiral winding plan, longitudinal zigzag attachment of the fiber to the tree trunk is a backup strategy; however, a heavy-duty and stretchable plastic wrap would be used as an outer layer to provide sufficient contact between the optical fiber and tree trunk. The latter strategy is part of our plans for future work on this topic.

It is also worth discussing the contact conditions between the fiber optic cable and the tree trunk. The spatial resolution of our fiber optic DAS system is 5m, which indicates the system cannot distinguish the spatial separations between vibration events that occur within the 5m distance. In the case of winding a fiber length shorter than 5m around the tree, vibration events occurring close to the tree may not be distinguished from those at the tree, resulting in false alarms. Thus, the minimum fiber length needed in this experiment is 5m. Besides, in our experiment, we wind a 5m fiber optic section around the tree with moderate tightness. We observed that some points along the fiber section are not directly touching the tree trunk, because the trunk is sharp at some positions. However, the DAS system still efficiently detects the larvae sound. In other words, having all the points along the 5m fiber optic section in direct and firm contact with the trunk is not necessary to make the system work. Generally, the more tightly we wind the fiber optic around the tree, the higher the SNR. However, it is not easy to quantify by experiments accurately the relationship between the SNR and the tightness of winding the optical fiber. In addition, winding a fiber section longer than 5m will improve the performance of the DAS system. However, our 5m spatial resolution already provides excellent classification accuracy. Besides, for practical applications in palm tree farms, about 10m loose fiber cable is reserved between each two adjacent trees. In this case, 50ns pulse width (5m spatial resolution) is enough to distinguish the larvae generated sounds between two adjacent trees.ss

This discussion shows that the main advantage of our sensor, compared with those reported in the literature, is that the fiber optic DAS provides distributed detection of

RPW. We can scan an entire farm quickly, saving time and effort compared with the other detection methods [8-10] that inspect the trees individually. However, a drawback of our reported system is that the initial installation of the optical fiber requires time and effort, especially in vast farms. Fortunately, the fiber installation only needs to be carried out once per farm, and then the fiber can remain in the farm permanently.

7.6 Summary

Fully-connected ANN and CNN are used to classify an infested tree with RPW and a healthy tree, using the data provided by a fiber optic DAS. To mimic the farm environment within the laboratory, we play the weevil larvae sound inside a tree trunk, while we use wind and bird sounds as noise sources around the tree. Considering the typical conditions when the wind blows discretely, the ANN performs flawlessly with the frequency-domain data to offer a 99.9% classification accuracy. In contrast, CNN produces 99.7% and 99.1% classification accuracy for the same wind conditions when using temporal and spectral data, respectively. Although the CNN's performance is excellent with both kinds of data, we recommend using the CNN with the temporal data to avoid the intensive FFT calculations required to get the spectral components. The results of this work will help following fiber optic DAS deployment for the RPW early detection in real farms.

References

[1] Al-Shahib, W.; Marshall, R.J. The fruit of the date palm: its possible use as the best food for the future?Int. J. Food Sci. Nutr.2003,54, 247–259.

[2] Al-Dosary, N.M.; Al-Dobai, S.; Faleiro, J.R. Review on the management of red palm weevil Rhynchophorus ferrugineus Olivier indate palm Phoenix dactylifera L.Emir. J. Food Agric.2016,28,34–44.

[3] El-Mergawy, R.; Al-Ajlan, A. Red palm weevil, Rhynchophorus ferrugineus (Olivier): economic importance, biology, biogeogra-phy and integrated pest management.J. Agric. Sci. Technol. A2011,1, 1–23.

[4] Food Chain Crisis. Available online: http://www.fao.org/food-chain-crisis/how-we-work/plant-protection/red-palm-weevil/en/ (accessed on 14 Decmber 2020).

[5] Wahizatul, A.A.; Zazali, C.; Abdul, R.; Nurul'Izzah, A.G. A new invasive coconut pest in Malaysia: The red palm weevil(Curculionidae: Rhynchophorus ferrugineus).Planter2013,89, 97–110.

[6] Ferry, M.; Gomez, S. The red palm weevil in the Mediterranean area.Palms2002,46, 172–178.

[7] Llácer, E.; Miret, J.A.J. Efficacy of phosphine as a fumigant against Rhynchophorus ferrugineus (Coleoptera: Curculionidae) inpalms.Span. J. Agric. Res.2010,3, 775–779.

[8] Rach, M.M.; Gomis, H.M.; Granado, O.L.; Malumbres, M.P.; Campoy, A.M.; Martín, J.J.S. On the design of a bioacoustic sensorfor the early detection of the red palm weevil.Sensors2013,13, 1706–1729.

[9] Haff, R.; Slaughter, D. Real-time X-ray inspection of wheat for infestation by the

granary weevil, Sitophilus granarius (L.).Trans.ASAE2004,47, 531.

[10] Suma, P.; La Pergola, A.; Longo, S.; Soroker, V. The use of sniffing dogs for the detection of Rhynchophorus ferrugineus.Phytoparasitica2014,42, 269–274.

[11] Ashry, I.; Mao, Y.; Al-Fehaid, Y.; Al-Shawaf, A.; Al-Bagshi, M.; Al-Brahim, S.; Ng, T.K.; Ooi, B.S. Early detection of red palmweevil using distributed optical sensor.Sci. Rep.2020,10, 3155.

[12] Ooi, B.S.; Ashry, I.; Mao, Y. Beetle Detection Using Optical Fiber Distributed Acoustic Sensor. US Patent Application No.17/050,116, July 09,2018.

[13] Meireles, M.R.; Almeida, P.E.; Simões, M.G. A comprehensive review for industrial applicability of artificial neural networks.IEEE Trans. Ind. Electron.2003,50, 585–601.

[14] Schmidhuber, J. Deep learning in neural networks: An overview.Neural Networks2015,61, 85–117.

[15] Bao, X.; Zhou, D.P.; Baker, C.; Chen, L. Recent development in the distributed fiber optic acoustic and ultrasonic detection.J.Light. Technol.2016,35, 3256–3267.

[16] Lu, Y.; Zhu, T.; Chen, L.; Bao, X. Distributed vibration sensor based on coherent detection of phase-OTDR.J. Light. Technol.2010,28, 3243–3249.

[17] Ashry, I.; Mao, Y.; Alias, M.S.; Ng, T.K.; Hveding, F.; Arsalan, M.; Ooi, B.S. Normalized differential method for improving thesignal-to-noise ratio of a distributed acoustic sensor.Appl. Opt.2019,58, 4933–4938.

[18] Lipshitz, S.P.; Vanderkooy, J. Pulse-Code Modulation—An Overview.J. Audio Eng. Soc.2004,52, 200–215.

[19] Mao, Y.; Ashry, I.; Ng, T.K.; Ooi, B.S.Towards Early Detection of Red Palm Weevil using Optical Fiber Distributed AcousticSensor. InOptical Fiber Communication Conference;OpticalSocietyofAmerica:2019; San Diego, United States, pp. W2A.15.

[20] Mao, Y.; Ashry, I.; Alias, M.S.; Ng, T.K.; Hveding, F.; Arsalan, M.; Ooi, B.S. Investigating the performance of a few-mode fiber fordistributed acoustic sensing.IEEE Photonics J.2019,11,1–10.

[21] Bao, X.; Chen, L. Recent progress in distributed fiber optic sensors.sensors2012,12, 8601–8639.

[22] Wu, H.; Chen, J.; Liu, X.; Xiao, Y.; Wang, M.; Zheng, Y.; Rao, Y. One-Dimensional CNN-Based Intelligent Recognition of Vibrationsin Pipeline Monitoring With DAS.J. Light. Technol.2019,37, 4359–4366.

[23] O'Shea, K.; Nash, R. An Introduction to Convolutional Neural Networks.arXiv2015, arXiv:1511.08458.

[24] Chen, D.; Liu, Q.; He, Z. High-fidelity distributed fiber-optic acoustic sensor with fading noise suppressed and sub-meter spatial sresolution.Opt. Express2018,26, 16138–16146.

[25] Spirit, D.M.; Ellis, A.D.; Barnsley, P.E. Optical time division multiplexing: Systems and networks.IEEE Commun. Mag.1994,32, 56–62.

[26] Tateda, M.; Horiguchi, T. Advances in optical time domain reflectometry.J.

Light. Technol.1989,7, 1217–1.

8 Conclusion

In this Chapter, the conclusion of this thesis about the application of some machine learning and image processing method in DOFS is given. Moreover, some challenges and future works in this field of DOFS are also discussed.

8.1 Conclusion

In the whole work of this thesis, we have investigated the application of some advanced neural network techniques, including ANN, DNN, CNN, and an image processing method, VBM3D, in some DOFS systems. The BOTDA has been demonstrated with those temperature and strain measurement techniques. In addition, the DAS based on Φ-OTDR has been exhibited for the RPW detection task, which is based on the capability of sensing acoustic signals (i.e., vibration/sounds) of the DAS. The advantages of those advanced signal processing methods have been discussed in detail, mainly including higher measurement accuracy, longer sensing distance, and faster detection speed. However, there are still some points we need to explore and optimize further to utilize these techniques in the field of DOFS practically. The skills for better and faster data preprocessing, model training, and parameter optimization are worth further investigation. In addition, the interpretation work to help us understand the principles of NNs is also very essential. The most significant contribution of this work is to provide some typical cases and the corresponding performance results to researchers in this field as valuable references. These experience are useful not only for those techniques mentioned in this work, but also for similar techniques in the whole field of DOFS.

8.2 Challenges of the application of DOFS

There are some significant obstacles hindering growth in the deployment of distributed fiber–optic sensors. The high–cost of fiber–optic sensors poses a significant challenge to the development of this market. Depending on the applications, operating conditions, and the type of fiber–optic cable used, the cost of a distributed fiber–optic sensing system can be very high and still not affordable by every company that requires real-time monitoring and sensing. In addition, the installation and maintenance of these systems are also costly, making their implementation difficult. However, as distributed fiber–optic sensing adoption becomes more rapid, improvements in manufacturing and volume pricing will result in lower costs. Additionally, lifetime continuous monitoring with fiber–optic sensors can offset the high initial cost.

Other technical challenges include the fiber darkening down-hole, where hydrogen penetrates the metal tube around the fiber and fiber jackets to enter the fiber material causing a significant optical attenuation. However, many efforts have been reported to tackle hydrogen darkening by using hermetic coating, tailoring the glass properties, and selecting proper operation wavelengths. Such optical fiber cables with special coating and properties are now readily available for long–term downhole monitoring.

Another hurdle relates to data size, as distributed fiber-optic sensors can continuously monitor the downhole environment and pipelines, producing massive data. Although continuous monitoring offers many advantages, it also comes with its own challenges in data management, storage, visualization, and security. Cloud–based data management has recently been introduced to the oil and gas industry as an efficient means to store, transmit, and visualize data produced by distributed fiber–optic sensors.

On the other hand, the existing challenges in the industry will make the data–driven analyses even more critical. For example, the increasing difficulty of oil recovery and public concerns about the natural environment and resources will require more efficient oil recovery processes and fewer pipeline leakage events, where data from corresponding sensing systems are necessary. The trend of integrated sensing systems and data–driven analyses will complement each other in the oil and gas industry. While the amount of data obtained and required becomes huge, relying only on experts in this field to provide complete and detailed analyses and make decisions along with the whole process is unrealistic. Thus, advanced artificial intelligence (AI) and machine learning methods should be beneficial. They can help reduce the data size, extract valuable data on events, and even make decisions on behalf of the experts. In addition, taking into consideration the present and future employments of many different sensing and measuring systems in the oil and gas industry, the adoption of a cloud–based platform would be a promising solution to solve the problems of secure and reliable data transport, management, storage, analysis, visualization, and download.

8.3 Future works

Distributed fiber–optic sensing has been used across many application fields. The oil and gas industry is one of the most essential applications. This application area has and will have the largest market share now and for the following time. Among three types of DOFS (DTS, DSS, and DAS), the fiber–optic DAS can detect vibrations and their frequencies downhole and along pipelines. Thus, fiber–optic DAS can be used for VSP, hydraulic fracturing monitoring, downhole flow monitoring, well integrity, and pipeline intrusion detection. Raman–based DTS is another distributed sensing technique that measures temperature along an optical fiber cable. DTS has been deployed in many petroleum applications, including downhole flow and injection monitoring, SAGD, and pipeline leak detection. We will continue to develop a prototype for a hybrid sensing system that simultaneously measures vibration and temperature along an SMF/MMF. Various vibration events can be detected along the well.

We also highlighted that Brillouin–based fiber–optic DTSS can be used to monitor well integrity, and detect pipeline deformation. The growth of the fiber–optic DAS, DTS, and DSS market is mainly hampered by their high–cost, which would be mitigated by the rapid adoption of distributed fiber–optic sensing technologies. Finally, we pointed out that improving the overall performance of the sensing systems,multi–parameter sensing, including AI and machine learning, and offering a cloud–based data management are the future research directions of distributed fiber–optic sensing.

The research community for distributed optical fiber sensing (DOFS) continues to develop new technologies in this field, which should provide further application opportunities in all related industries. One of the main goals of the current research work is to improve the overall performance of distributed fiber–optic sensing. For example, introducing new modulation schemes, novel coding formats, and advanced signal processing methods may help reduce spatial resolution limitations, sensing range, and measuring accuracy of distributed fiber–optic sensors. Another research direction is to explore the capabilities of optic fiber sensors, including the distributed ones, to measure more parameters with high reliability in the harsh environment of the industry. In laboratory environments, optical fiber sensors have demonstrated the ability to measure various physical and chemical parameters, such as temperature, strain, vibration, pressure, curvature, rotation, electric/magnetic field, flow, liquid level, and liquid concentration. However, few of these technologies have been reliably adopted in the markets. Thus, it is highly desirable to market more optical fiber sensors, especially DOFS. The development of practical applications will in turn, drive the development of novel technologies.

Besides, for industrial applications, stability and durability are just as important as the sensitivity of the sensors. Generally, the installation schemes of optical fibers directly affect the performance and ruggedness of the sensing systems. Thus, the installation schemes will continue to be investigated and improved in the various application scenes. Furthermore, the system's reliability under different environments in the industry should also be researched, especially in harsh environments with high temperatures and high pressure. It should be noted that novel design and/or doping methods of speciality optical fibers adopted in sensing systems may help reduce transmission loss, increase scattered light, and also increase the system's tolerance for harsh environments. This would emerge new applications of DOFSs in the various sectors of relevant industries.

Another development trend of DOFS in the industry is to integrate different sensing techniques, including DAS, DTS, and DSS, to provide a distributed multiplexed sensing (DXS) system. Since the present DOFS share some identical optoelectronic components and can be employed through one single optical fiber or several optical fibers inside a single tube, it should be feasible to integrate these different techniques into a DXS system based on the need, which provides multi–parameter measurements. One advantage of the integrated DXS system is that its cost is less than the sum of individual sensing systems, while it can provide more helpful information rather than simply adding up the results of several systems. This is because a comprehensive multidimensional data analysis at the exact location would prsovide more profound information on the hotspot.